

**Exploration of the Origin of Substrate Effects and Elastic Strain Properties during
Thin Film Nanoindentation**

by

Bo Zhou

A dissertation submitted to the Graduate Faculty of
Auburn University
in partial fulfillment of the
requirements for the Degree of
Doctor of Philosophy

Auburn, Alabama
December 18, 2009

Keywords: Nanoindentation, Thin Film, Young's Modulus
Substrate Effect

Copyright 2009 by Bo Zhou

Approved by

Barton C. Prorok, Chair, Associate Professor of Materials Engineering
Ruel A. Overfelt, Professor of Materials Engineering
Dong-Joo Kim, Associate Professor of Materials Engineering
Pradeep Lall, Thomas Walter Professor of Mechanical Engineering
Minseo Park, Associate Professor of Physics

Abstract

In this study, the main goal was to investigate the true origin of an influence of substrate effects during nanoindentation of thin films. The work examined the proper relation between the elastic strain intensities in the film and substrate, and modified the Doerner & Nix function used to first describe this situation. A universal mathematical model/formula was developed to better describe the nanoindentation Modulus–Displacement curve. Furthermore, a physical explanation was suggested for the new function. In this project, 15 specimens (including 14 amorphous thin films and 1 nanocrystalline film deposited on Si substrates) were tested using a MTS nanoindentation XP system. The films were tested with a continuous stiffness measurement (CSM), where flat regions were found in the early stage of the $E-h$ curves that reflected the true film modulus.

The flat region (the region without substrate effects) and critical indentation depth (h_{cr}) was determined for each material. A unique non-linear trend was found between the critical indentation depth/film thickness ratio (h_{cr}/t) and film/substrate modulus ratio (E_f/E_s). It was found parameter α in Doerner & Nix function was not a constant as originally suggested. Instead, it changed with the indentation depth. To improve Doerner & Nix function, two parameters α_1 and α_2 were suggested in the equation instead of one, as the elastic strain growth is not continuous in the film and substrate. Based on the experimental investigation and analytical modeling, the two parameters were determined

as the Poisson's ratios of the film and substrate. The new function was found to be adept at closely matching all experimental data collected, which spanned both soft films on hard substrates and hard films on soft substrates.

Acknowledgments

I would like to thank Dr. Prorok for his support and suggestions during this work. I would like to thank Shakib, Nicole, Kevin, Sang, Joshua, Shankar, and Mike for their help in film synthesis, fabrication and finite element Analysis. I also want to thank Dr. Erdemir and Dr. Eryilmaze from Argonne National Lab for their assistance with DLC films deposition. I want to thank all my committee members for their guidance throughout this research. Finally, I want to thank my family for their love and support all these years.

Table of Contents

Abstract.....	ii
Acknowledgments.....	iv
List of Tables	vii
List of Figures.....	viii
List of Abbreviations	xii
Chapter 1 Introduction.....	1
1.1 Synopsis	1
1.2 Dissertation Structure.....	2
Chapter 2 Literature Review.....	5
2.1 Instrumented Indentation Testing.....	5
2.2 Continuous Stiffness Measurement	16
2.3 Thin Films Substrate Effects.....	20
2.4 Finite Element Analysis of Thin Film Nanoindentation.....	30
2.5 Pile-up and Sink-in Effects	34
2.6 Thin Film Microstructure Effects (Size Effects)	41
2.7 Thin Film Deposition Mechanism	42
2.8 X-ray Diffraction Technique.....	46
Chapter 3 Experimental Setup	48
3.1 Thin Film Selection and Deposition	48

3.2 Thin Film Characterizations	55
3.3 Nanoindentation Setup.....	56
3.4 Finite Element Analysis Setup.....	57
Chapter 4 Results and Discussions	60
4.1 Film Thickness Measurement & XRD Results.....	60
4.2 Indentation Impression (Sink-in & Pile-up) Characterizations	63
4.3 Film Young's Modulus and Critical Indent Depth Determination	68
4.4 Doerner & Nix Function Investigation	74
4.5 Alpha (α) Parameter Determination.....	82
4.6 Physical Explanation of α_1 and a_2 in Modified Doerner & Nix Function.....	103
Chapter 5 Conclusions	115
References	117

List of Tables

Table 2.1 Geometries of Different Indenter Tips.....	15
Table 3.1 Deposition Information for All the Specimens.....	51
Table 3.2 Selected Sputtering Parameters for Amorphous CrO _x	52
Table 4.1 h_{cr} , E_f , E_f , E_f/E_s , and h_{cr}/t for All Tested Specimens.....	71
Table 4.2 h_{cr}/t and E_f/E_s Data of NFC films with Different Thickness.....	73
Table 4.3 List of α_1 and α_2 Values for Each thin film with the Film Poisson's Ratio.....	94
Table 4.4 α in the Doerner & Nix Model and corresponding K and R values	108

List of Figures

Figure 2.1a Schematic of the Basic Components of a Nanoindenter	6
Figure 2.1b Image of a Nanoindenter XP System	7
Figure 2.2 Schematic of Load-Displacement Curve Obtained by Nanoindentation	8
Figure 2.3 Load-Displacement Curve of Bulk <111> Silicon.....	11
Figure 2.4 Load-Displacement Curve of Bulk Aluminum	11
Figure 2.5 A Load-Displacement Curve Showing a Nonlinear Unloading Portion	14
Figure 2.6 Schematic of a Nanoindentation Impression.....	15
Figure 2.7 Schematic of Continuous Stiffness Measurement.....	17
Figure 2.8 Load-Displacement Curve from a CSM Test.....	17
Figure 2.9 CSM modulus-displacement curve for bulk fused silica.....	19
Figure 2.10 Modulus-Displacement Curve for a SiO ₂ Thin Film on the Si Substrate.....	19
Figure 2.11 Modulus-Displacement Curve for a Si ₃ N ₄ Thin Film on the Si Substrate	20
Figure 2.12 Compliance vs. Reciprocal Contact Depth for Tungsten Film on Si	23
Figure 2.13 Comparison of Doerner & Nix and Gao's Weighting Factors	23
Figure 2.14 DLC <i>E-h</i> Data with Curves from Doerner&Nix and Gao's Functions	24
Figure 2.15 Alpha as a Function of Normalized Punch Size from King's Work	25
Figure 2.16 Indentations from a Flat Punch and the Effective Flat Tip for a Berkovich ..	26
Figure 2.17 Experimental and the Repression Values for the TbDyFe/Si Film on Si.....	29
Figure 2.18 Center of a Typical 2D Axisymmetric Mesh for Thin Film Indentation	32

Figure 2.19 Experimental and FEA Modulus vs. Displacement Curves of a-tC Film	33
Figure 2.20 Sink-in and Pile-up Profiles during Nanoindentation	35
Figure 2.21 SEM Image of a Pile-up Indentation Impression	37
Figure 2.22 Schematic of Pile-up and Sink-in Contact Areas during Indentation.....	38
Figure 2.23 AFM (a) Image and (b) Profile of a 750 Indentation on Al/Glass	38
Figure 2.24 Schematic Representation of the Projected Contact Area due to Pile-up	39
Figure 2.25 (P/S^2) vs. Indentation Depth for Fused Silica Film on Si Substrate.....	40
Figure 2.26 Various Deposition Systems for Thin Films	45
Figure 2.27 Schematic of RF PECVD and Plasma Sheath.....	46
Figure 3.1 Image of a Denton Sputtering System.....	53
Figure 3.2 Schematic of the RF PECVD System at Argonne National Lab.....	54
Figure 3.3 Image of a Jeol 5000 Atomic Force Microscope.....	55
Figure 3.4 Image of a Jeol 7000F Field Emission Scanning Electron Microscope	56
Figure 3.5 Schematic of the Finite Element Analysis of the Nanoindentation.....	59
Figure 4.1a Cross-sectional SEM Image of ta-C:H Film on Si Substrate	61
Figure 4.1b Composition SEM Image of the Cross-section of NFC/Si.....	62
Figure 4.2 X-ray Spectrum	63
Figure 4.3 SEM Image of an Indentation Impression on NFC/Si.....	65
Figure 4.4 AFM Images of a Sink-in Impression of 300 nm Indentation on NFC/Si	66
Figure 4.5 AFM Images of a Sink-in impression of 500 nm Indentation on ta-C:H/Si	66
Figure 4.6 AFM Images of (a) 300 nm and (b) 500nm Indentation on a-Si Film	67
Figure 4.7 CSM Modulus-Displacement Curves of (a) SiO ₂ and (b) Si ₃ N ₄ Films	70
Figure 4.8 h_{cr}/t vs. E_f/E_s for All Tested Specimens.....	72

Figure 4.9	Positions of the NFC Films with Different Thickness in h_{cr}/t vs. E_f/E_s	74
Figure 4.10	Experimental and Theoretical Curves of $h_{cr}/t-E_f/E_s$	76
Figure 4.11	SiO ₂ Modulus-Displacement Curve with Theoretical Curves.....	77
Figure 4.12	Plot of α Value at Critical Indentation Depth vs. E_f/E_s	79
Figure 4.13	Plot of α vs. h for NFC Film Contrasted with the $E-h$ Curve.....	80
Figure 4.14	Plot of α vs. h for SiO ₂ Film Contrasted with the $E-h$ Curve	81
Figure 4.15	Plot of α vs. h for ta-C:H Film Contrasted with the $E-h$ Curve.....	82
Figure 4.16	A Suggested Power Function of h for Alpha.....	83
Figure 4.17	Schematic of Certain Degree of the Elastic Strain Growth in the Specimen .	85
Figure 4.18	FEA Images of the Elastic Strain Distribution in NFC/Si Specimen.....	87
Figure 4.19	FEA Image of the Elastic Strain Distribution in ta-C:H/Si	90
Figure 4.20	FEA Result of Indenting 20 nm into (a) UNCD/Si and (b) Si/UNCD	91
Figure 4.21	Comparison of α_1-h data for SiO ₂ with the Doerner & Nix function	93
Figure 4.22	$E-h$ Curve of SiO ₂ Film with the new, Doerner&Nix, and Gao Models.....	95
Figure 4.23	$E-h$ Curve of a-Si Film with the new, Doerner&Nix, and Gao Models.....	95
Figure 4.24	$E-h$ Curve of FeB Film with the new, Doerner&Nix, and Gao Models.....	96
Figure 4.25	$E-h$ Curve of TiO _x Film with the new, Doerner&Nix, and Gao Models.....	96
Figure 4.26	$E-h$ Curve of AlN Film with the new, Doerner&Nix, and Gao Models	97
Figure 4.27	$E-h$ Curve of NFC Film with the new, Doerner&Nix, and Gao Models.....	97
Figure 4.28	$E-h$ Curve of FeO _x Film with the new, Doerner&Nix, and Gao Models	98
Figure 4.29	$E-h$ Curve of AlO _x Film with the new, Doerner&Nix, and Gao Models	98
Figure 4.30	$E-h$ Curve of CrO _x Film with the new, Doerner&Nix, and Gao Models	99
Figure 4.31	$E-h$ Curve of SiC Film with the new, Doerner&Nix, and Gao Models	99

Figure 4.32 <i>E-h</i> Curve of Si ₃ N ₄ Film with the new, Doerner&Nix, and Gao Models	100
Figure 4.33 <i>E-h</i> Curve of ta-C:H Film with the new, Doerner&Nix, and Gao Models ..	100
Figure 4.34 <i>E-h</i> Curve of Metglas Film with the new, Doerner&Nix, and Gao Models	101
Figure 4.35 <i>E-h</i> Curves of (a) Polymer and (b) UNCD Films with the New Model.....	102
Figure 4.36 Effective Elastic Strain Volume Developed during Nanoindentation.....	104
Figure 4.37 Important Parameters for the Spherical Segment.....	105
Figure 4.38 Comparison of the D&N Factor and the Analytical Model from Eq. (22)...	107
Figure 4.39 Plot of (a) <i>I/K</i> vs. α and (b) <i>R</i> vs. α for a 10 nm Indentation	109
Figure 4.40 Comparison between 1- α and 2- α Models.....	110
Figure 4.41 Radius of the Elastic Strain Boundary vs. Alpha1 & Poisson's Ratio	111
Figure 4.42 Schematic of an Indentation Impression in the Film.....	113
Figure 4.43 Elastic Strain Distributions in the Films with Different Poisson's Ratios ...	114

List of Abbreviations

DLC	Diamond Like Carbon
NFC	Near Frictionless Carbon
CSM	Continuous Stiffness Measurement
UNCD	Ultrasmall Nano-Crystalline Diamond

CHAPTER 1

INTRODUCTION

1.1. Synopsis

In the last three decades, Instrumented Indentation Testing (IIT), also known as depth sensing indentation, has become one of the most important methods for the mechanical characterizations of bulk and thin film materials [1-66]. As the world has been more and more inspired by the nano-scale materials and devices, instrumented indentation, inexorably, followed this “expanding” trend. From micro-scale to the nano-scale regime, nanoindentation has been widely used to determine the Young’s modulus, hardness, fracture strength, residual stress and other important mechanical properties of extremely small systems, such as ultra-thin films, nanowires, nanoparticles, NEMS, and bio-nanomaterials [20,29,37,47,50]. However, several key issues have limited the use of nanoindentation, or more precisely, prevented it from obtaining accurate information of the target materials [10,16,67-69]. For instance, thin film substrate effects have always complicated measurements as the indentation is influenced by m both the film and the substrate. Eliminating substrate effects and deriving the true mechanical properties of the film are essential and urgent for the development of nanomaterials and nanotechnology, as well as greatly improve the comprehension of the elastic and plastic deformation growth in thin films.

Ever since nanoindentation was applied to thin films, there have been efforts to eliminate substrate effects. Many outstanding researchers have used both experimental and theoretical methods to study this subject [8,10,13,15,18,70-72]. However, due to the complexity from other nanoindentation effects, such as film microstructures and pile-up/sink-in situations, the veil on the substrate effect has not been fully uncovered. Thus, this research followed the significant work of Nix, Doerner, Gao, Oliver, Pharr, and others to investigate and better understand the mechanism behind the substrate effect. In this work, 15 thin films (14 amorphous and 1 nanocrystalline films) were deposited and tested with the Nanoindenter. The selection of amorphous structure was aimed at eliminating the microstructure effects so that the substrate effect could be decoupled from them. A physical explanation was found for an existing empirical function of the substrate effect. By improving this function, it was able to derive the true film modulus from the nanoindentation data. One unique result in this research was to find that the Poisson's ratios of the film and the substrate played important roles for determining substrate effects and how they manifested the composite modulus measured by the nanoindentation.

1.2. Dissertation Structure

Chapter 2 gives literature reviews to all the subjects that are related to this dissertation work. It includes nanoindentation, continuous stiffness measurement (CSM), substrate effects, finite element analysis of nanoindentation, pile-up/sink-in phenomenon, film microstructure effects, thin film deposition, and the X-ray

diffraction technique. In the nanoindentation part, an overview of instrumented indentation theory was given. Two different indentation methods: static and dynamic measurements were covered in this section. The relation between the Continuous Stiffness Method (dynamic) and the substrate effect was explained in detail. Substrate effects were the most important part of this research, and were thus covered in significant detail. Finite element analysis played a large role in substrate effects indication in this study. Useful simulation results from other researchers were illustrated. Pile-up/sink-in and film microstructure, which were two other important nanoindentation effects, were also covered in this chapter. Thin film deposition techniques and deposition mechanisms were discussed based on how to obtain the amorphous structure. X-ray diffraction theory was briefly introduced for the film structure determination.

Chapter 3 covers the experimental setup of this research, which consist of three parts: 1. Thin film deposition and characterization; 2. Nanoindentation measurements; 3. Finite element analysis setup.

Chapter 4 deals with the final results and discussions. The experimental data from nanoindentation were calibrated for all the amorphous thin films. Young's modulus (E) - Indent depth (h) curves were obtained from the continuous stiffness measurement (CSM) so as to investigate the starting point of substrate effects. The so-called "flat region" (with minimum substrate effects) was observed in the early stage of nearly every E - h curve for all materials studied. The depth of this region (h_{cr}) was found to vary with the material in a non-linear fashion. Based on the

experimental data and simulation results, we were able to modify the Doerner & Nix empirical function for thin film indentation on a substrate, particularly their parameter alpha (α). A mathematical model of the elastic strain energy distribution was established to support the new theory. The original alpha was replaced with two new parameters that were equal to the film and substrate Poisson's ratio. The modified relation was found to be adept at closely matching all experimental data collected, which spanned both soft films on hard substrates and hard films on soft substrates.

Chapter 5 provides conclusions and future work.

CHAPTER 2

LITERATURE REVIEW

2.1. Instrumented Indentation Testing

Instrumented indentation testing (IIT), also known as nanoindentation, is achieved using a high-resolution system that can drive an indenter tip made of diamond into and withdraw it from a sample material [10,16,29]. During the process, the loads and displacements of the tip are recorded by positional sensors, from which mechanical properties can be derived. In the past few decades, this technique has been developed sufficiently to satisfy the increasing needs of nano-scale materials and devices characterizations. Nanoindentation has two major advantages: (1) The mechanical properties of nanowires and NEMS are usually very difficult to determine by conventional tensile tests. Through nanoindentation, the Young's modulus and hardness can be calculated from the load-displacement curve. Other important properties like yield strength, fracture strength, residual stress can be estimated using nanoindentation related methods [24,36,62,73-80]. (2) Another key advantage is that nanoindentation does not have strict requirements on specimen's shape, scale, and surface conditions (especially for bulk materials). As the indenter tip has a radius less than 50 nm, the technique is extremely useful to examine ultra-thin films and coatings.

Figure 2.1a and 2.1b show the schematic and an image of an indentation system [29]. There are three basic components of a Nanoindenter: an indenter tip, an actuator for applying forces, and a sensor for recording the indent depth. The indentation process consists of two stages: loading and unloading. During loading, the indenter tip is driven into the material, where both elastic and plastic deformations occur. When the tip is unloaded from the sample, only the elastic recovery occurs, which effectively separates the elastic properties of the materials from the plastic. A typical load-displacement curve is illustrated in figure 2.2 [50].

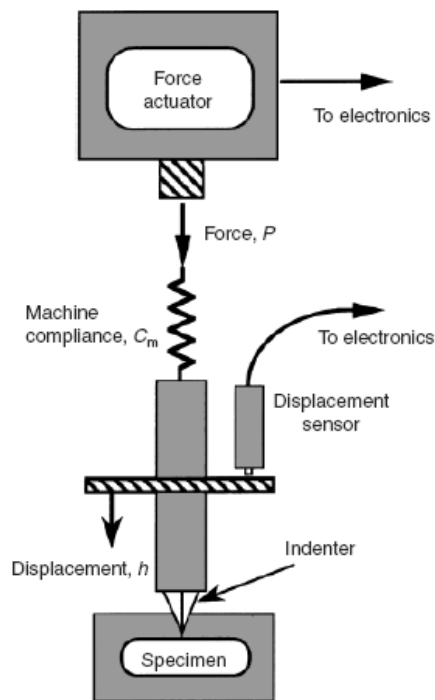


Figure 2.1a Schematic of the basic components of a Nanoindenter [29]



Figure 2.1b Image of a Nanoindenter XP system

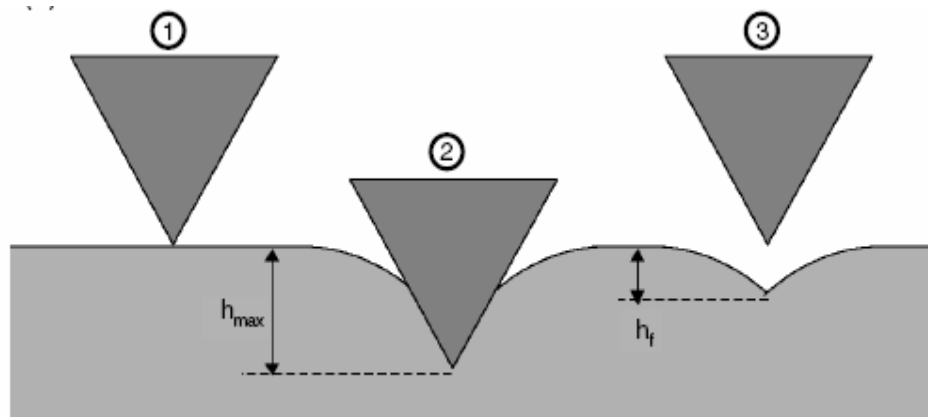
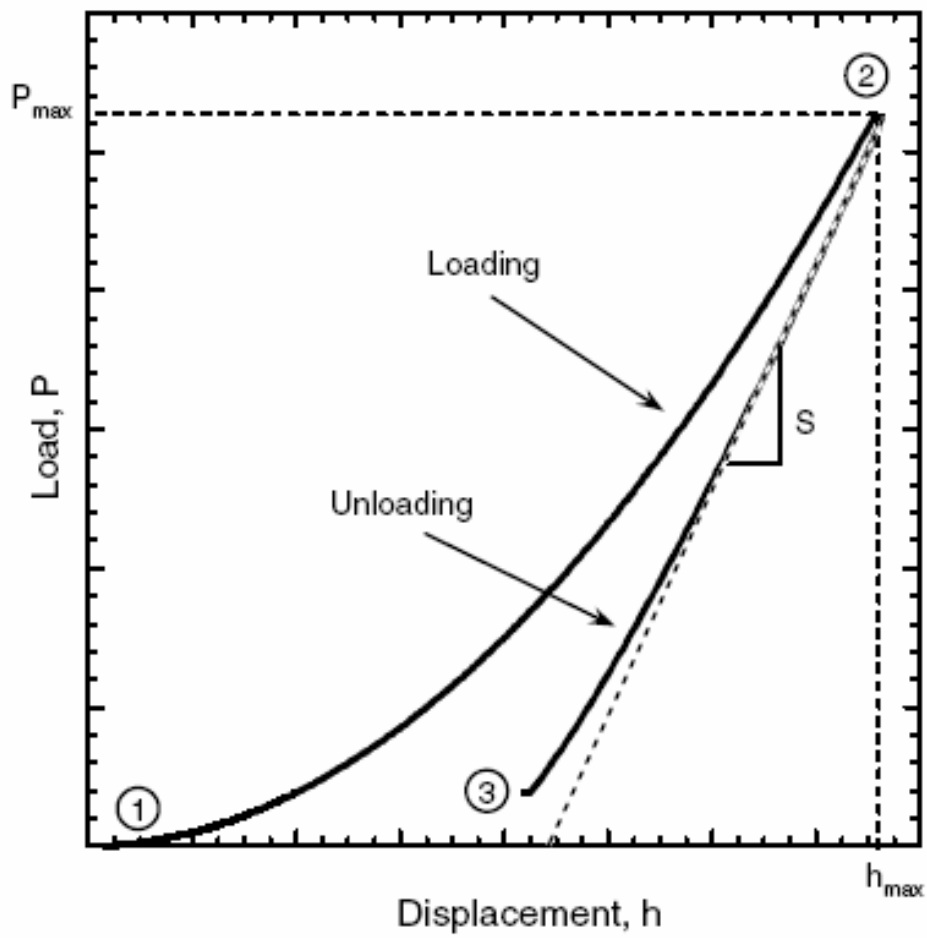


Figure 2.2 Schematic of the typical load-displacement curve obtained by

nanoindentation [50]

The earliest load-displacement sensing indentation experiments can be retraced to 1940s. Tabor performed indentations on several metals using a spherical indenter[1]. An interesting result was that the hardness impression on samples after unloading was indenter shape related. In other words, a round shape impression was caused by a spherical tip. Same results were obtained by Stillwell from a conical tip [2]. More importantly, they found the existence of elastic recovery during unloading. They showed the evidence that the shape of the unloading curve and the elastic recovering displacement were related the elastic modulus.

Their research also led to the understanding that the reduced (measured) Young's modulus (E_r) from indentation accounted for the elastic displacement occurring in both the indenter and the specimen. The effect can be represented by the following equation:

$$\frac{1}{E_r} = \frac{1-\nu^2}{E} + \frac{1-\nu_i^2}{E_i} \quad (1)$$

Where E and ν are the Young's modulus and Poisson's ratio of the specimen, E_i and ν_i are Young's modulus and Poisson's ratio, respectively of the indenter. For a typical diamond tip, $E_i = 1141$ GPa, and $\nu_i = 0.07$ [1,2].

In the 1970s, researchers started to show interest in the roles of the unloading curve slope (S) and the projected indentation contact area (A) in the Young's modulus and hardness determination. The representative work in this decade was from Bulychev and co-workers [4]. They found a relationship between the reduced modulus and the two parameters mentioned above:

$$S = \left(\frac{dP}{dh} \right) = \frac{2}{\sqrt{\pi}} E_r \sqrt{A} \quad (2)$$

Where S is the stiffness of the upper portion of the unloading curve, P is the load, and h is the displacement.

The term “nanoindentation” was first used in 1980s. In this decade, researchers began to realize the importance of instrumented indentation in thin film characterizations. Pethica, Hutchings, and Oliver proposed a simple method for modulus calculation [8]. They suggested that the contact area (A) in Eq. 2 can be estimated as a function of the final indent depth (h_f).

Loubel and co-workers proposed an idea of deriving the Young’s modulus from IIT in 1984 [9]. They suggested that E could be derived from the initial slope of the unloading curve, i.e. the indentation load as the function of the indentation depth.

For a spherical indenter, the slope can be represented as:

$$S = \left(\frac{dP}{dh} \right) = 2r_0 E_r \quad (3)$$

where r_0 is the radius of the punch. The idea was sensible as the loading portion of the test has a complex combination of plastic-elastic deformation. The initial unloading then would be only composed of elastic response, and thus contain only the elastic information from the specimen to calculate the Young’s modulus. This idea was supported empirically by several tested metals that exhibit that the initial part of the unloading curve was linear, and the rest of the unloading curve was non-linear, see figure 2.3 and 2.4 for the load-displacement curve of <111> silicon and aluminum and aluminum [10].

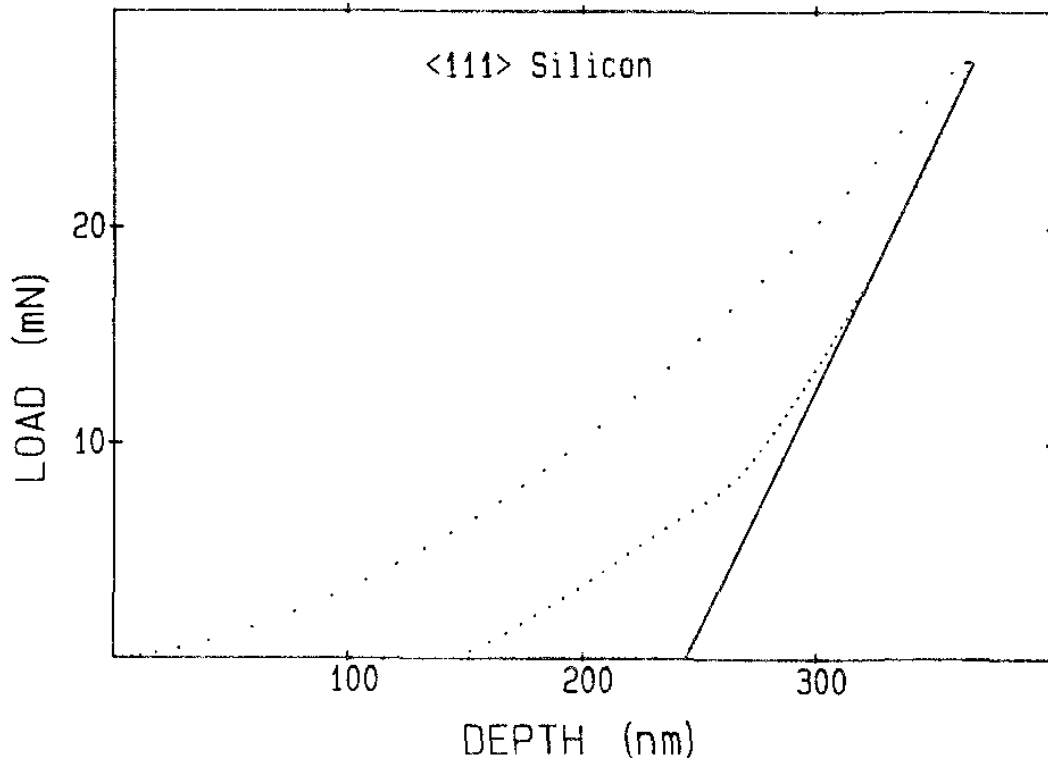


Figure 2.3 Load-Displacement curve of bulk <111> Silicon [10]

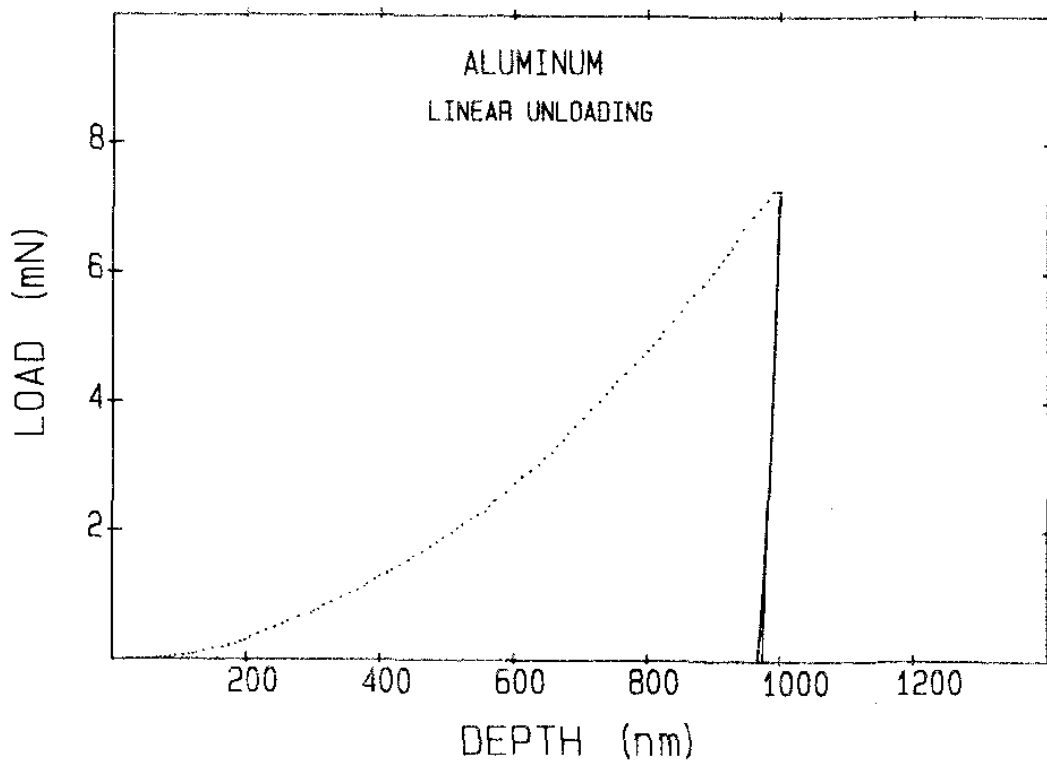


Figure 2.4 Load-Displacement curve of bulk Aluminum [10]

This theory was improved and expanded by Doerner and Nix in 1986 [10]. They proposed a relatively comprehensive method for interpreting the data from indentation. They assumed that the Young's modulus was related to the initial slope of the unloading curve and the indentation depth. They also calculated the hardness of the film by subtracting the elastic displacement from the total displacement of indentation. The hardness equation is shown as:

$$H = \frac{P_{\max}}{A} \quad (4)$$

where P_{\max} is the peak indentation load and A is the projected contact area.

Moreover, they suggested that there was a “substrate effect” on the measured composite modulus for a film/substrate specimen during indentation [10]. They believed that during unloading, the elastic response was not only from the information of the film but also from the substrate. They suggested an empirical function of the indent depth to describe the film and substrate contributions to the measured young's modulus. Also, King supported Doerner & Nix by performing simulation of thin films [13]. Gao built up a mathematical model for the thin film indentation [15]. Their work has affected the nanoindentation theory for more than 15 years. As the Doerner & Nix/King function and Gao's model are vital to this study, they will be explained in detail in the later section.

In the 90s, Oliver, Pharr and co-workers were the leaders in the nanoindentation field. They proposed the famous Oliver & Pharr method for determining bulk materials hardness and elastic modulus from micro/nano indentation in 1992 [16]. As mentioned above, their work in investigating the IIT method began in

early 1970's. After years of accumulating indentation data on different materials, they questioned Loubel, Doenar, and Nix's assumption about the linear region at the initial unloading curve. They found that for most materials, the unloading curve was completely nonlinear (see figure 2.5 for a nonlinear unloading curve). Their solution was to fit the unloading curve of the load-displacement data with a power-law relation (eq. 5) [16]:

$$P = B(h - h_f)^m \quad (5)$$

where B and m are empirically determined parameters and h_f is the final displacement after complete unloading of the indenter tip.

. From the equation above, S can be derived as :

$$S = \left(\frac{dP}{dh} \right)_{h=h_{\max}} = Bm(h_{\max} - h_f)^{m-1} \quad (6)$$

The equations of reduced Young's modulus (E_r) and hardness calculation (H) are given as:

$$E_r = \frac{\sqrt{\pi}}{2\beta} \frac{S}{\sqrt{A}} \quad (7)$$

$$H = P / A \quad (8)$$

where A is the projected contact area of contact under load, and β is a constant that depends on the geometry of the indenter tip. The projected area is calculated by evaluating an empirically determined indenter area function $A=f(h_c)$ at the contact depth. This area function is also known as the tip shape function. It is related to the geometry of the indenter. For a perfect Berkovich tip, A can be represented as:

$$A = 24.56h_c^2 \quad (9)$$

It needs to mention that in practical use, the tip geometry will not be perfectly sharp.

Thus a calibration of the contact area needs to be introduced using:

$$A = 24.56h_c^2 + C_1h_c^1 + C_2h_c^{1/2} + C_3h_c^{1/3} + \dots \quad (10)$$

where C_i are the fitting constants.

Oliver and Pharr were the first to suggest (A) as function of h_c instead of h_f . The contact depth (h_c) is usually smaller than the displacement (h) for a sink-in situation ($h_c > h$, when pile-up). Figure 2.6 shows the schematic of a section through an indentation and the relationships between various parameters. In Oliver & Pharr's method, the contact depth is estimated as[16]:

$$h_c = h - \varepsilon \frac{P}{S} \quad (11)$$

where ε is a constant that depends on the indenter geometry. Nowadays, most of the Nanoindenter systems use the Oliver & Pharr method to calculate the materials mechanical properties.

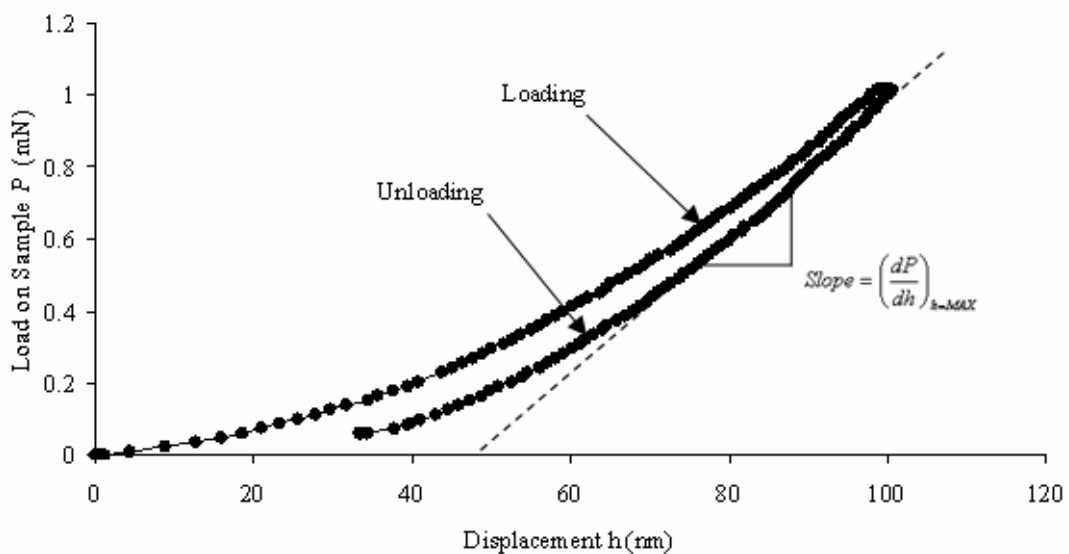


Figure 2.5 A load-displacement curve showing a nonlinear unloading portion

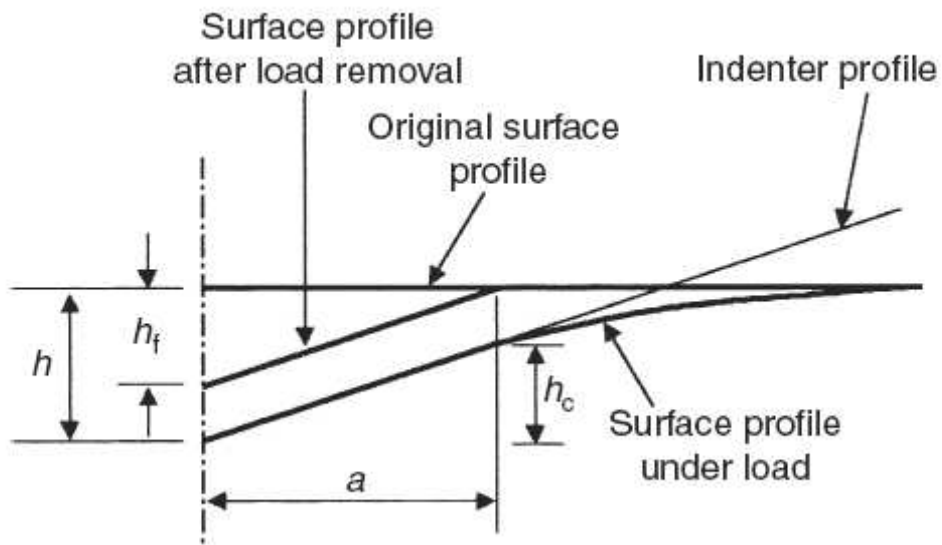







Figure 2.6 Schematic of a nanoindentation impression [16]

Indenters with various shapes are used for different purposes. Pyramidal indenters also well known as Berkovich tips are probably the most frequently used shape. The three-sided pyramid can ground to a very small point, which will keep its geometry to the minimum scales. Besides the Berkovich tip, spherical, cube-corner, conical, and Vickers pyramid indenters are also applied. Table 2.1 shows their geometries and parameters [50].

Table 2.1 Geometries of different indenter tips [50]

Parameter	Berkovich	Cube-corner	Cone	Spherical	Vickers
Shape					
C-f angle	65.35°	35.264°	—	—	68°
Projected Contact area	$24.5600d^2$	$2.5981d^2$	πa^2	πa^2	$24.5044d^2$

2.2 Continuous Stiffness Measurement

Other than the traditional static nanoindentation method, the continuous stiffness measurement (CSM), also known as dynamic stiffness measurement, allows one to determine the Young's modulus and hardness along with the displacement [29,37]. This alternative of nanoindentation is ideal for very thin film characterizations due to the sensitivity of the indent depth. Basically, CSM is no different from the static methods. A typical CSM test can be seen as a set of the static indentations at the same location but with increasing indent depths. This is accomplished by superimposing a small force oscillation on the primary loading signal and analyzing the resulting displacement response using a frequency-specific amplifier, see figure 2.7 [37]. Thus, it allows continuous measurement of stiffness as the tip is driven into the specimen. A typical CSM loading circle is shown in figure 2.8 [37].

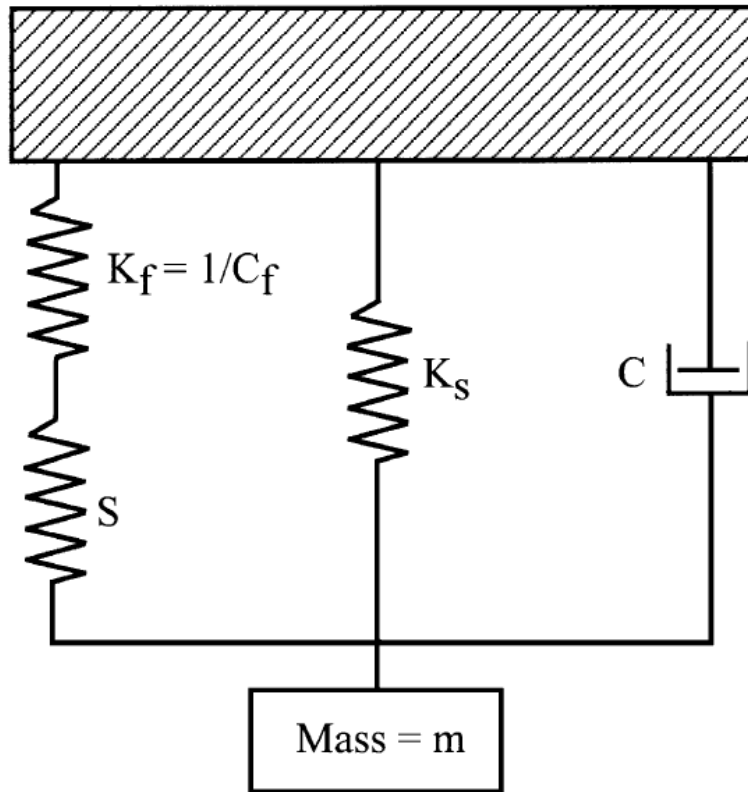


Figure 2.7 Schematic of continuous stiffness measurement [37]

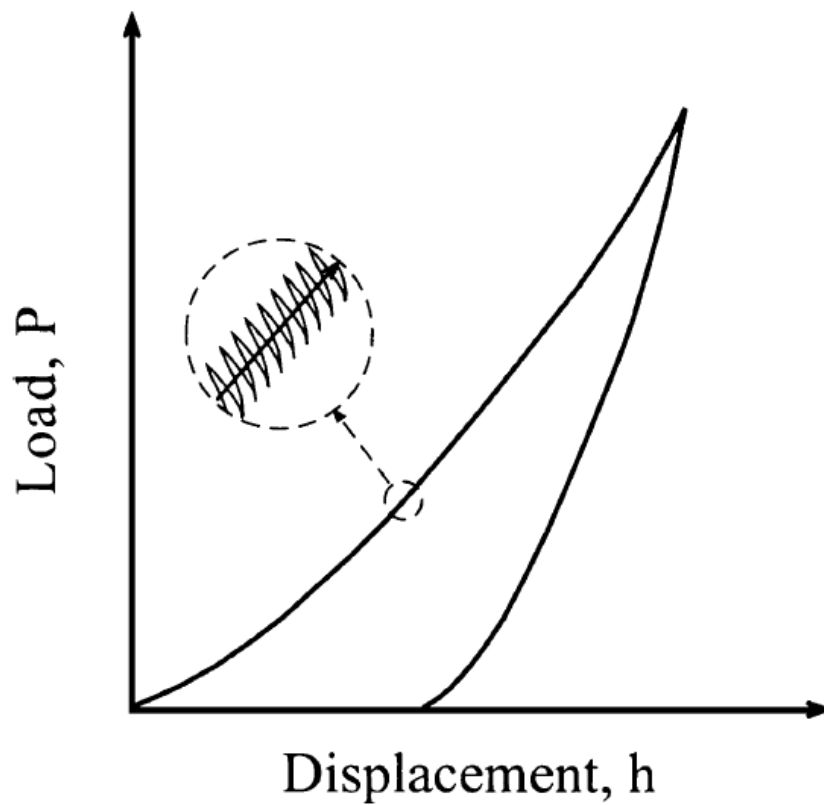


Figure 2.8 Load-displacement curve from a CSM test [37]

CSM has numerous advantages over a single static indentation. First, it can be used to evaluate the fatigue in nano-scale thin films and materials. Also the small time frame of each indentation in CSM makes it ideal for measuring the mechanical properties of polymeric materials. Measurements on multilayer (more than a single film) structures and graded materials can also be benefited from the continuous method. Furthermore, recent works show that creep measurements of the nanoscale materials can be performed by monitoring the change in stress-displacement relation in CSM tests [37].

Applying CSM tests on bulk and thin film materials lead to different results. Figure 2.9 and 2.10 show the Young's modulus-displacement curves of bulk silica and SiO₂ thin film on a Si substrate, respectively. As one can imagine, the curve for a bulk material will be a straight line which shows the bulk elastic modulus. However, for a thin film system, the measured modulus represents a composite value containing both the film (E_f) and the substrate (E_s) information. For SiO₂ on Si, E_{comp} starts as a relatively small value that is closed to E_f . The curve sustains relatively flat for a short period and then increases with the displacement towards E_s . The CSM curve gives us a clear vision that the substrate effects increase as the indenter goes deeper into the film. The CSM E-h curves vary with film and substrate properties. For instance, when a soft film in on a hard substrate, the curve has a rising trend, while as a hard film on a soft substrate, the curve will decrease (see figure 2.11 for a Si₃N₄ film on the Si substrate). The unique relation between the substrate effect and E-h curve makes CSM an extreme valuable tool for thin film mechanical characterizations.

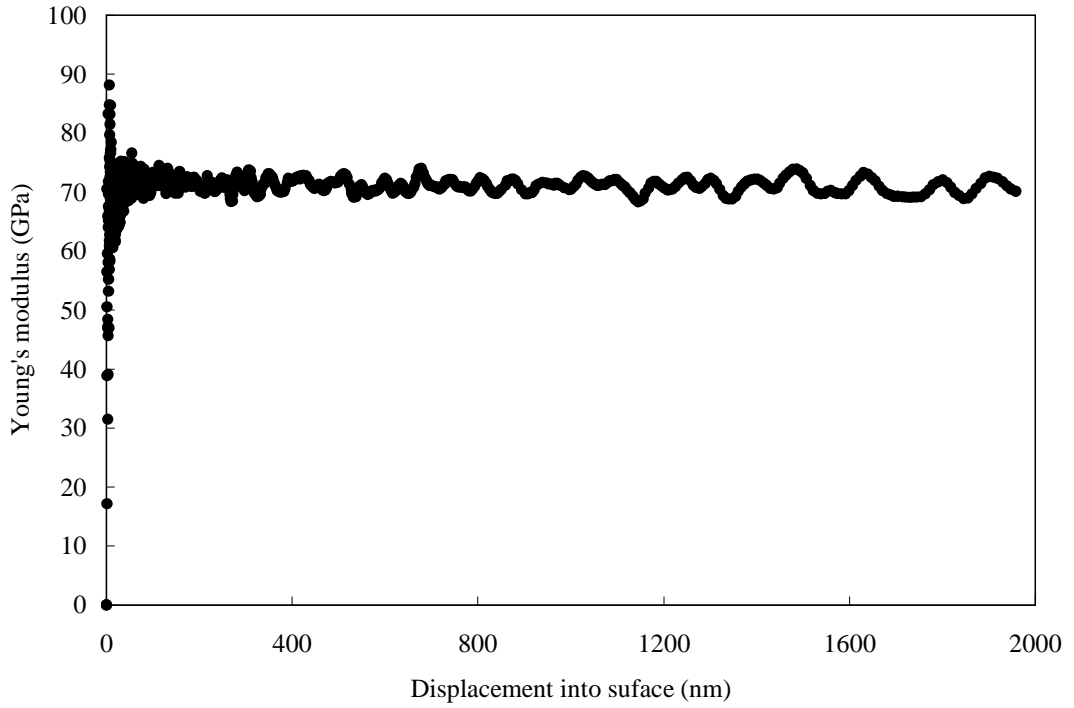


Figure 2.9 CSM modulus-displacement curve for bulk fused silica

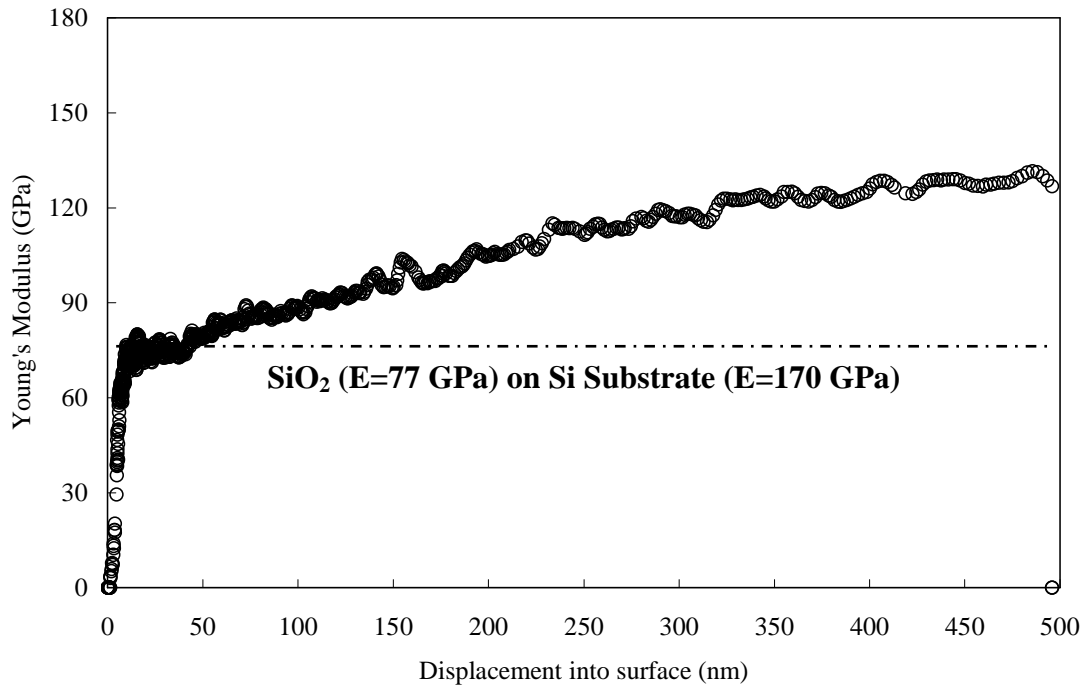


Figure 2.10 CSM modulus-displacement curve for a SiO₂ thin film on the Si Substrate

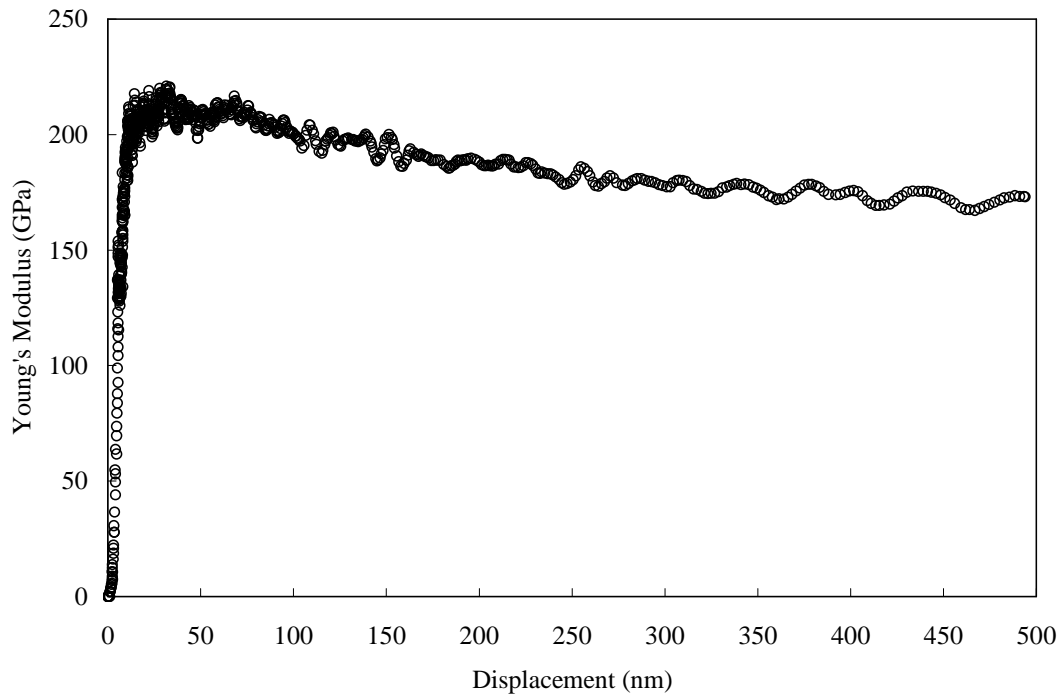


Figure 2.11 CSM modulus-displacement curve for a Si_3N_4 thin film on Si substrate

2.3 Thin film substrate effects

In recent years, as instrumented indentation moved from micro-scale to the nano-scale regime, new issues have arose in interpreting nanoindentation data. Among them, the substrate effects in thin films, film pile-up/sink-in effects, and the film microstructures are the three key issues [50].

As mentioned in the last section, while using nanoindentation, the measurement of thin film properties is much more difficult than bulk materials because the indentation unloading data consists of both film and substrate responses. The mechanism of this phenomenon was believed to result from the different mechanical properties (Young's modulus, hardness, Poisson's ratio, etc) of the film and the substrate [10,13,15,71]. As one can imagine, when a hard film is on a soft

substrate, the modulus will be reduced from the true film value towards the substrate value with increasing indent depth. The opposite trend will occur when a soft film is deposited on a hard substrate.

The substrate effects will largely influence the accuracy of the film mechanical properties. An often used guideline recommended by Bückle is that if the indent depth is less than 10% of the film thickness, the substrate can be neglected [3]. Based on this, researchers like Doerner, Nix and King suggested there was always a “flat region” in the early stage of the CSM nanoindentation test, where the substrate effect could be minimum, and the values indicated the true film Young’s modulus. A typical flat region in the Young’s modulus-displacement curve is shown in figure 2.10 and 2.11. The idea about indenting 10% of the thickness was obtained from the micro or even larger scale indentation tests [3]. Based on recent studies, though the guideline can still fit most of the cases, it is not always true, especially when the film is much softer or harder than the substrate [72]. Also as the film thickness shrinks down to nanometer scales, the surface condition effect becomes vital for the first few tens nanometer indentation. Thus, simply using 10% rule might lead to an inaccurate property value. A more comprehensive, detailed and systematic method needs to be found to evaluate substrate effects.

Doerner and Nix were the first to describe the substrate effect using an empirical function. In their work, Doerner and Nix performed nanoindentation on tungsten sputtered on Si. They plotted the compliance as a function of the reciprocal displacement as shown in figure 2.12 [10], and a unique relation was found. Based on

their data, Doerner and Nix suggested a solution for the nanoindentation effective modulus-displacement curve, as shown below [10]:

$$\frac{1}{E} = \frac{1}{E'_f} + \left(\frac{1}{E'_s} - \frac{1}{E'_f} \right) e^{-\alpha(t/h_c)} \quad (12)$$

where E is the measured Young's modulus, $E'_f = E_f / (1 - \nu_f^2)$, $E'_s = E_s / (1 - \nu_s^2)$, t is the film thickness, h_c is the indenter tip contact depth, and α is an empirically determined constant for all the materials, which Doerner and Nix suggested a value of 0.25. Although, it doesn't have a physical background, the function works relatively well with most of the thin film materials. The Doerner & Nix weight factor $\exp(-\alpha t/h_c)$ is a sigmoid-shaped curve. As shown in figure 2.13 as a function of h_c , this factor increases from 0 and reaches 1 in infinity. This factor properly describes the influence of the substrate along with the indent depth. And figure 2.14 shows how the Doerner & Nix function fits the experimental data from CSM nanoindentation.

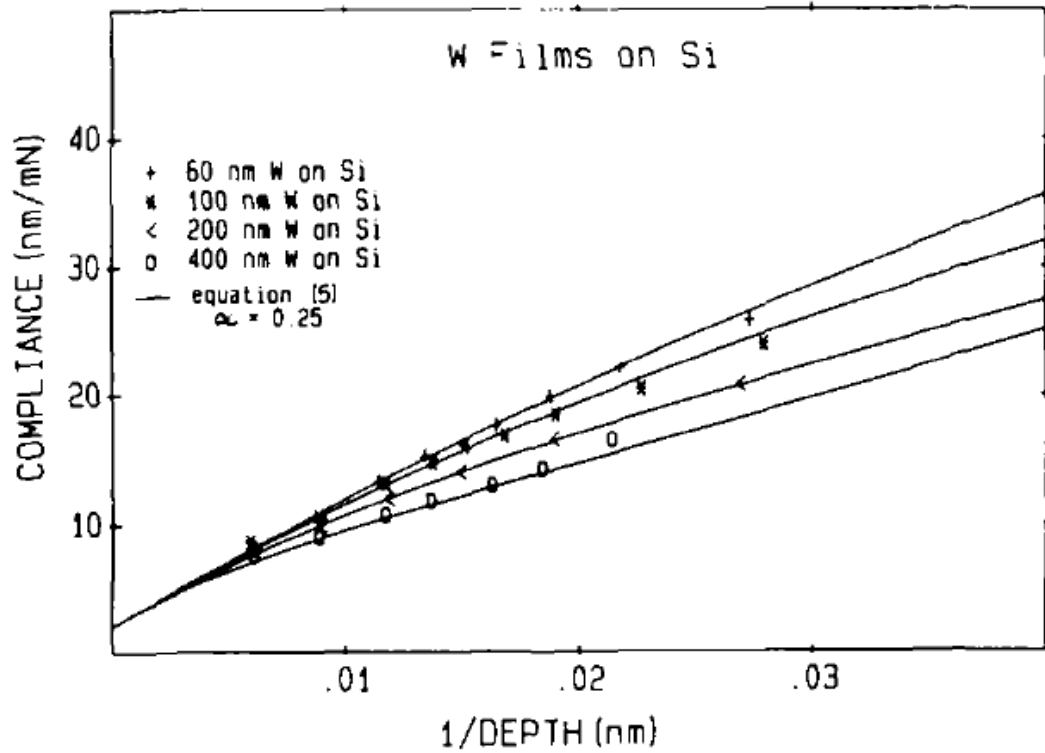


Figure 2.12 Compliance vs. reciprocal contact depth for tungsten film on Si [10]

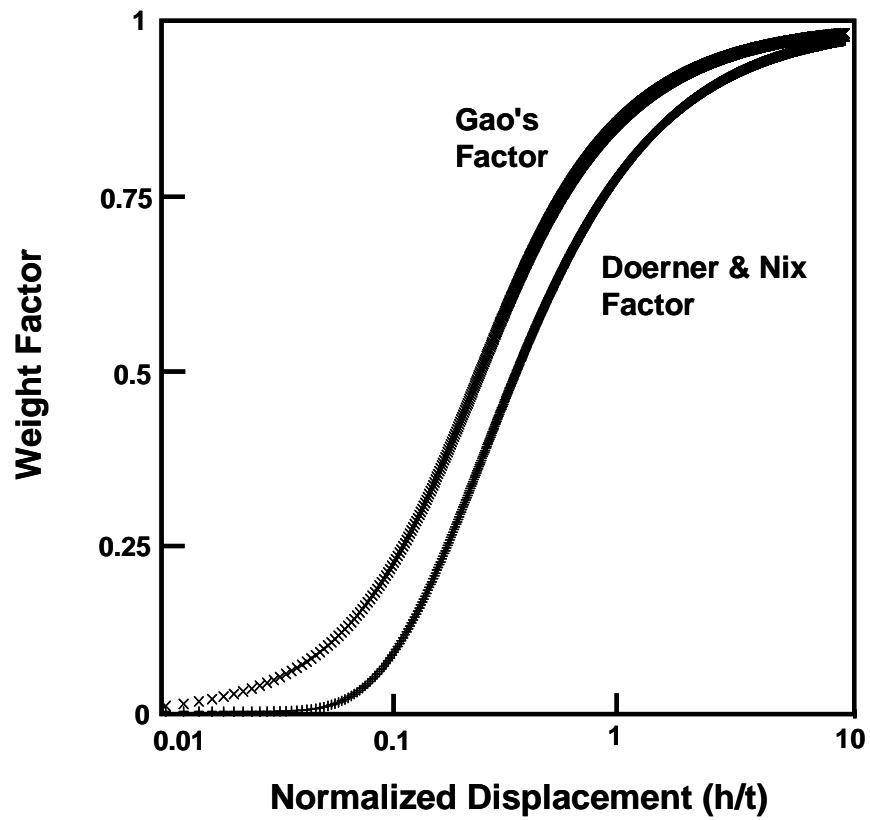


Figure 2.13 Comparison of Doerner & Nix and Gao's weighting factors

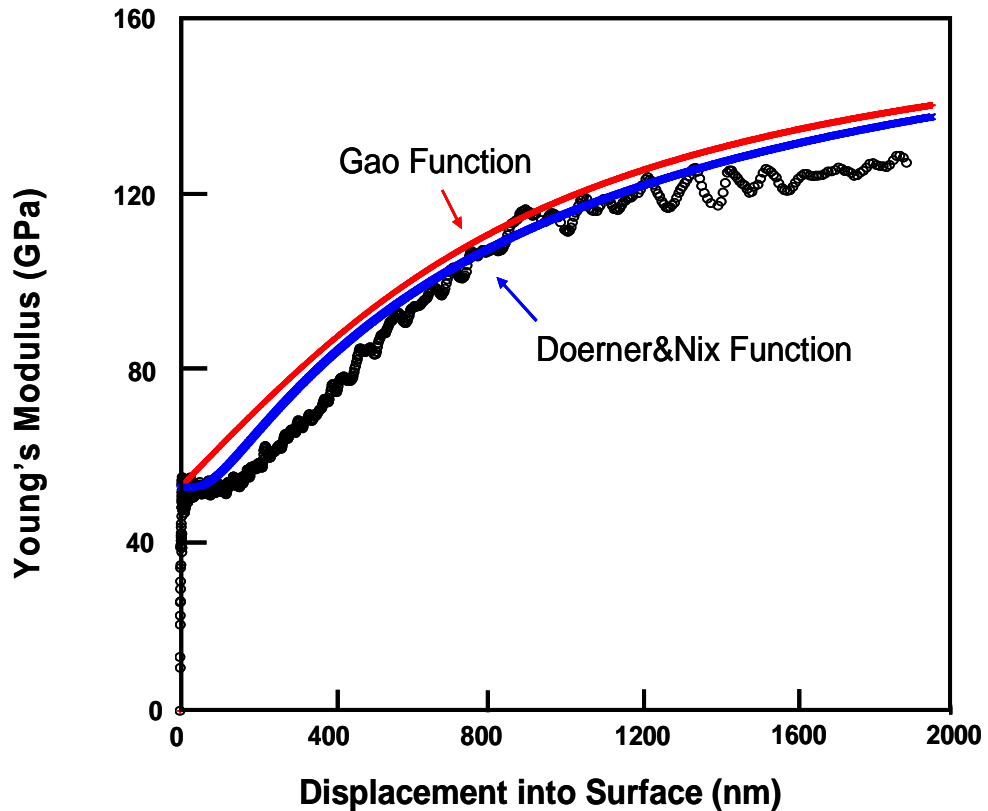


Figure 2.14 DLC $E-h$ data with theoretical curves from Doerner & Nix and Gao's functions

King supported Doerner & Nix's work by using finite element analysis [13]. In his work, he replaced h_c in Doerner & Nix function by the square root of the projected contact area a so as to take the indenter geometry into consideration. Three major indenter geometries were considered in his study: sphere, square, and triangle. The theoretical procedure used by King's simulation was for analyzing elastic normal contact problems for layered media. The simulation results were in certain agreement with Doerner & Nix. However, there was a major contribution in King's paper that was against the old work. It was found by simulation that the parameter alpha (α) in Doerner & Nix function was not a constant as claimed "0.25", but changed with the

contact area (depth), see figure 2.15. Doerner & Nix and King's model often gives satisfying results for those films that have a flat region in their early $E-h$ curves. However, it is not without problems. The alpha parameter changes with the displacement, which might leads to inaccurate data. Also only one variable in the function makes it inflexible in fitting experimental data.

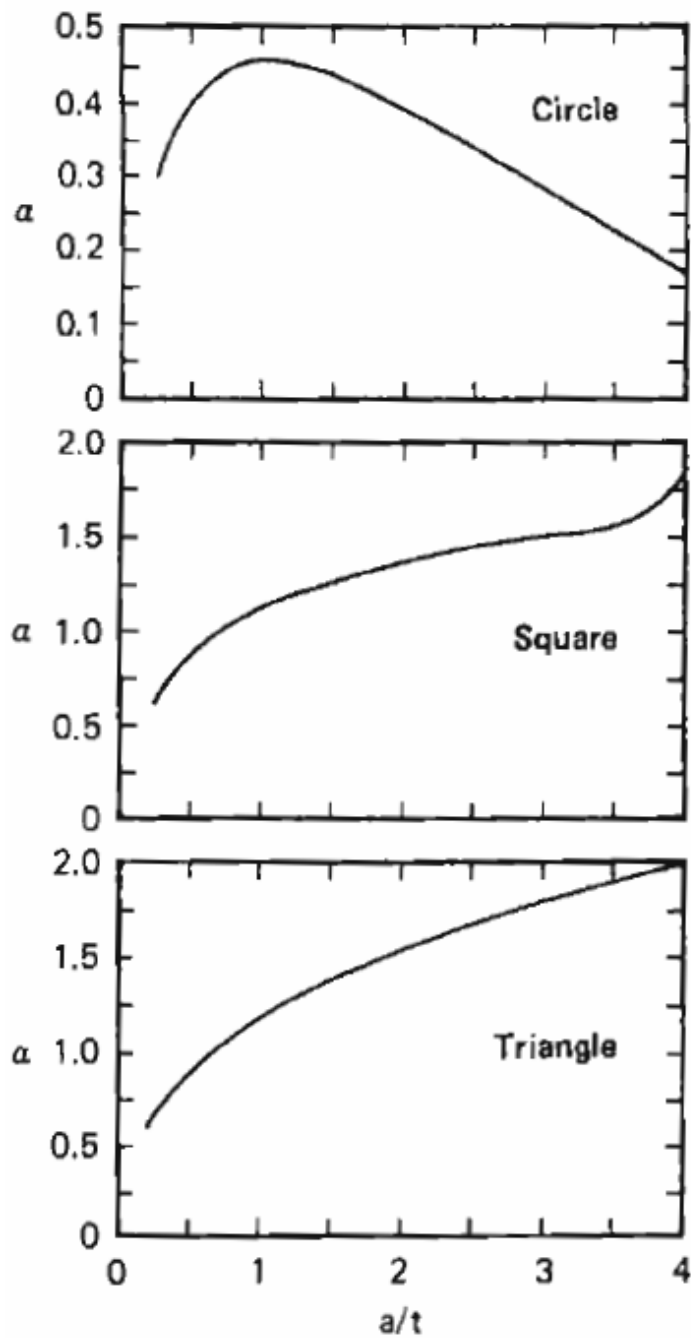


Figure 2.15 Alpha as a function of normalized punch size from King's work [13]

Efforts have been made to improve the Doerner & Nix function. Based on King's simulation results [21,26,34,39]. Saha and coworkers modified the old function to calculate the thin film Young's modulus [39]. King assumed a flat triangular punch in his analysis, but Doerner & Nix's data was from a pyramid-shape Berkovich tip. Saha connected two efforts by introducing the effective film thickness "t-h" to replace t in the old function as shown in figure 2.16. The modified function is:

$$\frac{1}{E} = \frac{1}{E_f} + \left(\frac{1}{E_s} - \frac{1}{E_f} \right) e^{-\alpha \frac{(t-h_c)}{a}} \quad (13)$$

The modified function fits well as the indent depth is less than 50% of the film thickness. However, the predicted reduce modulus greatly deviates from the experimental value. This is because changing the Berkovich tip to an "effective" flat punch will greatly overestimate the contribution of the substrate stiffness at large indent depth.

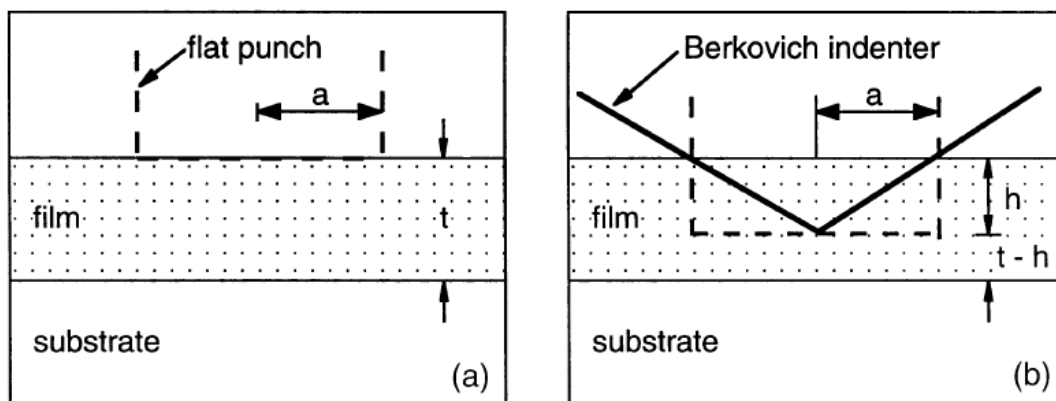


Figure 2.16 Indentations from a flat punch and the effective flat tip for a Berkovich

[39]

Another important study in this field was from Gao and his co-workers [15]. Quite different from the theoretical procedure that King employed in his work, Gao focused on the total energy transformation from the indenter to a thin film/substrate system during nanoindentation. Their idea was simple but intuitive: considering the elastic contact problem, the film/substrate system can be seen as a homogeneous body made of the substrate material with a phase transformation layer at the surface. Based on the energy conservation theory, they derived a mathematical solution from a rigid cylindrical stick punching into a semi-infinite elastic body with a different surface layer. The function was shown as below:

$$E = E_s + (E_f - E_s)\Phi \quad (14)$$

where Φ is the weighting factor that depends on the ratio of film thickness and contact area radius. The Gao's factor is shown as:

$$\Phi = \frac{2}{\pi} \arctan(x) + \frac{1}{2\pi(1-\nu)} \left[(1-2\nu)x \ln \frac{1+x^2}{x^2} - \frac{x}{1+x^2} \right] \quad (15)$$

Where $x=t/a$. t is the film thickness, a is the radius of the contact area, and ν is the Poisson's ratio. Also, as mentioned above, a is a function of the contact depth h_c .

Like Doerner & Nix factor, Eq. 15 is a sigmoid-shape function that increases from 0 and reaches 1 when a or h_c is close to infinity. These two factors were compared and contrasted in figure 2.13. It is easy to find the major difference is at the early stage of indentation. The Doerner & Nix factor has a small flat region, while Gao's factor almost increases from the beginning. This leads to different justifications

for the substrate effect during nanoindentation. Gao's model suggests that the substrate effect becomes prominent as soon as the indenter touches the film, while Doerner & Nix function assumes there will be a small displacement in the early stage that reflects the true film modulus. This is the reason why Gao's model always fits well with the specimens that have the measured modulus changing from the start, i.e. diamond film on Si substrate. Gao's mathematical derivation was almost flawless, but the model is a little arbitrary. For instance, regardless the trend of the measured modulus, as long as the indent depth/film thickness is equal to 0.85, the measured E is equal to $(E_f + E_s)/2$.

In recent years, there were many empirical and analytical solutions for modeling the nanoindentation substrate effects [17,18,21,31,32,41,81]. However, most of them were not tested with a wide range of materials with different modulus. A notable exception was made by Menick and co-workers [21]. They investigated the substrate effects by experimentally testing with several groups of thin film materials. Based on the data, they compared and contrasted five major expressions for thin film indentation including Doerner & Nix and Gao's functions (figure 2.17a and 2.17b). However, one concern was that those materials all had different microstructures. The film microstructures are known to greatly influence the nanoindentation data, and thus might lead to inaccurate data

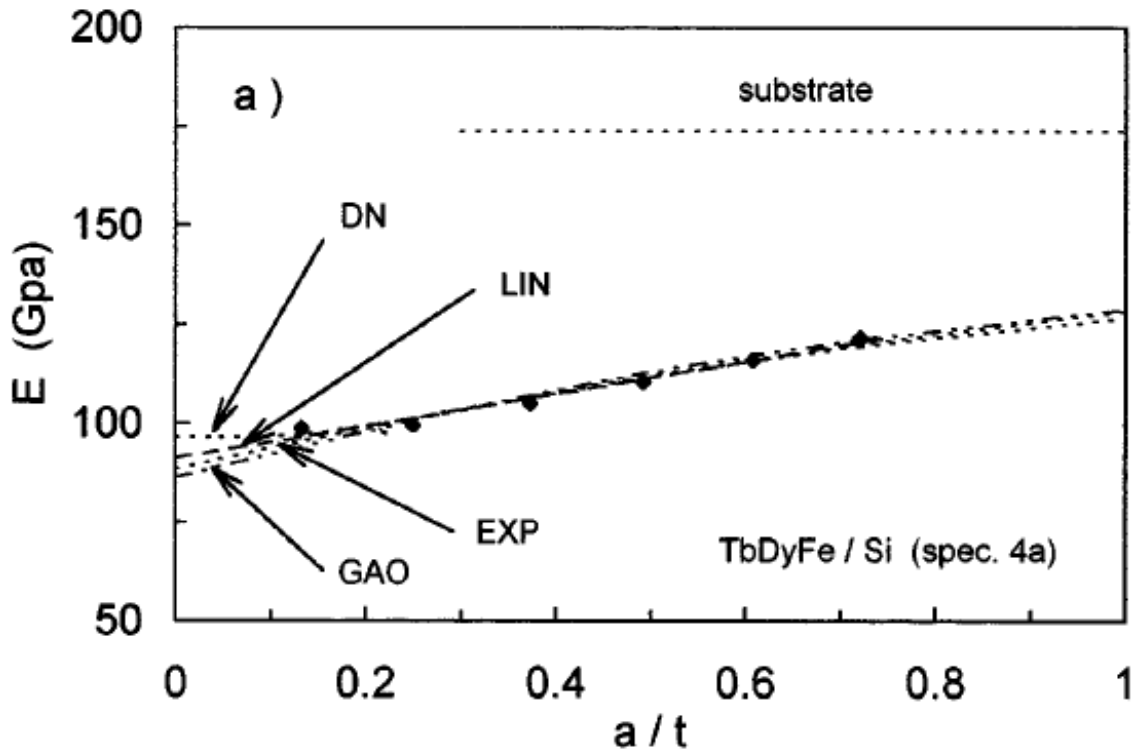


Figure 2.17a Experimental data and the regression values for the TbDyFe/Si film on Si.

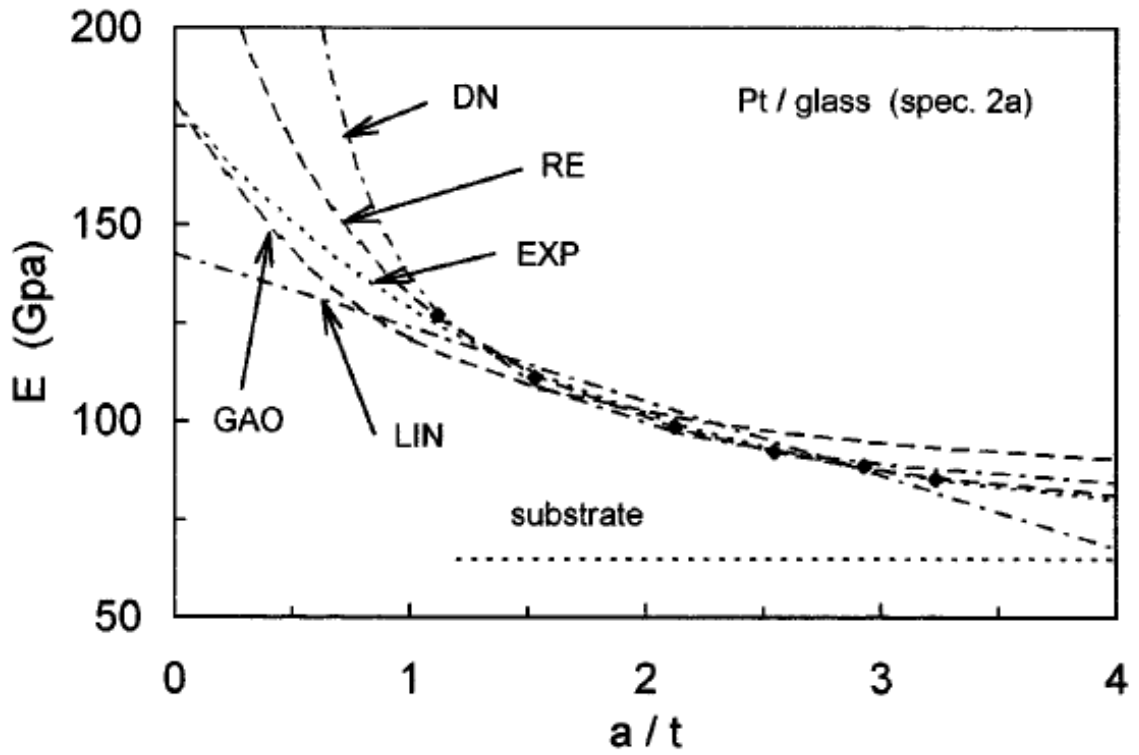


Figure 2.17b Experimental data and the regression values for the Pt film on glass.

2.4 Finite element analysis of thin film nanoindentation

Finite element analysis is another promising technique for investigating thin film nanoindentation [44,46,52,70,72,77,82-89]. On the one hand, it can help understand the indentation process and elastic and plastic deformation growth in the specimen. On the other hand, it can be used to improve the analytical method for extracting mechanical properties from the load-displacement data. There are many types of FEA software that help simplify thin film indentation simulation, which include: ANSYS, ABAQUS, COSMOS, and COVENTOR, etc. The first step of simulating the indentation contact problem is to define a mesh and the element type that can fit the real thin film/substrate and indenter well. It is also important to know the mechanical properties of the indenter, indenter geometry, film thickness, surface contact problem, and tribological properties of the film before any simulation process.

Due to different elements, meshes, dimensions and contact settings, there were numerous successful models built for thin film nanoindentation. Among them, a simple but efficient 2D model has been accepted and used by Bolshakov, Knapp, Gan and many other researchers [46,72,82,84,89]. In this model, the specimen and the indenter are described by a two-dimensional axisymmetric mesh. As shown in figure 2.18 from Knapp's work [72], the element size is not evenly distributed. Note that the element size of the film underneath the indenter is the smallest. Since large deformation is expected in this local area, a small size of 10-20 nm will be sensitive enough for the accurate calculation. The less interest area usually has a relatively large element size to save total computation time. For special interests like the

substrate effect investigation, local substrate area (right below the indenter) will also be refined to have a very small element size. There are two boundary lines for this model. The bottom line is fixed on both lateral and vertical directions, while the left line was only prohibited for lateral movement. The target contact pair consists of the film surface and one edge of the indenter. A detailed setup will be covered in the next chapter. This model is simple but still can provide reasonable results. Besides, due to the small mesh size, it provides a relative short run time, which makes it a useful tool for a large amount simulation work. FEA of thin film indentation has many advantages that the experiments can not provide. It can give us a physical idea about how the film and substrate deform and the elastic and plastic strain growth in the specimen. It can also calculate some properties which are difficult to be obtained from experimental methods, such as residual stress and yield strength. FEA also help to understand the nanoindentation process on very hard thin films. It was found in certain film materials, such as hard DLC or diamond on a soft substrate, the modulus could never reach the suggested values of film modulus (assuming the film modulus is comparable with the bulk value), as shown in figure 2.19. Above all, the encouraging results confirm that FEA is a promising and really helpful tool for the study of thin film nanoindentation.

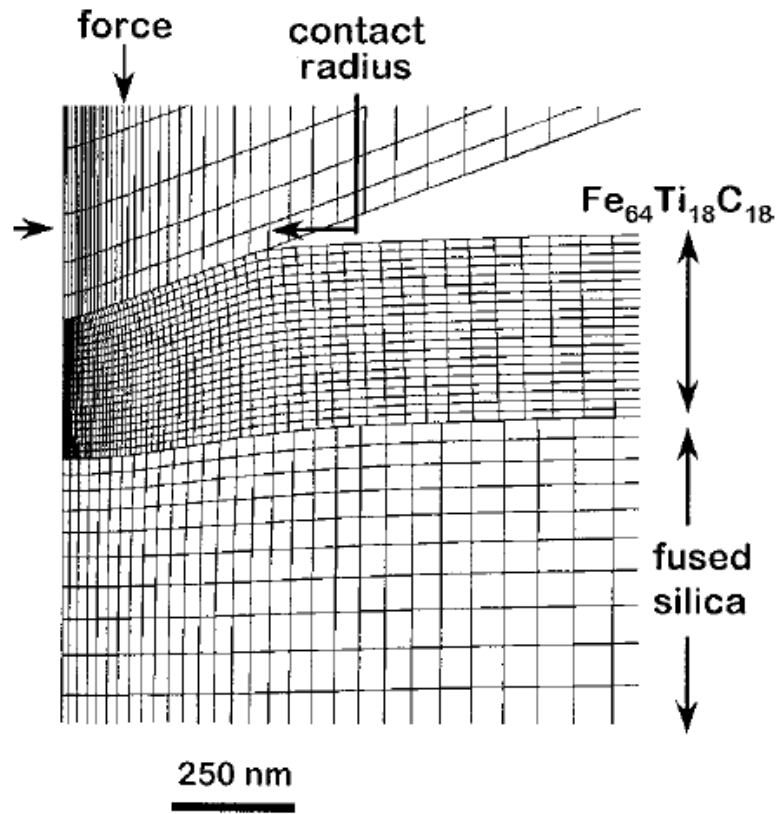


Figure 2.18 Center of a typical 2D axisymmetric mesh for thin film indentation [72]

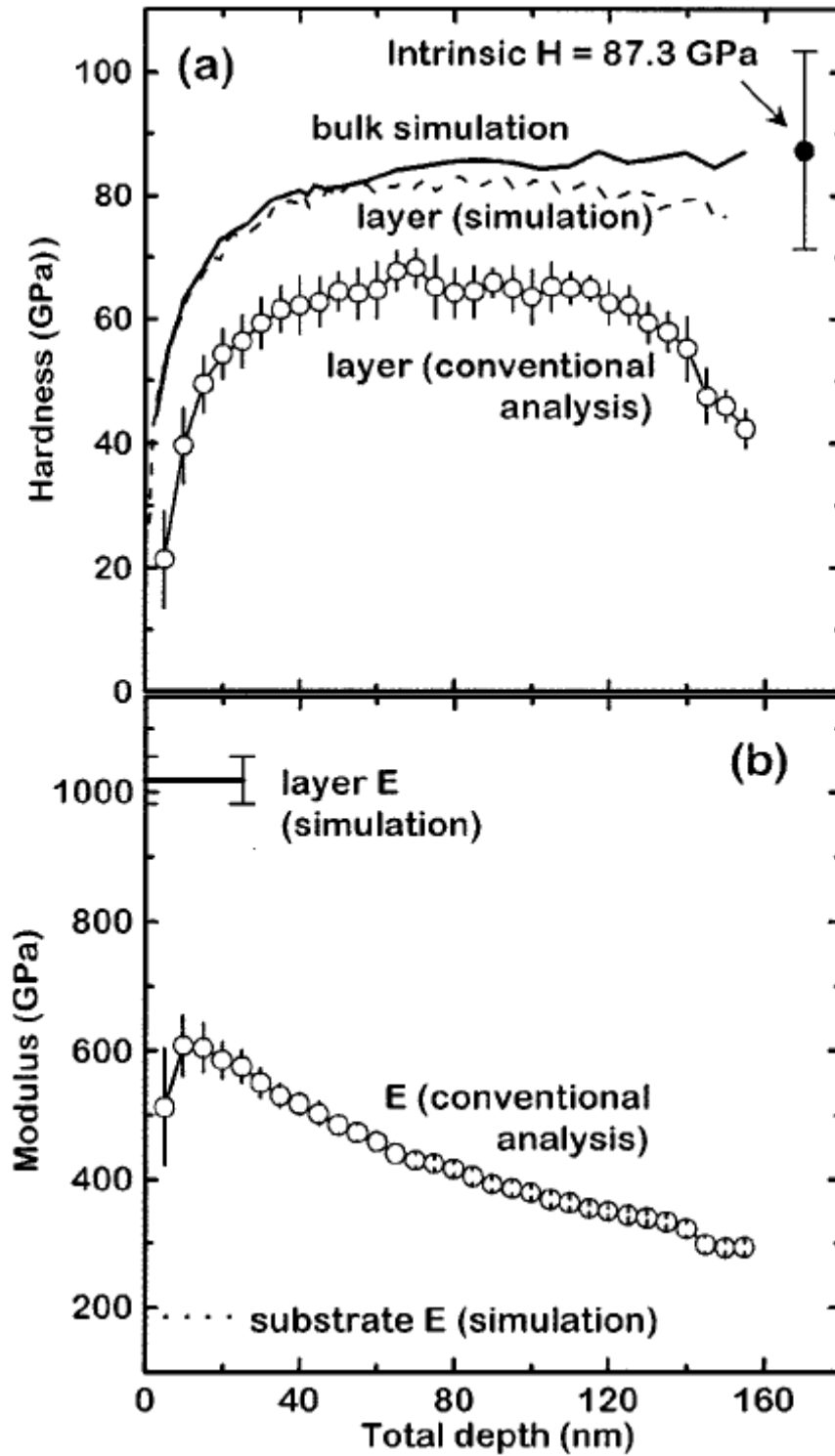


Figure 2.19 (a) Experimental and FEA Hardness vs. displacement curves of a-tC film on Si; (b) Experimental and FEA elastic Modulus vs. displacement curves of a-tC film on Si;

2.5 Pile-up and Sink-in effects

Indentation contact area is a key parameter for thin film modulus and hardness determination. In the Oliver & Pharr method (first suggested in 1992), the contact area was suggested to be a function of the contact depth (h_c), which is related to the indenter geometry. Also in their method, “sink-in” was assumed for all kinds of material (figure 2.6). This assumption seems reasonable as the indenter is pushed into the film, the local area around the tip should also go down to a certain degree. However, when a sharp tip like the Berkovich or Cone is used, the indentation process is both elastic and plastic. In certain materials, the film material around the tip is uplifting plastically instead of normal sink-in, and it can not be explained by the elastic contact theory alone. This plastic phenomenon is called Pile-up. Images of pile-up and sink-in are shown in figure 2.20a [29].

Pile-up doesn't happen in all materials, however, when it does, it will greatly affect determination of film mechanical properties. As shown figure 2.20b [67], the contact depth for pile-up materials is larger than those with sink-in. Thus, if employing the Oliver & Pharr method for sink-in, the contact area of piling up materials will be underestimated, which cause overestimation of the Young's modulus and hardness. Investigations of the pile up mechanism have been performed by many researchers [51,60,67,68,85,90-93]. Bolshakov and Pharr examined pile-up/sink-in in finite element analysis [67]. Based on their results, the hardness can be overestimated up to 60% when pile-up degree is large, while Young's modulus is going to be 30% large. They also examined materials that intended to have pile-up by FEA. It was

found that sink-in usually occurred in materials with low yield stress/Young's modulus ratio and little work-hardening ability, i.e, hard ceramics. On the contrary, pile-up prevails in soft metals. It was also found that the film/substrate modulus ratio played a role for the occurrence of sink-in and pile-up. Normally, pile-up can be found as a very soft film is deposited on a hard substrate, while sink-in happens when a very hard film on a soft substrate.



Figure 2.20a Sink-in and Pile-up profiles during nanoindentation [29]

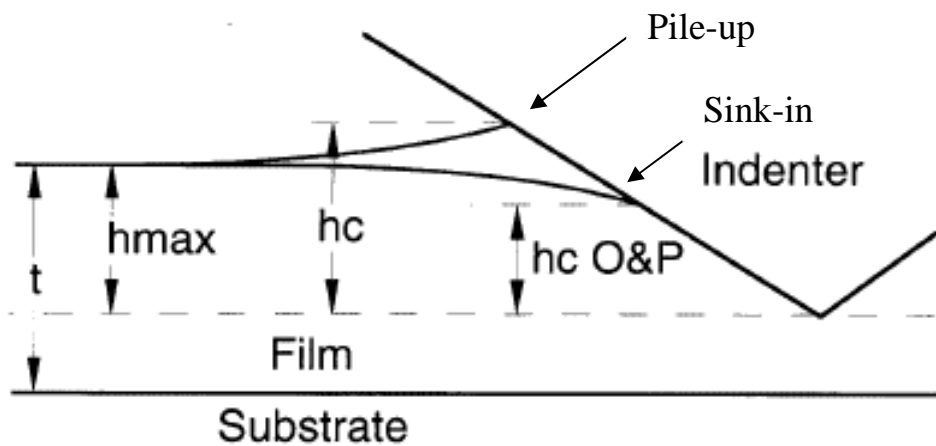


Figure 2.20b Comparison of the contact depths for sink-in and pile-up [67]

The Nix group also put effort in investigating the pile-up mechanism [34,39,68]. In McElhaney and Nix's paper, they presented that the hardness impression on the film after indentation might give the information of how to calculate the pile-up and sink-in contact areas. As shown in figure 2.21 from Scanning Electron Microscopy (SEM) [29], the impression from a pile-up has a convex shape, and sink-in usually has a concave impression. A clear schematic is illustrated in figure 2.22 [68]. Due to the unique relation between the impression and the cross-section area of the indenter, the contact area can be estimated if the pile-up degree is known. In recent years, as the Atomic Force Microscope (AFM) has been introduced for thin film surface characterizations, the pile up degree can be easily determined through an AFM scan across the indentation impression as shown in figure 2.23 and 2.24.

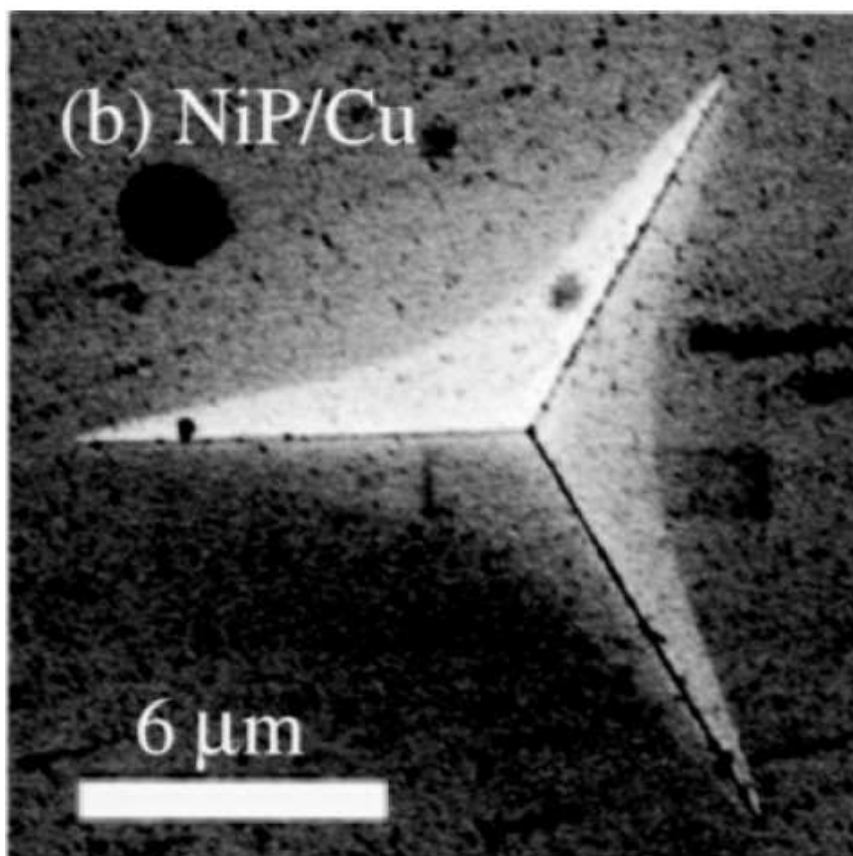
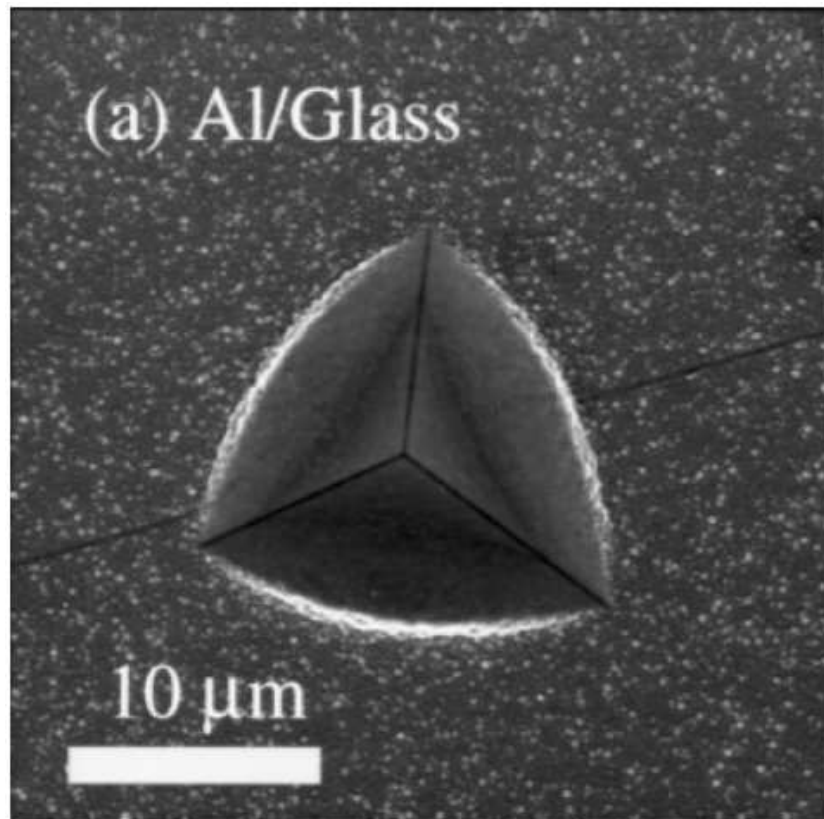


Figure 2.21 (a) SEM image of a pileup indentation impression on Al/Glass; (b) SEM image of a sink-in indentation impression on NiP/Cu [29]

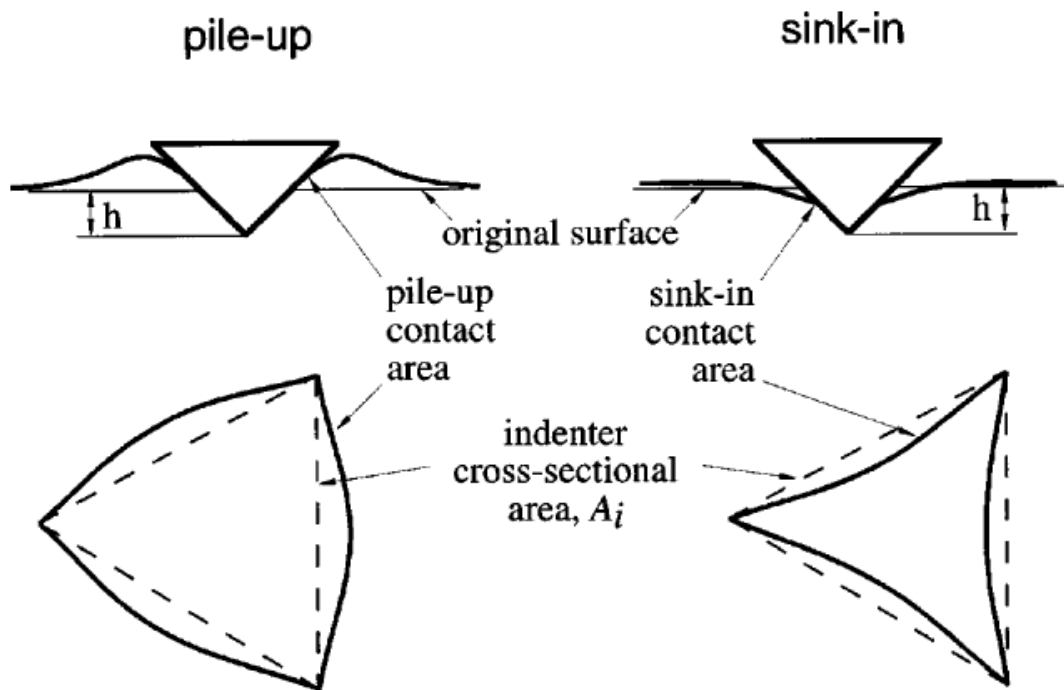


Figure 2.22 Schematic of Pile-up and sink-in contact areas during indentation [68]

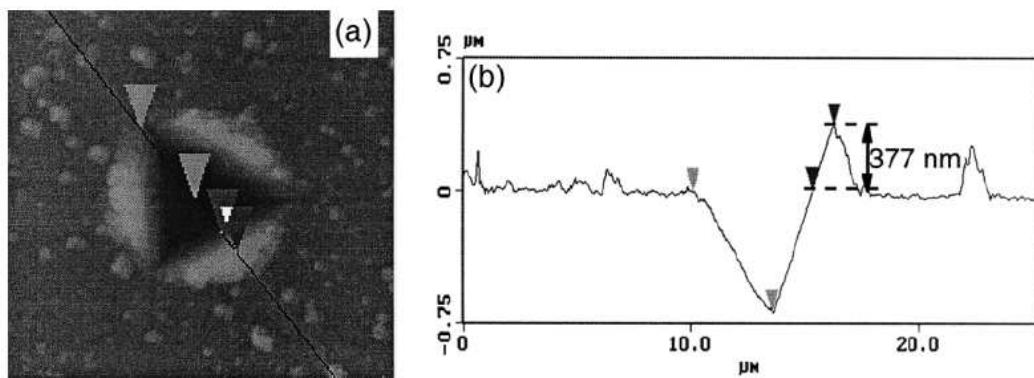


Figure 2.23 AFM (a) image and (b) profile of a 750 indentation on Al/Glass [39]

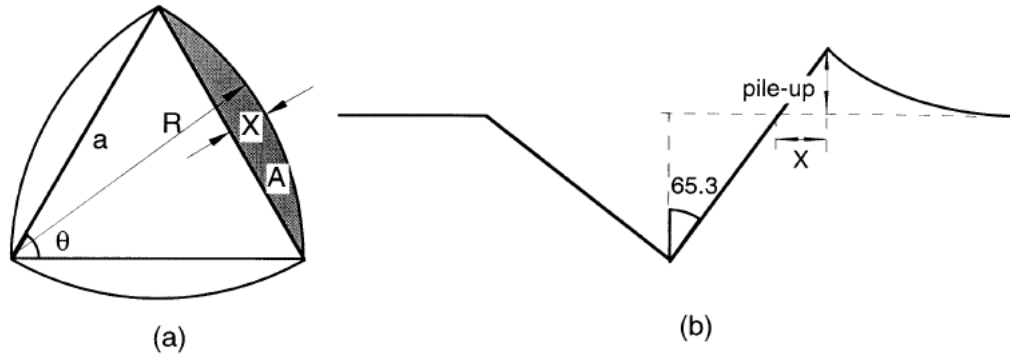


Figure 2.24 Schematic representation of (a) the projected contact area due to pile-up. (b) Cross-section of the contact area again showing pile-up [34]

However, it is still difficult to build up a relation between the pile-up/sink-in degrees with film/substrate mechanical properties. The Nix group developed a method to eliminate. Joslin and Oliver first suggested to use load over stiffness square (P/S^2) parameter to eliminate the pile-up and sink-in effects [94]. As shown in Eq. 16 and figure 2.25, P/S^2 is independent of the contact area, and thus is not corrupted by pile-up/sink-in. Later on, the Nix group used this parameter to investigate the indentation size effects on hardness [34]. They chose those films and substrates with similar Young's modulus (i.e. Al on glass) to eliminate the substrate effects. However, for the film and substrate with different values, E_r in Eq. 16 is affected by the substrate effects.

$$\frac{P}{S^2} = \frac{1}{\beta} \frac{\pi H}{4 E_r^2} \quad (16)$$

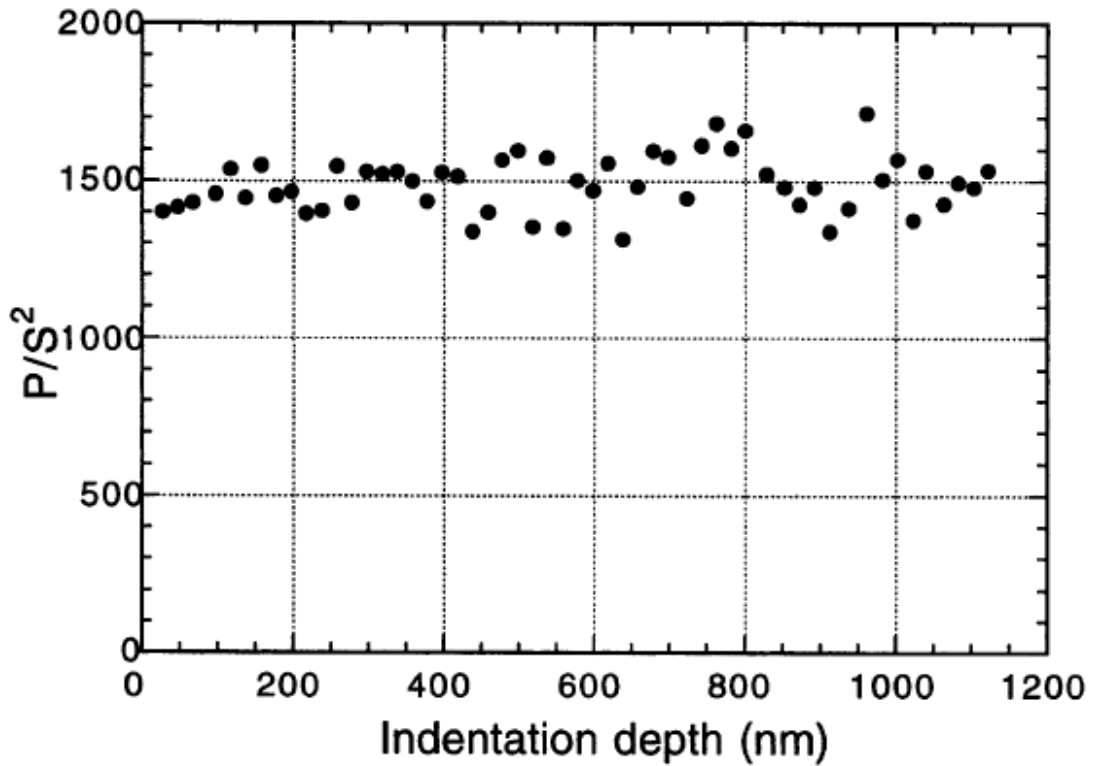


Figure 2.25 Load over stiffness square (P/S^2) vs. indentation depth for fused silica film on Si substrate [34]

Compared to the plastic pile-up, sink-in degree is more difficult to determine accurately because it involves elastic contact problem. Some serious sink-in situation (larger than that the Oliver & Pharr method expects) might occur when indenting on very hard materials like diamond. Serious sink-in will usually cause overestimation of the contact and resulting to a smaller modulus and hard value. Finite element analysis is often used to examine this situation, as shown in figure 2.19 [72].

2.6 Thin film microstructure effects (size effects)

As thin films dimensions begin to approach that of the film microstructural features, the materials mechanical properties begin to exhibit a dependence on the specimen size [32,45,60,61,69,95,96]. In other words, as film thickness reduces to the micro scale, those data obtained from bulk materials are no longer suitable for thin film mechanical properties. Usually, plastic behavior, fracture strength and fatigue resistance will have the size effects when film thickness reduces to micron scale or smaller, while the elastic properties, which depend on the material bonding structure, will not exhibit the size effects until the nanoscale. Figure 2.26 [50] shows the schematic of length-scale effects on the mechanical properties. Moreover, as the film sizes reduce, the micro/nano-structures like grain or cluster size will change, which has an effect on both the elastic plastic behavior.

The thin film microstructures largely complicate the analysis of nanoindentation data as they are often textured and do not represent a continuum. For instance, the anisotropic elastic properties due to the different crystal orientations, the strain gradient due to the crystalline structure, and the grain sizes and boundaries will cause the nanoindentation load-displacement to be shifted from the theoretical prediction [60,95]. To better understand the substrate effects and the basic thin film elastic strain growth mechanism, one should eliminate the microstructures factors to a minimum degree. The amorphous materials are qualified for this study, since they have no grain structures and are typically elastically isotropic.

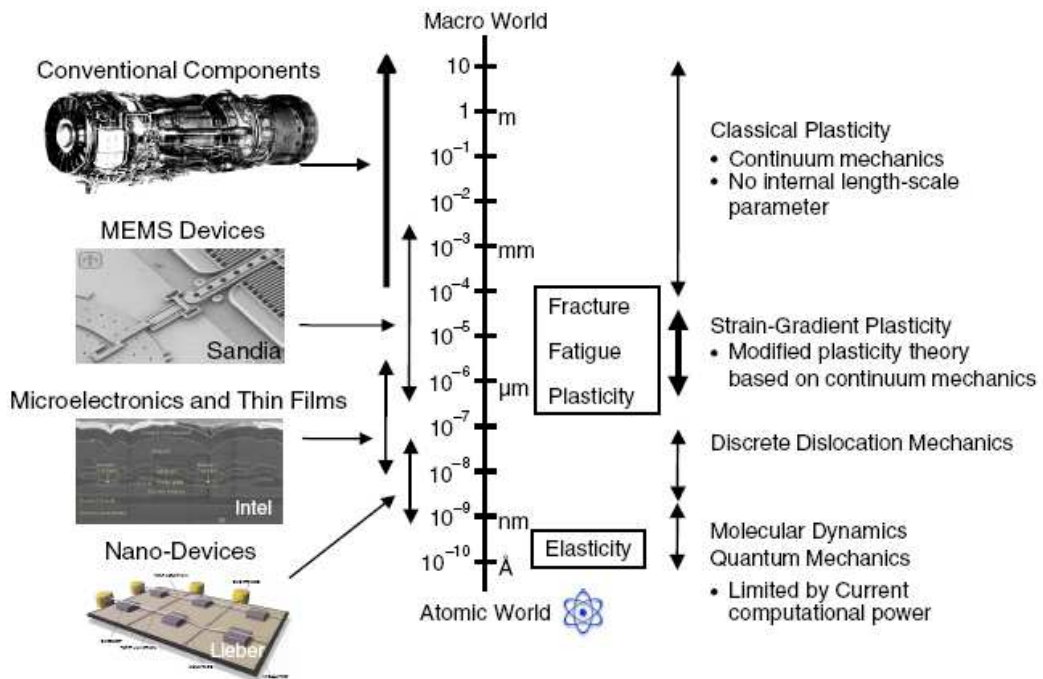


Figure 2.25 Illustration of length-scale effects on the mechanical properties of materials [50]

2.7 Thin film deposition mechanism

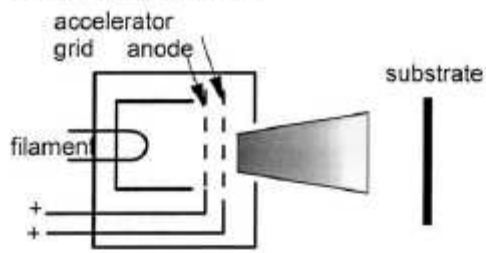
There are numerous ways to deposit or grow a thin film on a substrate. It includes: sputtering, e-beam evaporation, plasma enhanced chemical vapor deposition (PECVD), low pressure chemical vapor deposition (LPCVD), microwave plasma chemical vapor deposition (MPCVD), Oxide growth, layer by layer (LBL), Ion beam, mass selected ion beam (MSIB), cathodic arc, pulsed laser deposition (PLD). Figure 2.26 shows the schematics of selected deposition systems for thin films [97]. Among those methods, sputtering and CVD methods are most frequently used for industrial process and laboratory studies, respectively. Sputtering is a physical process (except reactive sputtering), where ion bombardment is the key mechanism for thin film

growth. Either DC or RF power could be used to generate argon plasma sputtering the graphite electrode. Magnetic fields are often applied in the sputtering chamber to increase the deposition rate. The magnetic fields make the electrons spiral and increase their mean free path. In other words, it increases the ionization degree of the plasma. A bias voltage is often applied to the substrate to increase the ion bombardment. Sputtering has several advantages, such as versatility of sputtering methods and deposition conditions can be easily controlled by the plasma power and gas pressure. For sputtering amorphous films, a high chamber pressure (achieved by large gas flow) is needed to reduce the ion mean free path so that the bombard energy is not great enough to create crystal structure. A relatively low sputtering power can also help create amorphous structure.

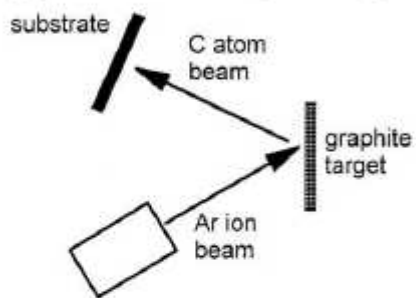
Compared to sputtering, CVD methods involve not only the physical process of bombardment but also the chemical reactions on and inside the films. Among them, PECVD is a decent process that is often used in semiconductor manufacturing to deposit films onto wafers containing metal layers or other temperature-sensitive structures. A simple schematic of RF PECVD is shown in figure 2.27. Using LPCVD can increase the uniformity of the thin films, and MPCVD is often employed to grow very hard materials. During a CVD process, as the source gases are induced into the main chamber, the plasma is created between electrodes by the RF or DC power. One important feature, the “plasma sheath” [98] is formed near the electrode surface due to the different mobility between ions and electrons. Since electrons have much higher thermal velocities than ions, they are lost faster at the electrodes and leave the plasma

slightly positive charged. Thus an electric field is generated pointed from plasma to the solid surface and accelerates the ions in the plasma to the wall. This confines the ions near the surface and creates a sheath with a net positive charge. The sheath has an order of Debye length in thickness and usually is darker due to the low electron density in that region. In low pressure, the ion sheaths formed are collisionless and have low conductivity thus serving as diodes between plasma and electrodes. The electrodes then obtain DC self-bias voltages equal to their peak RF voltage. Thus, the inverse capacitances of these two diodes determine the DC bias direction. The shorter electrode has a smaller capacitance, which brings a larger (negative) bias voltage. Thus the DC bias is point from the larger electrode to the shorter one. The field accelerates the positive ions to the shorter electrode. This is the reason that substrate is mounted to the shorter electrode.

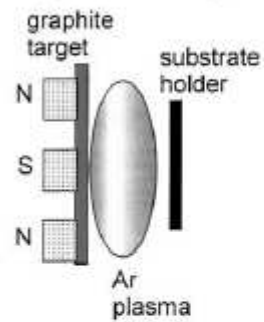
(a) Ion deposition



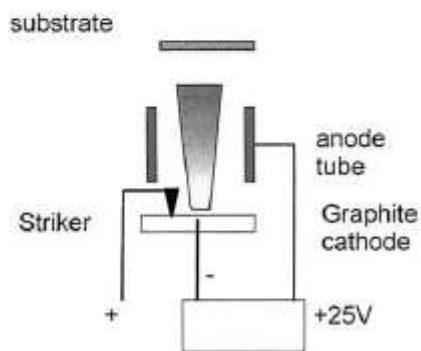
(b) Ion assisted sputtering



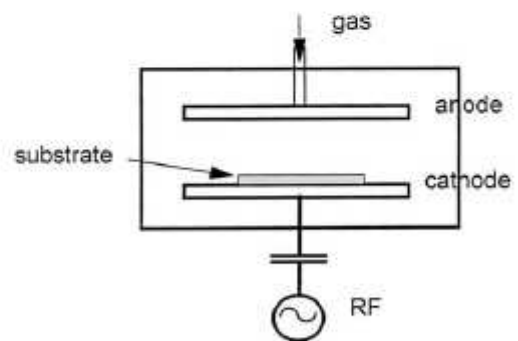
(c) Sputtering



(d) Cathodic Vacuum Arc



(e) Plasma deposition



(f) Pulsed laser deposition

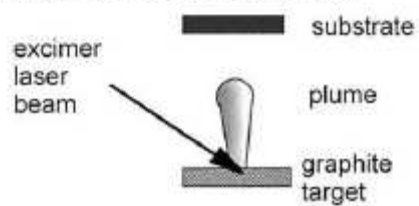


Figure 2.26 Various deposition systems for thin films [97]

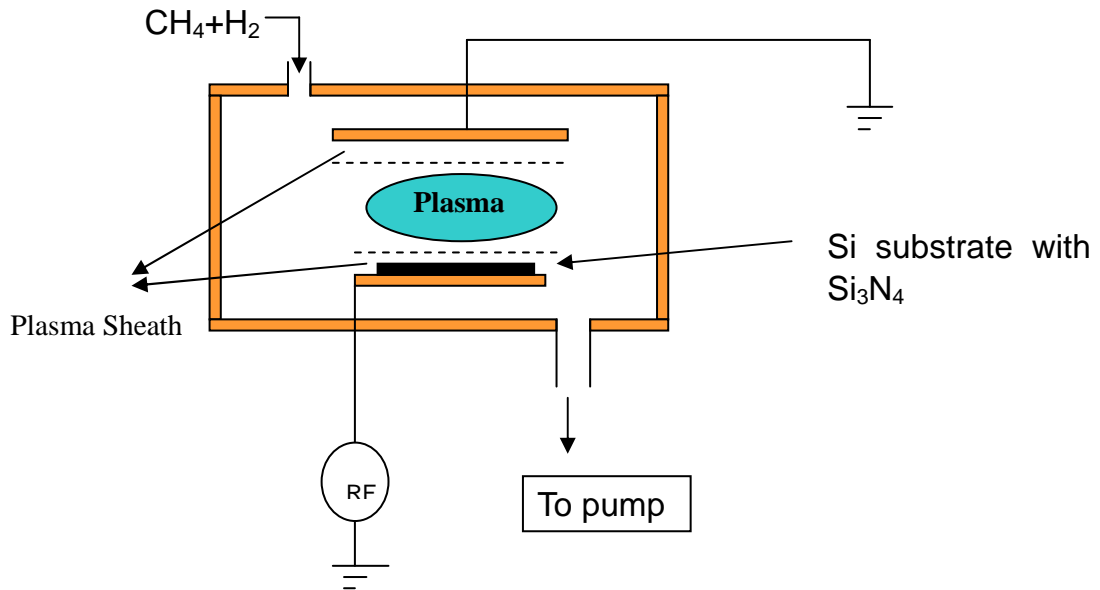


Figure 2.27 Schematic of RF PECVD and plasma sheath

2.8 X-ray diffraction technique

X-ray diffraction is a very useful experimental technique for structural analysis of crystals. It can also be used to determine whether the material is amorphous or not. X-ray is one kind of electromagnetic wave, whose wavelength (0.01~10nm) is very close to the period of crystal lattices and the spacing of atoms in crystals. When x-rays pass through a crystal, they will be diffracted by the crystal planes. By scanning the X-ray through the specimen, peaks represent the crystal planes will show up in the X-ray spectrum, so that the crystal structure information can be obtained. Applying XRD on thin film system is different from testing the bulk materials. As the x-ray will penetrate a few microns into the material, the X-ray spectrum usually contains the crystal structures information for both the film and the substrate. To obtain the film x-ray spectrum, another scan is performed on bulk substrate materials. Subtracting the latter from the composite X-ray spectrum leads to data of the film crystal structure.

Amorphous film structure determination is relatively easy to achieve through XRD. The amorphous X-ray spectrum should not contain any peaks of the crystal planes. As long as the composite and bulk substrate data overlap each other, the film is amorphous. Refer to Cullity's book "Elements of X-ray Diffraction" for detailed information [99].

CHAPTER 3

EXPERIMENTAL SETUP

3.1 Thin film selection and deposition

The materials selected for this research covered a wide range of the Young's modulus values. From soft to hard, the amorphous films were made of polymer, near-frictionless carbon (NFC), chromium oxide (CrO_x), silicon dioxide (SiO_2), iron oxide (FeO_x), titanium oxide (TiO_x), amorphous Si (a-Si), aluminum oxide (AlO_x), aluminum nitride (AlN), iron boron (FeB), nickel titanium (NiTi), METGLAS, silicon nitride (Si_3N_4), silicon carbide (SiC), and tetrahedral hydrogenated carbon (ta-C:H). As it was difficult to get a very hard amorphous diamond-like film, ultra nano-crystalline diamond was employed in this study. Bulk silicon was used as the substrate materials, all of which were p-type $\langle 100 \rangle$ direction wafers. The substrate thickness was $500\mu\text{m} \pm 15\mu\text{m}$.

Thin films were deposited using various techniques. The film thickness, deposition methods and target materials/source gases are listed in table 3.1. Metals oxides like CrO_x , FeO_x , TiO_x , and AlO_x were deposited using the sputtering system. Important sputtering parameters are listed in table 3.2. Note that the sputtering power and gas flows vary with materials. The best parameters for amorphous films growth were experimentally determined by depositing films with different combinations of parameters (i.e. fix the power value then change the gas flow ratio, and fix gas ratio to

change the power). Based on the characterization results, the parameters that generated the “most” amorphous (no peaks in XRD, small cluster size, and smooth surface, etc) film were selected. The image of a sputtering system is shown in figure 3.1.

The NFC and ta-C:H films were grown using the RF PECVD method at Argonne National Lab [45]. The near-frictionless carbon films possess unique mechanical and tribological properties that have exhibited the lowest ever recorded friction coefficient, 0.001, and ultra-low wear rates of 10^{-11} – 10^{-10} mm³ N⁻¹ m⁻¹, even under dry sliding conditions and at very high contact pressures [57,62,73,79,80,100-106]. Tetrahedral hydrogenated carbon (ta-C:H) is one kind diamond-like carbon materials that possess relatively high Young’s modulus and hardness. Figure 3.2a and 3.2b show a schematic of a PECVD system and an image of the CVD chamber, respectively. In PECVD mode, the flow rate of the precursor gases was limited to a maximum of 60 sccm. All substrates were pre-sputtered with Argon plasma using RF powers between 900-1100W for cleaning purpose. The pre-sputtering time ranged from 5 to 15 minutes depending on the process requirement. The base pressure prior to deposition was 3×10^{-7} torr, while the deposition pressure was 20-24 mtorr. The self bias voltage applied was -375V~-425V. This bias was higher than the voltage (-100V) mentioned in literature review that gives the highest Young’s modulus and density. Actually, different experimental conditions like gas flow rates, sources gas ratio, RF field-plate (FP) power and the chamber volume will cause this bias voltage changing.

The source gases for NFC and ta-C:H deposition were methane (CH_4) and hydrogen (H_2). The different ratio between these two gases brings different properties (structure) of the films. For NFC films, the ratio was 75% hydrogen (42 sccm flow rate) and 25% methane (14 sccm flow rate). A much higher methane ratio was used for ta-C:H deposition to increase the film strength [107]. The total flow rate should not be over 60 sccm during the whole deposition process. The process was running at Room Temperature. The estimated deposition rate was around 1.85nm/min, so it took about 9 hours to grow a $1\mu\text{m}$ NFC or ta-C:H film. The NFC films with different thicknesses were deposited for the experiments.

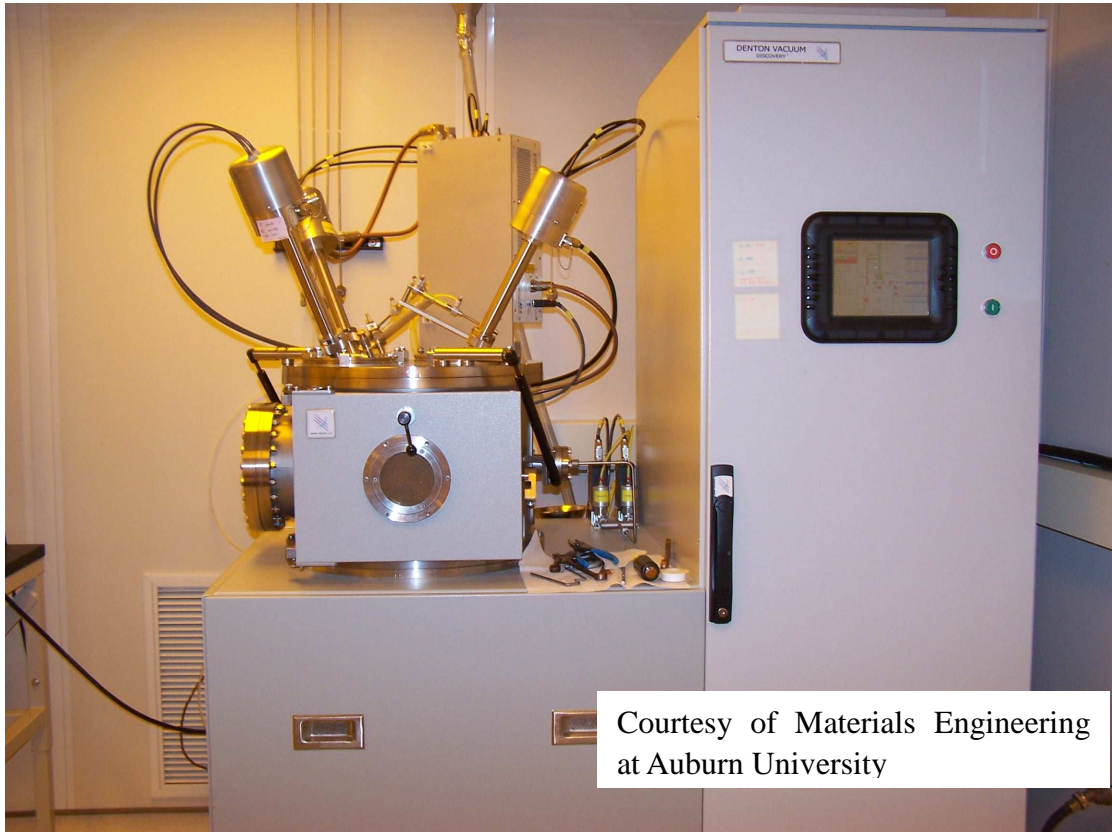
Dielectric films like SiO_2 and Si_3N_4 were deposited using LPCVD method. A low pressure CVD can help grow smooth and uniform amorphous films. For Si_3N_4 , the source gases were dichloro-Silane (SiH_2Cl_2 , 140sccm) and Ammonia (NH_3 , 30sccm). The deposition temperature was $850\text{ }^\circ\text{C}$ and the pressure was around 420 mtorr. It took 90 min to deposit 300nm silicon nitride on both sides of the wafer. SiO_2 were also deposited using this method with the source gases of silane and oxygen. Detailed information can be found in Jaeger's book "Introduction to microelectronic fabrication" [108]. The UNCD film was deposited through MPCVD [75], and the polymer film was grown using a typical layer-by-layer method [109].

Table 3.1 Deposition information for all the specimens

Thin Films	Deposition Method	Target materials & Source Gases	Film Thickness (nm)
Polymer	LBL	Polymer	225
NFC	PECVD	CH ₄ +H ₂	150, 380, 1125
CrO _x	Sputtering	Cr+O ₂	125, 2000
SiO ₂	LPCVD	SiH ₄ +O ₂	395
FeO _x	Sputtering	Fe+O ₂	125
TiO _x	Sputtering	Ti+O ₂	120
a-Si	Sputtering	Si	450
AlO _x	Sputtering	Al+O ₂	120
AlN	Sputtering	Al+N ₂	1100
FeB	Sputtering	Fe+B	1010
Metglas	Sputtering	METGLAS	278
Si ₃ N ₄	LPCVD	Si+SiH ₂ Cl ₂ +NH ₃	300
SiC	Sputtering	SiC	500
a-C:H	PECVD	C ₂ H ₂ +H ₂	868
UNCD	MPCVD	CH ₄ +H ₂	560

Table 3.2 Selected sputtering parameters for amorphous CrO_x

Sputtering Power	DC
Target	Chromium
Substrate	Silicon
Base Pressure	6x10 ⁻⁶ torr
Pre-sputtering Time	120 sec
Pre-sputtering power	150 watts
Sputtering Time	600 sec
Sputtering Power	150 w
Gas 1 flow (Ar)	27 sccm
Gas 1 flow (O₂)	13 sccm
Deposition Temperature	Room Temperature
Substrate Holder Rotate	50%
Ignition Pressure	70 mtorr
Deposition Pressure	7.8~8.0 mtorr



Courtesy of Materials Engineering
at Auburn University

Figure 3.1 Image of a Denton sputtering system

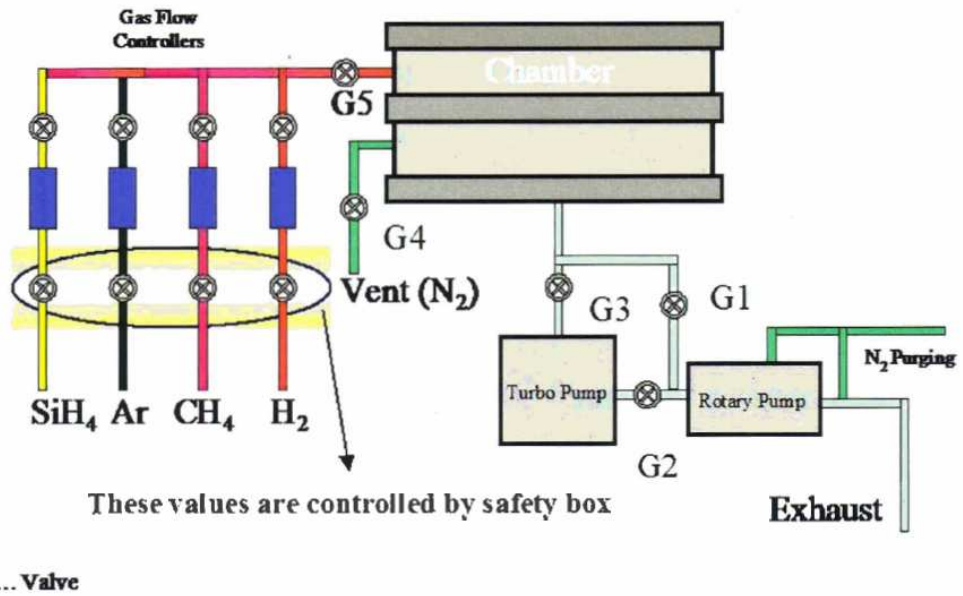


Figure 3.2a Schematic of the RF PECVD system at Argonne National Lab

Courtesy of Argonne National Lab

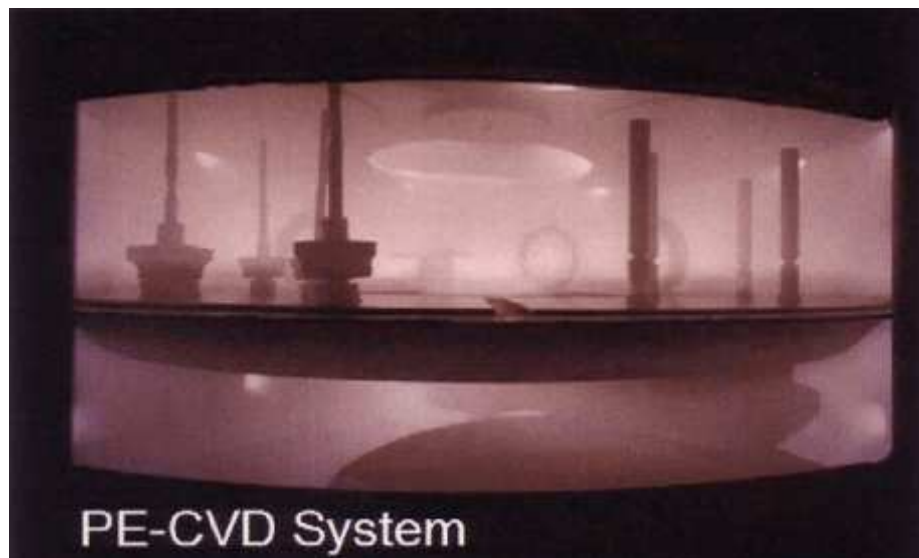


Figure 3.2b Image of the PECVD chamber at Argonne National Lab

Courtesy of Argonne National Lab

3.2 Thin film Characterizations

The deposited films were tested with XRD for confirming the amorphous structure. SEM and AFM characterizations were employed to observe the surface conditions of the films.

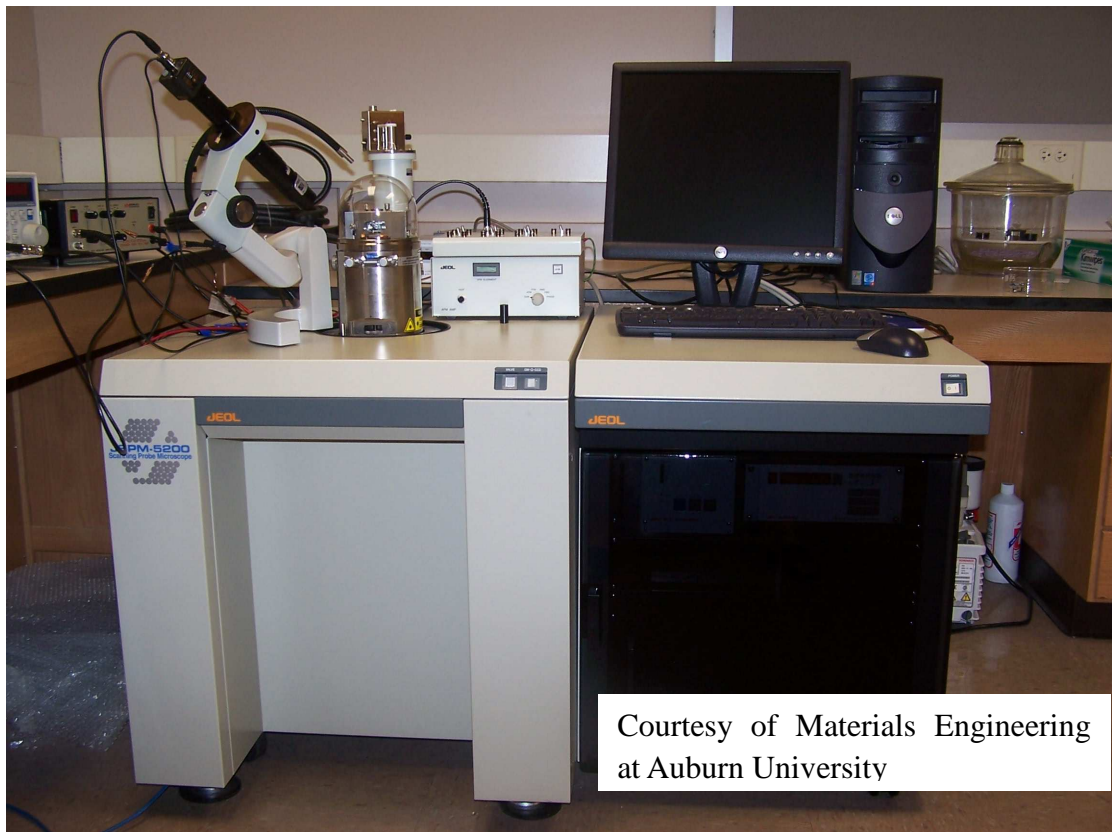


Figure 3.3 Image of a Jeol 5000 atomic force microscope

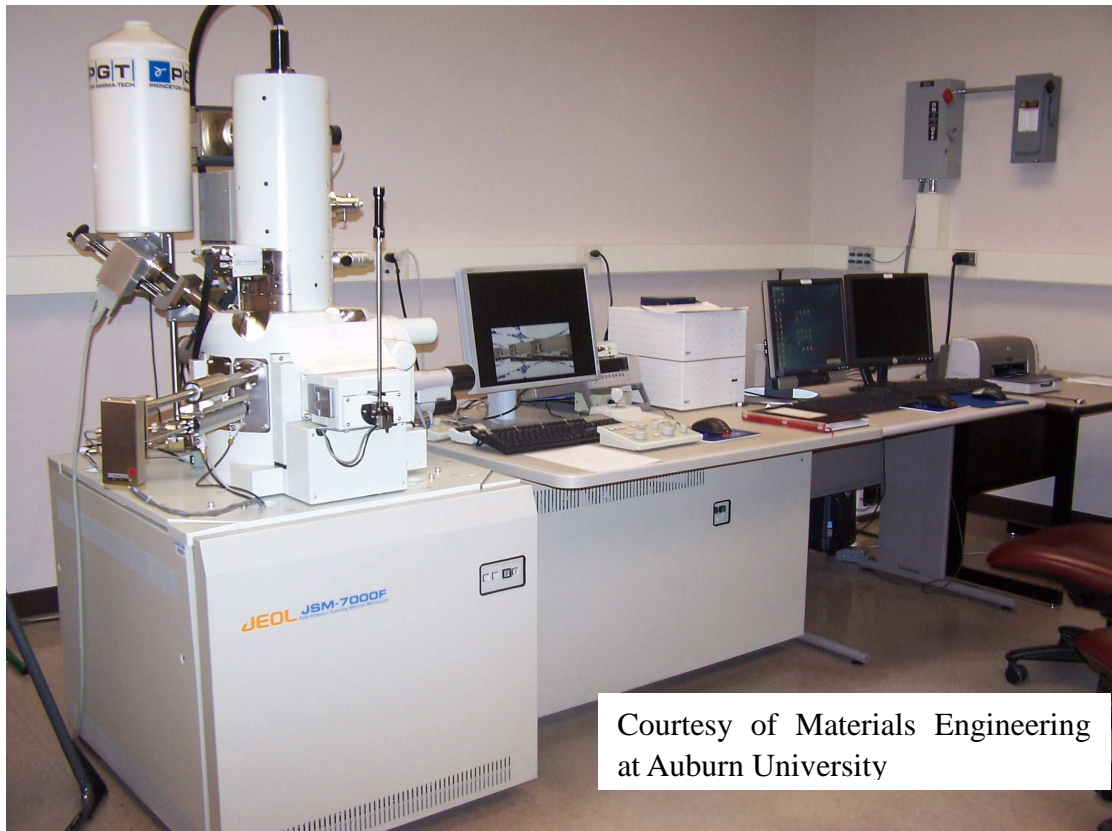


Figure 3.4 Image of a Jeol 7000F field emission scanning electron microscope

3.3 Nanoindentation Setup

The indentation tests were performed with an MTS Nanoindenter XP system at ambient pressure and temperature (Figure 2.1b). The Nanoindenter tip was a Berkovich type diamond pyramid. For the CSM (dynamic) method, the allowable thermal drift rate was limited as 0.05 nm/s. The Poisson's ratio of the film was assumed as equal to that of the same bulk material. The Poisson's ratio of the substrate was set as 0.28 for $\langle 100 \rangle$ silicon [110]. The continuous stiffness measurement was depth-controlled and the harmonic displacement target was set to 2 nm. For each thin film, 20 or more CSM tests were run with same final indent depth. Film Young's modulus was determined from the load-displacement curve and the

CSM modulus-displacement curve. The contact depth (h_c) and the projected contact area (A) were calculated independently using Eq. (10) and (11) in Chapter 2.

3.4 Finite Element Analysis Setup

The FEM was performed using ANSYS 11.0. The model was built-up using 2-D elements. To simplify the simulation, two assumptions have been made beforehand: the film surface roughness and residual stress were ignored during simulations. Following are the detailed procedures of setting up the parameters in ANSYS:

1. The Preferences setup was Structural.
2. Element type for film, substrate, and tip was PLANE183 (8 node). The target and contact surface elements would be setup later.
3. The real constant for PLANE183 was using default/none. The real constant for the target-contact pair would be setup later.
4. The materials properties were set as linear and elastic isotropic for both the film/substrate and the tip. The tip was designed to only have elastic deformation. The film Young's modulus was defined using the experimental data obtained from nanoindentation. The Si substrate modulus was defined as 170 GPa and the Poisson's ratio was set to $\nu=0.28$ for <100> wafers. The indenter tip's modulus and Poisson's ratio were set to $E=1141$ GPa, $\nu=0.07$.
5. Modeling was used to define the shape of the film, substrate and tip. The thickness of film was designed to match the true value of each thin film. The width was

defined as 10 μm for all the cases. The substrate had the same width with the film, and the thickness was designed as 20 μm . The film and substrate were designed to be perfectly attached to each other. Usually, the film and substrate thickness ratio would be close to 1/20, which was good enough for analyzing the elastic strain grown in the specimen. To simplify the simulation, the tip was designed as a half shape of a Berkovich tip. The right triangle has an angle of 65.3° , which is half of the Berkovich total angle (from one edge to the opposite face). The length of the tip was designed as 1 μm to match the film thickness.

6. The mesh needs to be first defined on the film, substrate, and tip, before defining the target-contact surface. The element size of the film in the local contact area is about 10 nm, where a high stress/strain concentration is expected. The size increases along with the width. But along the thickness, the element size doesn't change as the film is very thin. The substrate and tip meshes are defined with the same manner. The total element number is around 20000~30000. The estimated calculating time is around 5-10 min.
7. The target-contact pair is designed for two surfaces (lines) touching each other. In the pair, element type TARGE169 is designed for the indenter tip edge, and the CONTA172 is designed for the film surface. The real constant for the pair used in this study is the system defaults. Changing the real constant may improve the model in future study.
8. The simulation is quasi-static, and the tip movement is controlled by displacement. . The displacement value for each film matches the experimentally

obtained critical indent depth.

A schematic of the central portion of the mesh design for this FEA study is shown in figure 3.5.

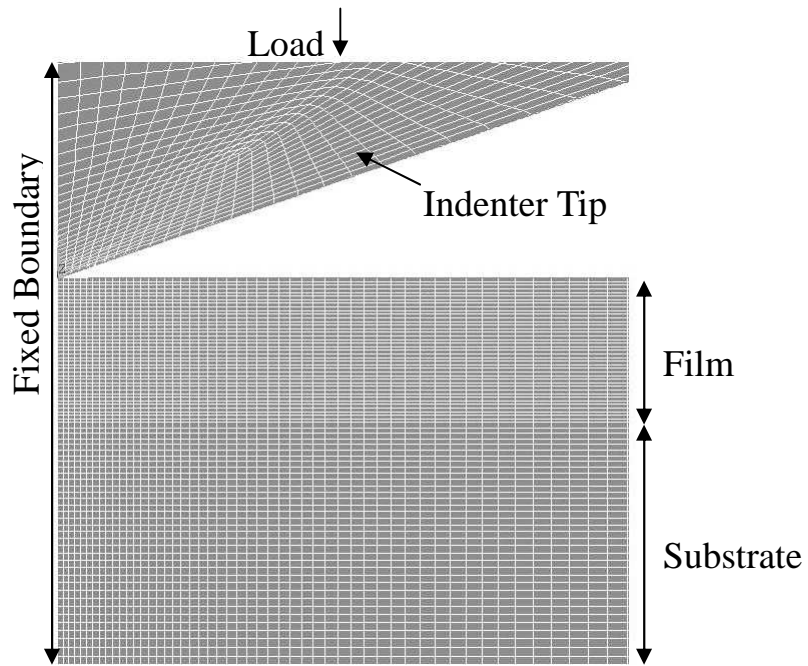


Figure 3.5 Schematic of the finite element analysis of the nanoindentation.

CHAPTER 4

RESULTS AND DISCUSSIONS

4.1 Film thickness measurement & XRD results

Accurate measurement of the thin film thickness was extremely important to this work. As many specimens had thickness less than 200 nm, normal profilometers that were used for micro-scale devices no longer met the requirement. Thus, SEM characterization was employed to determine the thickness. The specimen was cut into pieces after deposition on a silicon wafer. One of them was selected for SEM observation, which should have a flat and clean cross-section. Sometimes, several chips of the specimen from different locations on the wafer needed to be characterized to gain an average value of the film thickness. During SEM tests, the chips were vertically attached to the sample holder so that the cross-section can be focused directly. Figure 4.1a shows a SEM image for the ta-C:H film cross-section. A uniform 885 nm thick layer was observed on the bulk silicon. However, clear boundary between the film and the substrate could not always be found in normal SEM observation. In this case, the SEM composition mode needed to be employed. As shown in figure 4.1b, different materials would have various gray-scale colors in the image, which made it easy to define the film layer. Note that the “compo” sign at the lower left corner of the picture distinguishes it from the regular SEM images. XRD results were shown in figure 4.2. Most of the spectra consist of two major peaks,

which belong to the silicon substrate (002) and (004) planes. There are no obvious peaks that belong to the target films shown in the spectra. The films are amorphous.

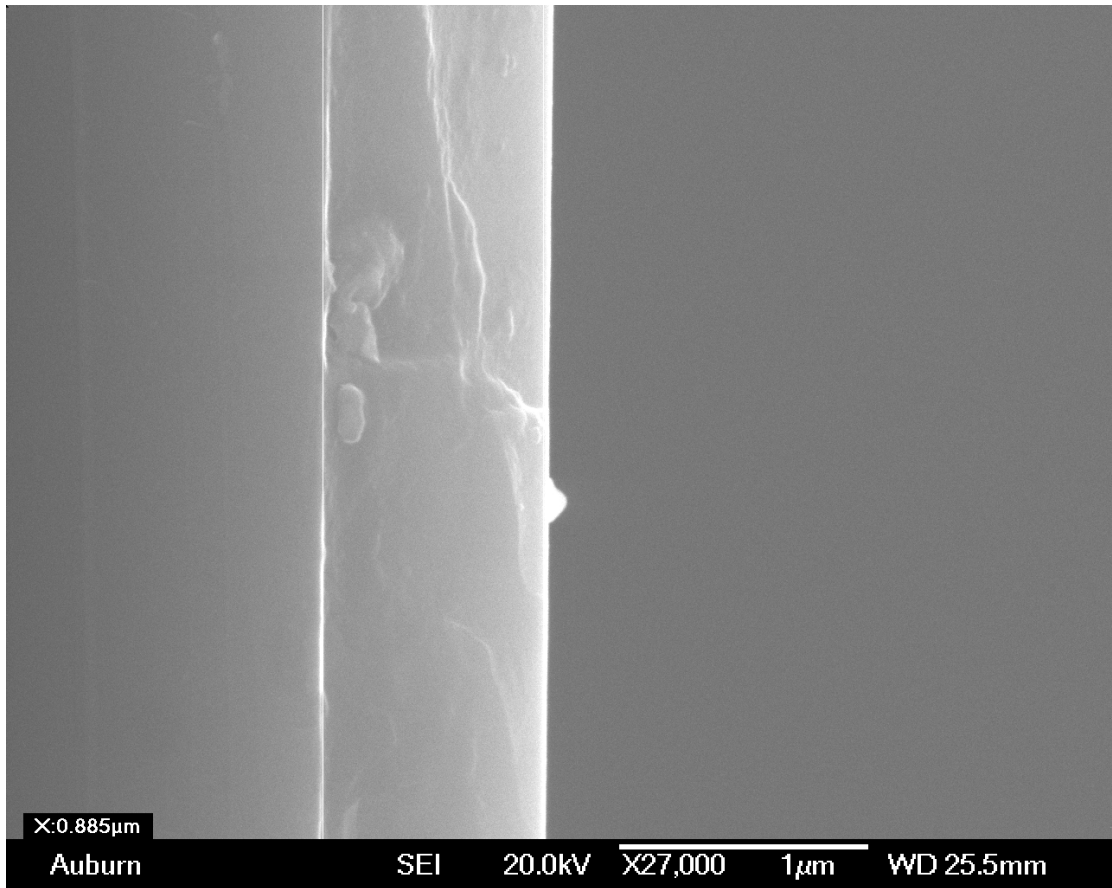


Figure 4.1a Cross-sectional SEM image of ta-C:H film on Si substrate

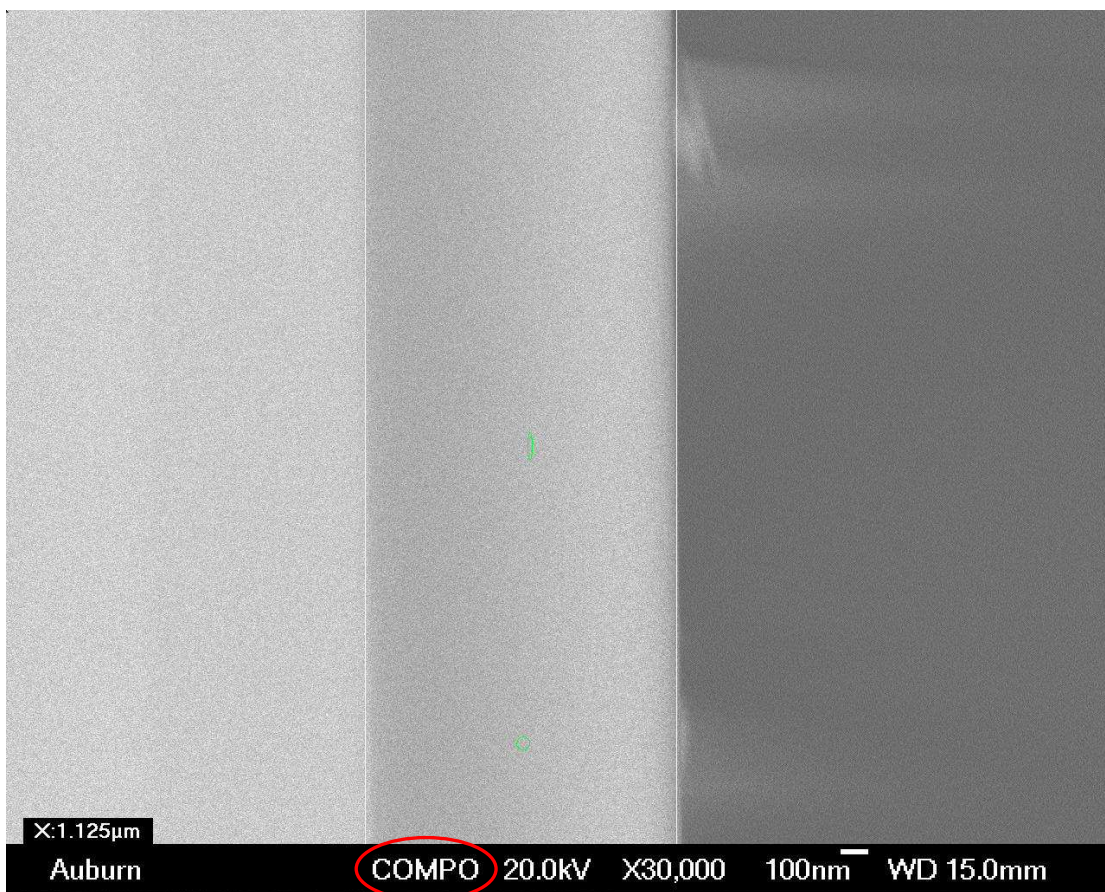


Figure 4.1b Composition SEM image of the cross-section of NFC/Si

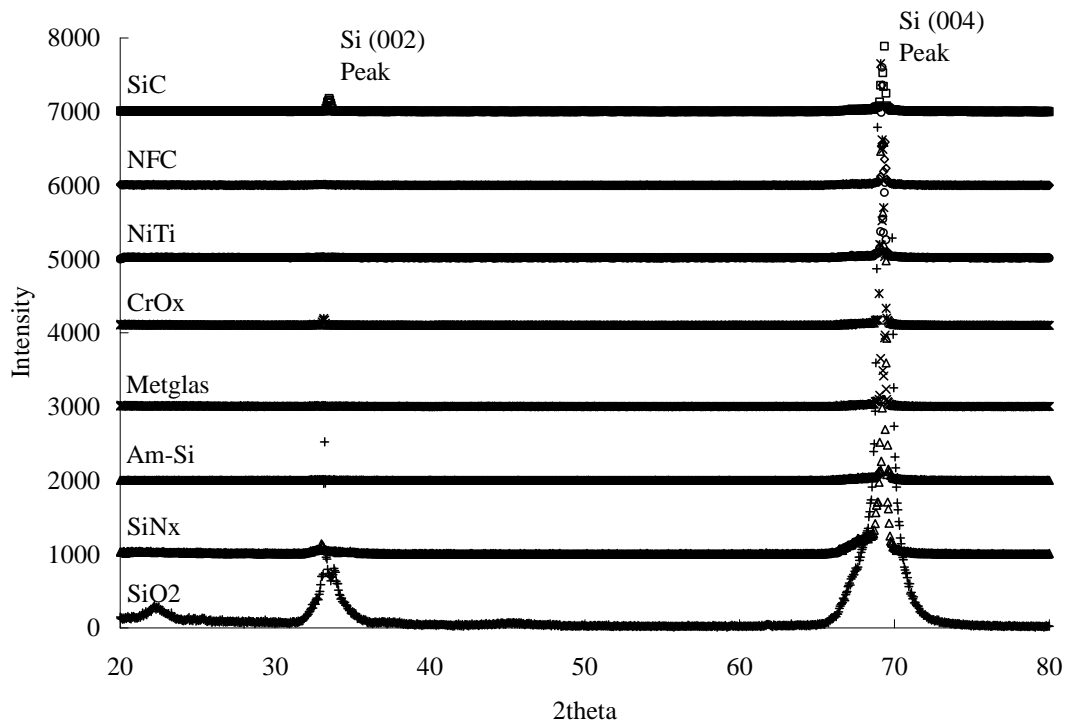


Figure 4.2 XRD spectra for tested materials

4.2 Indentation Impression (Sink-in & Pile-up) Characterizations

The indentation impressions were characterized with a scanning electron microscope (SEM) and an atomic force microscope (AFM). Figure 4.3 shows a SEM image of an impression on NFC/Si after unloading. It supplies general information about the nanoindentation process on the film. For instance, the film surface conditions can be roughly estimated as well as the size and shape of the impression area. It helps to determine whether sink-in (elastic contact) or pile-up (elastic-plastic contact) happened based on McElhaney and Nix's theory introduced in Chapter 2. However, SEM can not tell the vertical degree of the pile-up or sink-in impression. This was why atomic force microscopy was employed.

As a powerful tool, AFM can provide 2-dimensional, 3 dimensional and profile images of an indentation impression. In this study, both sink-in and pile-up phenomena were observed on different tested thin films. Figure 4.4 and 4.5 show the sink-in impressions on NFC/Si (soft film on hard substrate) and ta-C:H (hard film on soft substrate). The triangle shape profile of sink-in resembles the indenter geometry. Unlike the sink-in elastic contact, the plastically deformed pile-up greatly affects the indenter contact area and the accurate determination of film Young's modulus and hardness. Thus, extra caution is needed when dealing with pile-up thin films. As mention above, pile-up usually happens in soft metals on hard substrate. Shown in figure 4.6a, the a-Si film exhibits minor pile-up on silicon substrate as the indentation depth was within the film thickness (The ratio of the pile-up level and indentation depth is less than 1/50). Similar pile-up degree was found in SiO₂ and other soft metal oxide films. An overestimation of the Young's modulus at this level of pile-up is less than 2.5% based on Bolshakov and Pharr's simulation results when $h_f/h_{max} < 0.7$ (the ratio of final depth after unloading to the depth at maximum load) [67]. However, if the indentation depth is greater than the film thickness, the indenter will penetrate into the substrate. It is known that the pile-up from the Si substrate will greatly affect the total pile-up degree on the film [111]. As shown in figure 4. 6b, a 500nm indentation on a-Si film (450 nm thick) has a much greater pile-up (The ratio of the pile-up level and indentation depth is greater than 1/6!) than that from the 300 nm indentation in figure 4.6a. The effect from the substrate indentation part causes overestimation of the Young's modulus up to 30%. Thus, in this research, the data acquisition from

nanoindentation was strictly limited to the film thickness region so as to minimize the pile-up effect from the Si substrate.

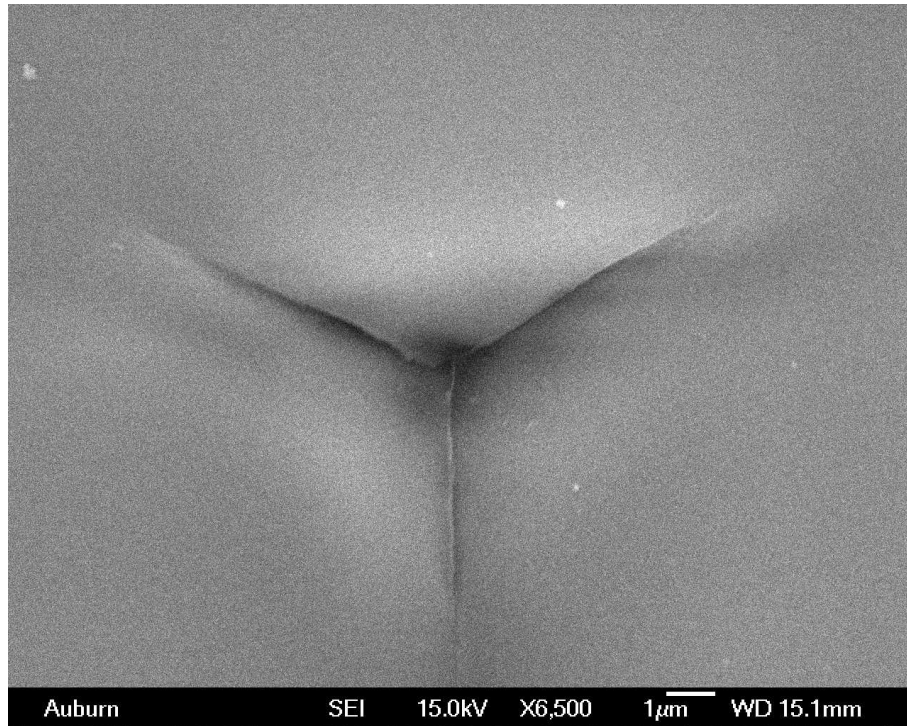


Figure 4.3 SEM image of an indentation impression on NFC/Si.

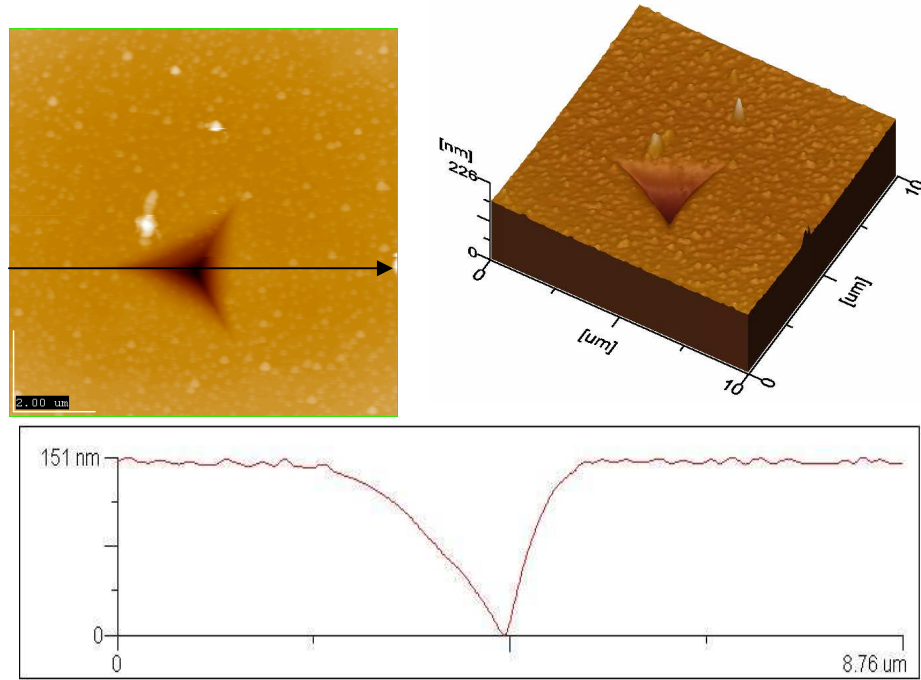


Figure 4.4 AFM images of a sink-in impression of 300 nm indentation on NFC/Si

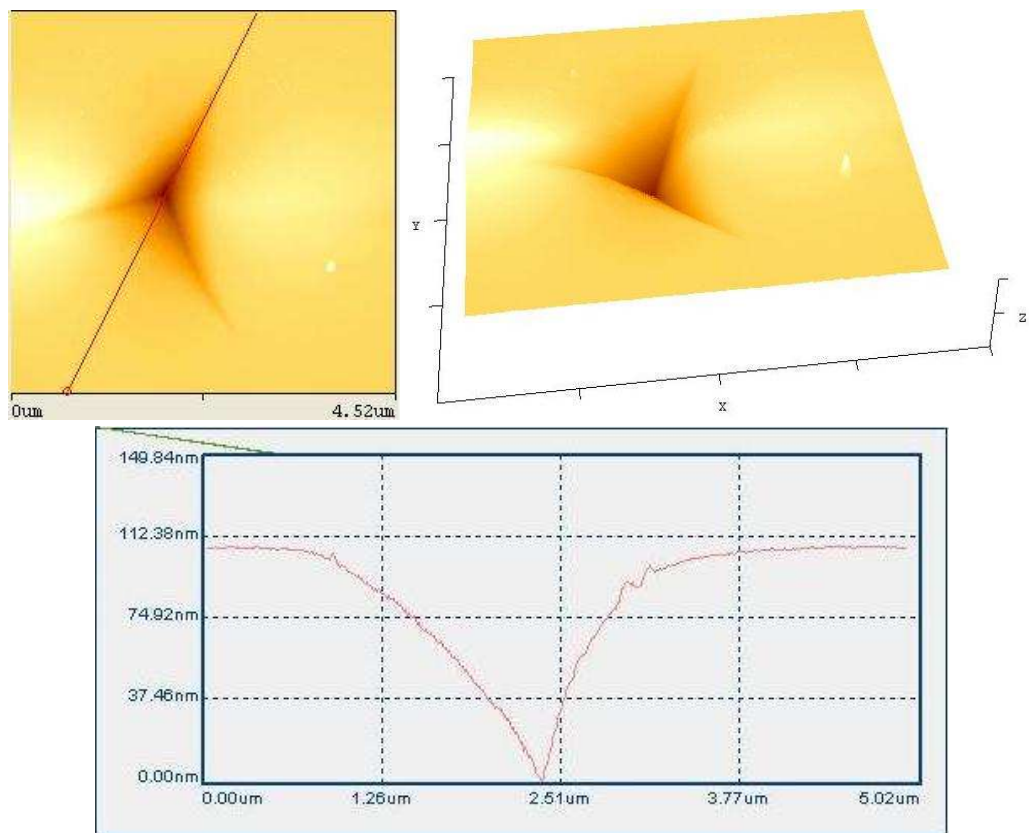


Figure 4.5 AFM images of a sink-in impression of 500 nm indentation on ta-C:H/Si

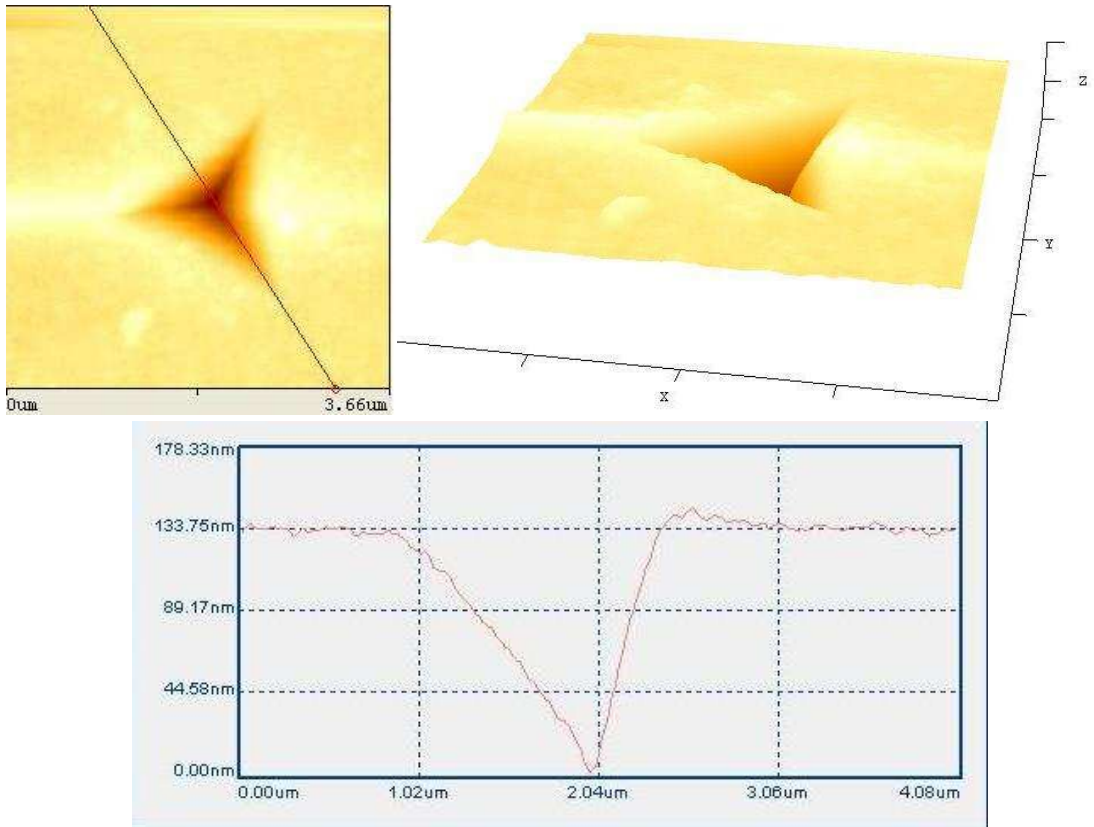


Figure 4.6a AFM images of a pile-up impression of 300 nm indentation on a-Si film (450 nm) on silicon substrate. (The indenter remained in the film and didn't go into the substrate)

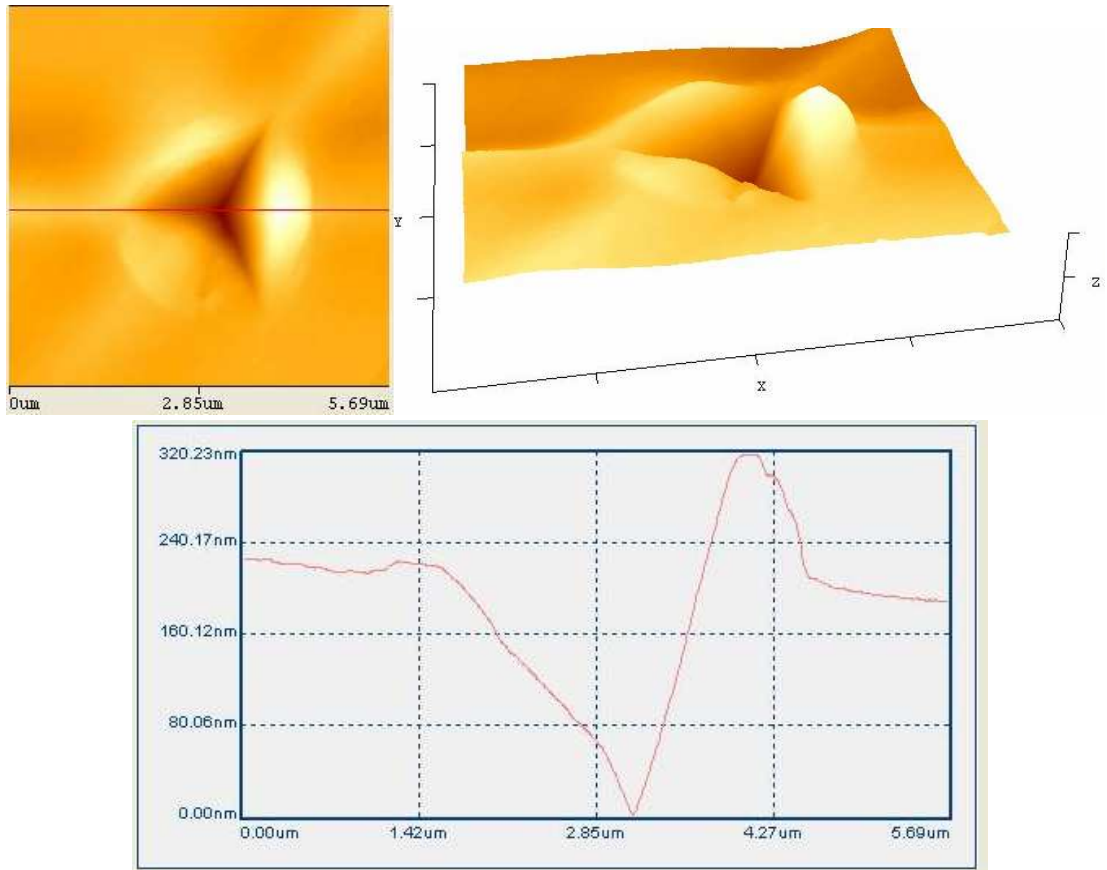


Figure 4.6b AFM images of a pile-up impression of 500 nm indentation on a-Si film (450 nm) on silicon substrate (The indenter penetrated the film and went into the Si substrate)

4.3 Film Young's modulus and Critical indent depth determination

Raw CSM nanoindentation data of the thin films were input into Analyst (data processing software for the MTS-Nano Nanoindenter XP system) for calibration. Figure 4.7a and 4.7b show a typical calibrated CSM modulus-displacement curve for the SiO₂ and SiN_x film on silicon a substrate, respectively. “Flat regions” were observed in the early stage of *E-h* curves for both films softer the substrate and films harder than the substrate. The value in this region strongly indicated the true film modulus with little affection from the substrate. In this study, an empirical guideline

was suggested to roughly estimate the region length: The end of the flat region or the critical indentation depth (h_{cr}) was defined when the measured modulus value changed more than 1% from the identified average modulus (E_f) calculated from the flat region. For instance in figure 4.7a, h_c was first roughly estimated as 30 nm. The film Young's modulus was then calculated as an average value from this estimated flat region (77 GPa for SiO₂). Finally, h_{cr} was defined as the measured value increased (or decreased for a harder film on soft substrate) 1% from 77 GPa (70 nm for SiO₂). There was one exception from the nanocrystalline diamond (UNCD) film. Due to the large modulus value, its $E-h$ curve has a very short flat region, and the modulus almost started to decrease from the beginning. The h_{cr} , E_f , and their ratio to the film thickness and substrate modulus are listed in table 4.1. It is necessary to mention that all the films had <100> Si wafers as the substrate. The average Young's modulus of the Si substrates was determined as 170 ± 5 GPa from at least 20 indentations on each wafer. The Poisson's ratio was suggested as 0.28 for <100> direction [110].

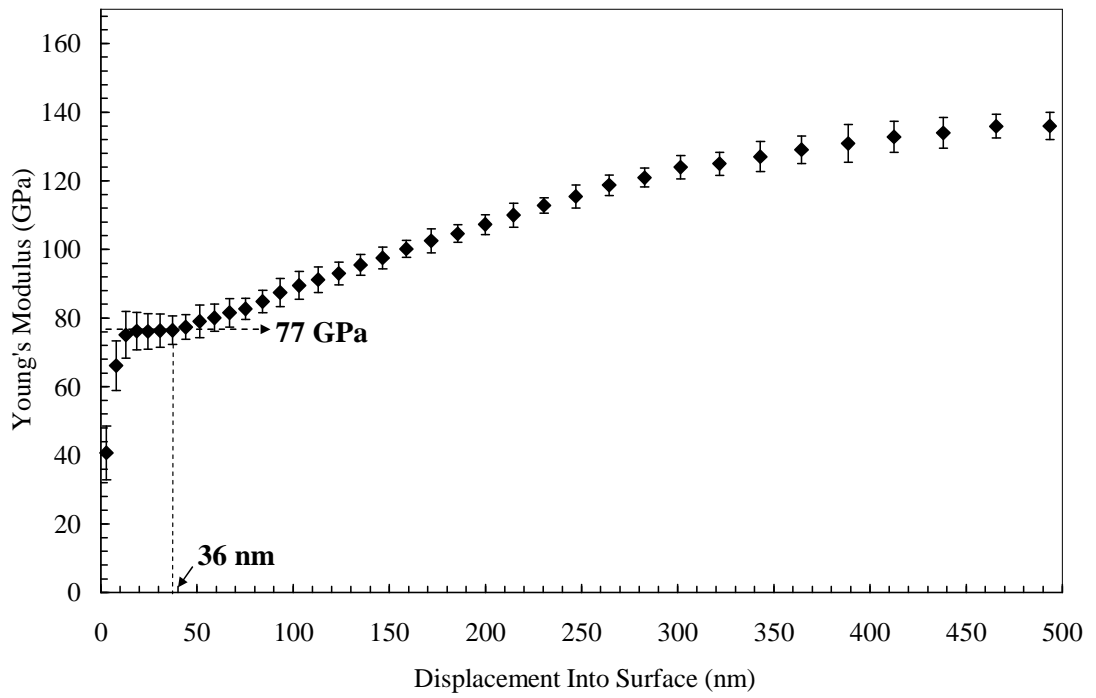


Figure 4.7a SiO₂ film CSM modulus-displacement curve

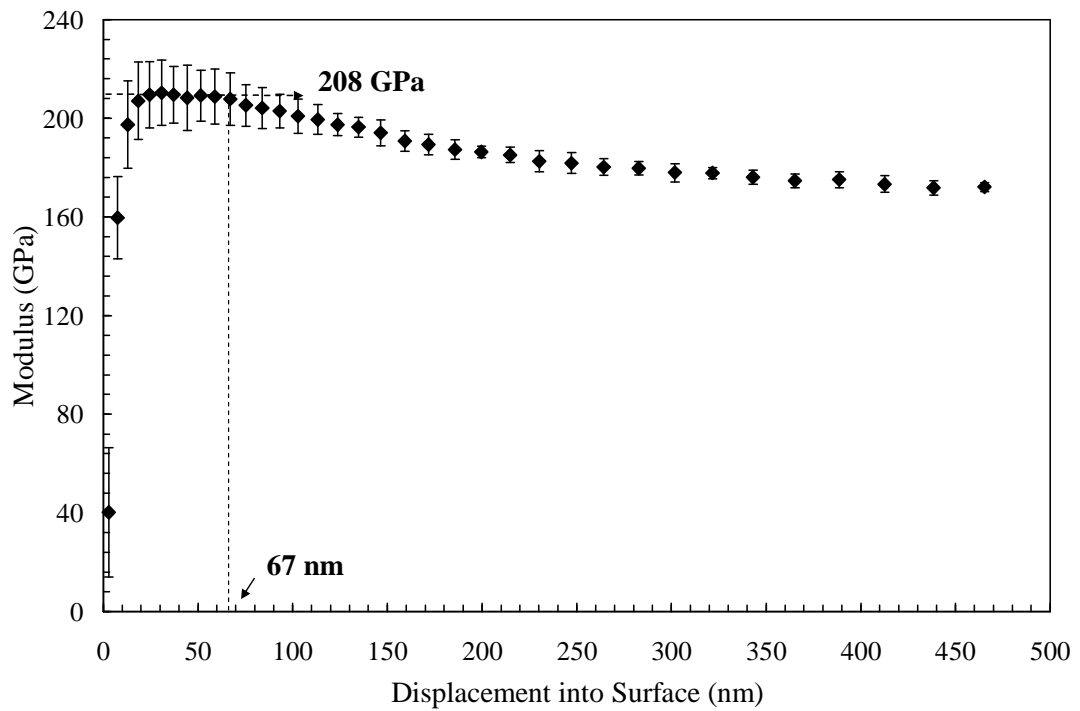


Figure 4.7b Si₃N₄ film CSM modulus-displacement curve

Table 4.1 h_{cr} , E_f , E_f/E_s , and h_{cr}/t for all tested specimens

Thin Films	E_f (GPa)	t (nm)	h_{cr} (nm)	E_f/E_s	h_{cr}/t
Polymer	12	225	20	0.07	0.088
NFC	52	1125	102	0.31	0.090
CrO _x	60	130	12	0.35	0.092
SiO ₂	77	395	36	0.45	0.091
FeO _x	90	105	11	0.53	0.107
TiO _x	103	120	13	0.61	0.108
a-Si	108	450	48	0.64	0.107
AlO _x	115	120	15	0.68	0.125
AlN	133	1000	158	0.78	0.158
FeB	143	1000	188	0.85	0.188
Metglas	180	278	200	1.06	0.719
SiN _x	208	300	67	1.22	0.223
SiC	212	500	93	1.25	0.186
ta-C:H	230	868	87	1.35	0.100
UNCD	573	560	20	3.35	0.036

The relation between the ratio of the critical indent depth to the film thickness (h_{cr}/t) and the ratio of film/substrate modulus (E_f/E_s) is described in figure 4.8. Different from the traditional way of using displacement as a variable, figure 4.8 has E_f/E_s as the x coordinate, because the critical indent depth was influenced by E_f/E_s , not

vice versa. According to the figure, many tested materials still follow Bückle’s 10% indent depth rule to avoid substrate effects. We should give more credibility and confidence in thin film nanoindentation technique. However, it is important to notice that as the films elastic modulus approached that of the substrate the h_{cr} percentage started to increase in a unique nonlinear fashion. Moreover, as the film was much harder or softer than the substrate, this percentage drops lower than the 10% line. The solid curves in the plot are drawn to suggest a trend and are not generated from curve fitting or an analytical solution. The existence of the “flat region” and its relation to the film/substrate materials led us to further investigate the Doerner & Nix equation. . Also, as the flat region of $E-h$ in early indentation indicates the true film modulus, accurate determination of the trend of h_{cr}/t vs. E_f/E_s might help us understand the mechanism

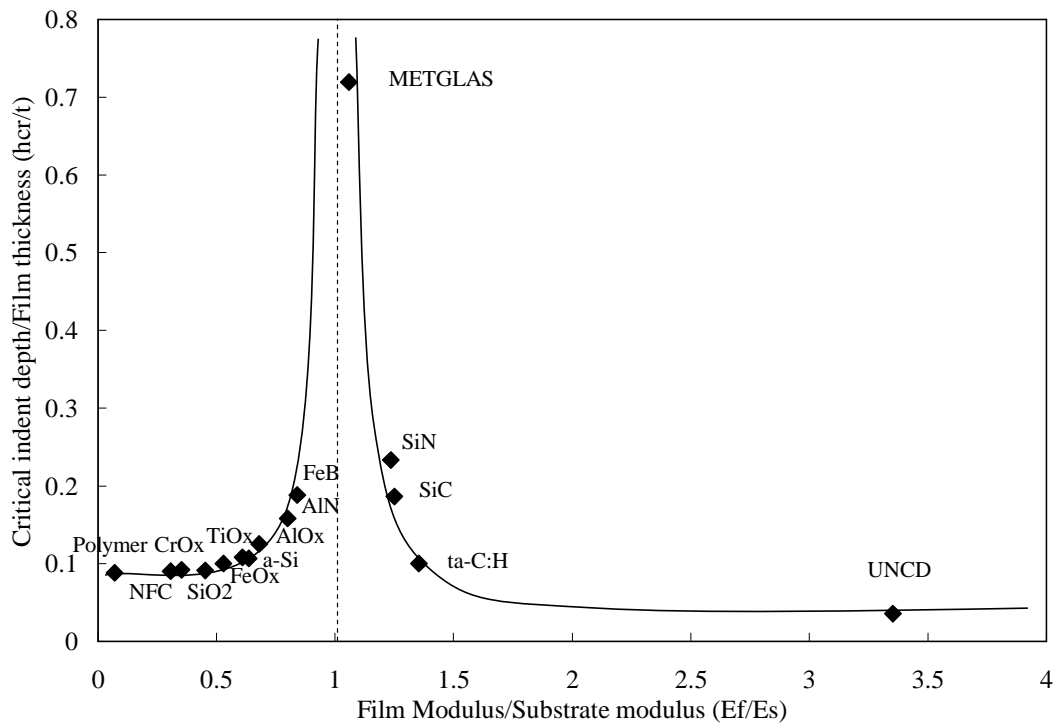


Figure 4.8 h_{cr}/t vs. E_f/E_s for all tested specimens

From now on, softer films on Si substrate ($E_f < E_s$) and harder films on Si substrate ($E_f > E_s$) will be dealt with respectively. Before defining the theoretical solution for the h_{cr}/t curves, there is one more important aspect required to be analyzed: the film thickness effect to h_{cr} . In other words, for each film material, does h_{cr}/t change with film thickness? Nanoindentation tests were performed on NFC film with different thickness, as shown in table 4.2 and figure 4.9. It is found that all the NFC films had similar positions in the plot, which indicated the film thickness should have no effect on the ratio as long as the E_f/E_s is the same.

Table 4.2 h_{cr}/t and E_f/E_s data NFC films with different thickness

Thin Films	E_f (GPa)	E_f/E_s	h_{cr} (nm)	t (nm)	H_{cr}/t
NFC	52	0.31	102	1125	0.090
NFC	48	0.28	34	380	0.088
NFC	50	0.29	14	150	0.093

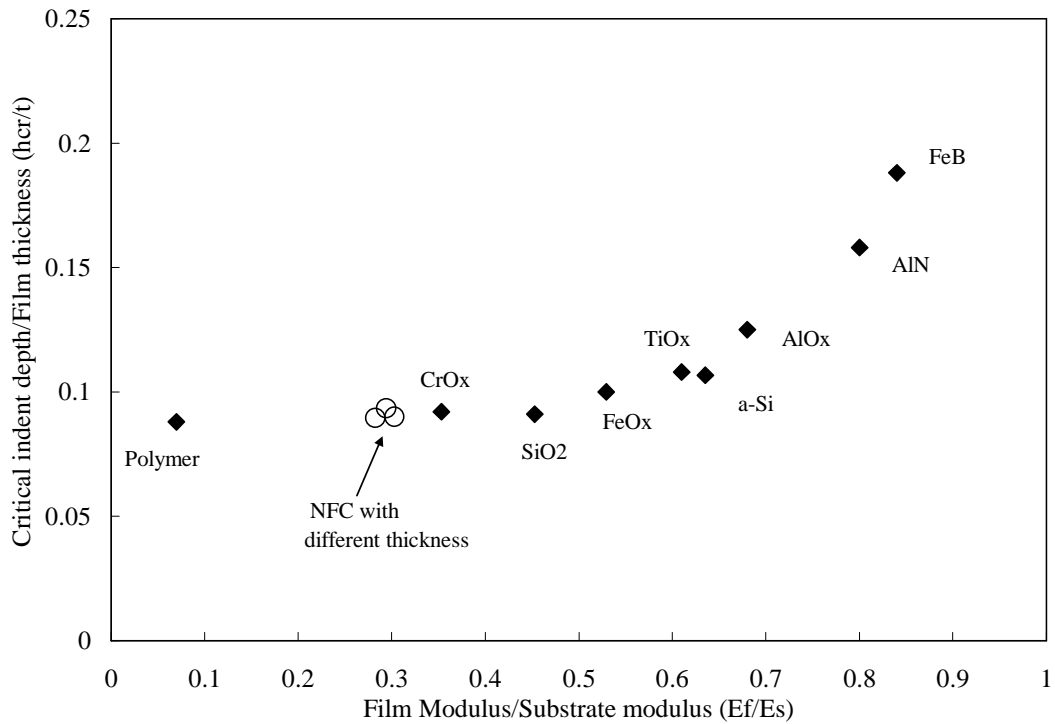


Figure 4.9 Positions of the NFC films with different thickness in h_{cr}/t vs. E_f/E_s ($E_f < E_s$)

4.4 Doerner & Nix function investigation

As mentioned in chapter 2, there are two major functions for thin film nanoindentation: Doerner & Nix, and Gao. The Doerner & Nix function suggested that within a small indentation depth, the substrate effects can be neglected. While in Gao's model, the measured modulus increases as long as the indenter touches the film. Since our experimental data matches Doerner & Nix's description, investigation will be mainly focused on their model. As shown Eq. (2), Doerner & Nix equation was developed to describe the indentation $E-h$ curve using an empirically determined constant α as 0.25. Using the same criterion of 1% change of the modulus value ($E=(1+1\%)E_f$) to determine h_{cr} , one can change Eq. (12) to the function below:

$$\frac{h_{cr}}{t} = \frac{\alpha}{\ln(1 - E_f/E_s) - \ln(1/100)} \quad (17)$$

Re-plotting Figure 4.8 with the theoretical curves obtained from Eq (17) in Figure 4.10a and 4.10b (for $E_f < E_s$ and $E_s < E_f$, respectively), one can find the experimental and Doerner & Nix curves have the similar trend. However, for films softer than the substrate, the experimental points were obviously above the theoretical line. In other words, for each film/substrate system, the flat region was longer than that of the Doerner & Nix function expected. When E_f approached E_s , this deviation became greater. From the figure, we directly got an idea that α at least was not a universal constant for all the materials. And more importantly, the h_{cr} was not solely determined by the modulus difference between film and substrate, but also was affected by α . For films harder than the substrate, Figure 4.10b indicates that the Doerner & Nix function does not always underestimate the flat region length. The diamond film had serious substrates and sink-in effects even from the beginning of the indentation, for which the Doerner & Nix function can not extrapolate.

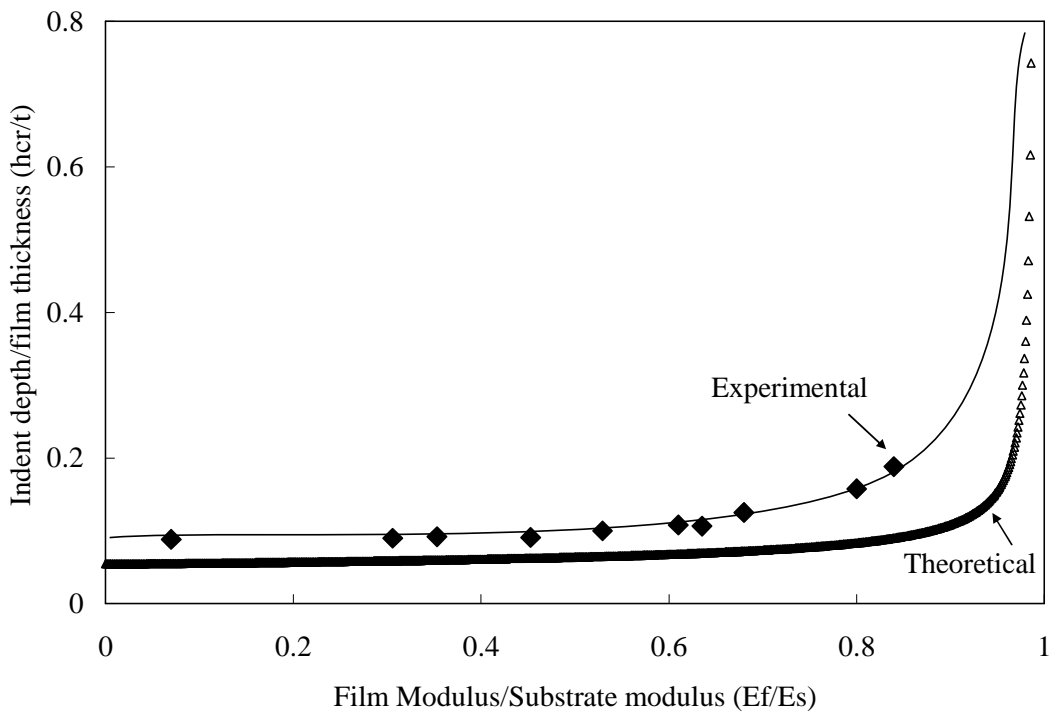


Figure 4.10a The experimental and theoretical curves of $h_{cr}/t-E_f/E_s$ for $E_f < E_s$

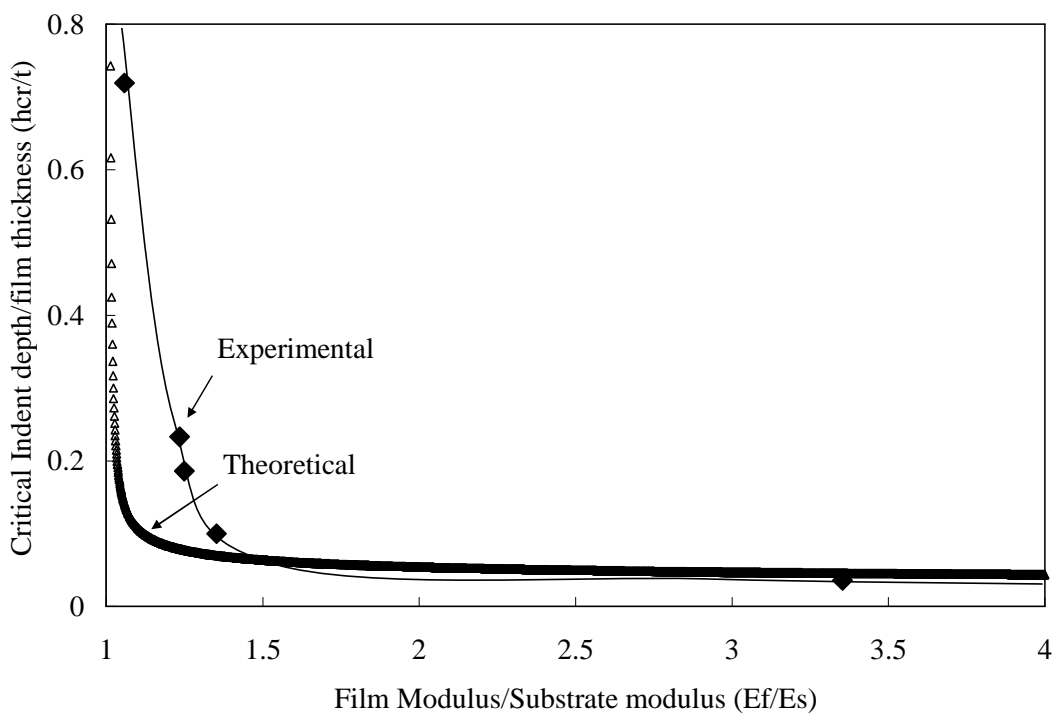


Figure 4.10b The experimental and theoretical curves of $h_{cr}/t-E_f/E_s$ for $E_f > E_s$

To better understand how α affects the Doerner & Nix function, the experimental CSM curve of SiO₂ was compared with theoretical curves having α of 0.1, 0.25, and 0.5 in figure 4.11. It was obvious that a smaller α indicated a faster (more abrupt) changing of the measured modulus from the film value to the substrate value. In other words, smaller α yields shorter flat region (h_{cr}) and greater substrate effects. On the contrary, a relatively large α slows down the changing trend of the measured modulus and has a greater h_{cr} .

Based on Eq. 17 and the experimentally determined h_{cr} , α at h_{cr} for each material can be calculated and plotted versus E_f/E_s , as shown in figure 4.12a and 4.12b. It is found α (at h_{cr}) increases as $E_f < E_s$, and decreases when film is hard than the substrate.

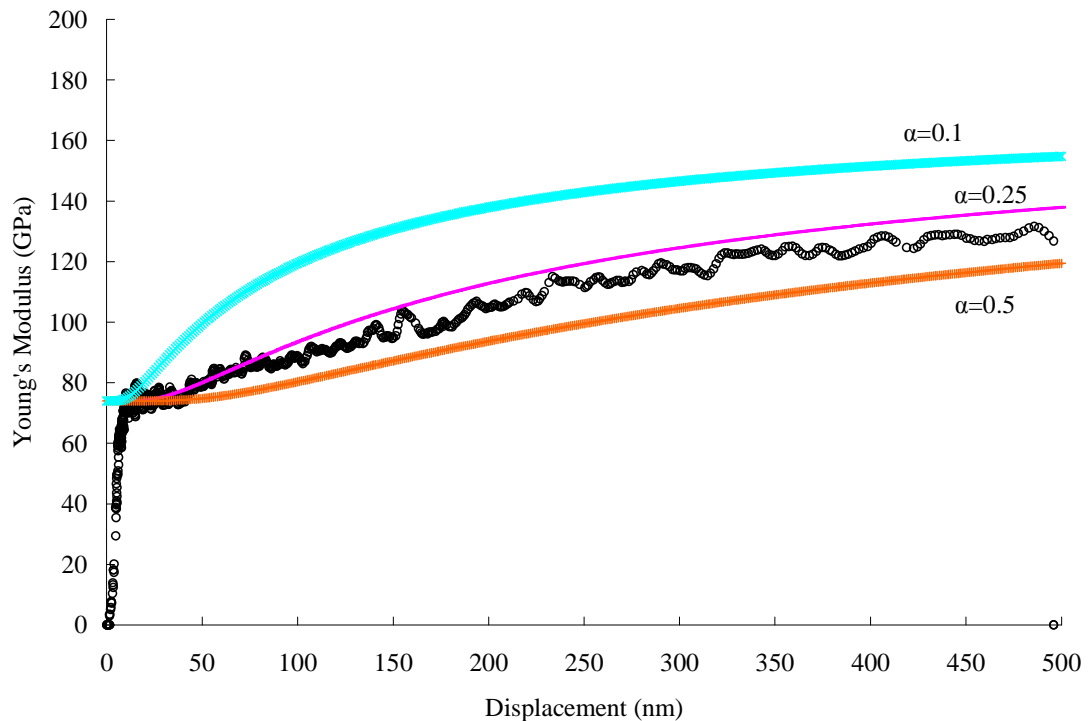


Figure 4.11 SiO₂ modulus-displacement curve with theoretical curves having α (α) of 0.1, 0.25, and 0.5

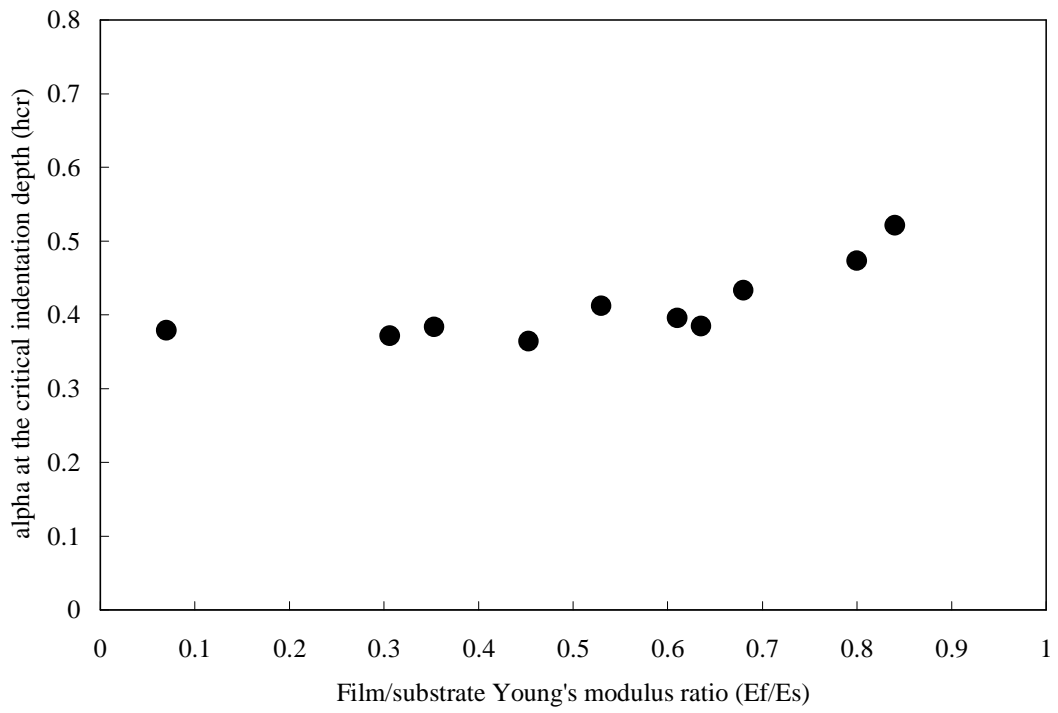


Figure 4.12a Plot of α value at critical indentation depth vs. E_f/E_s for tested materials

with $E_f < E_s$

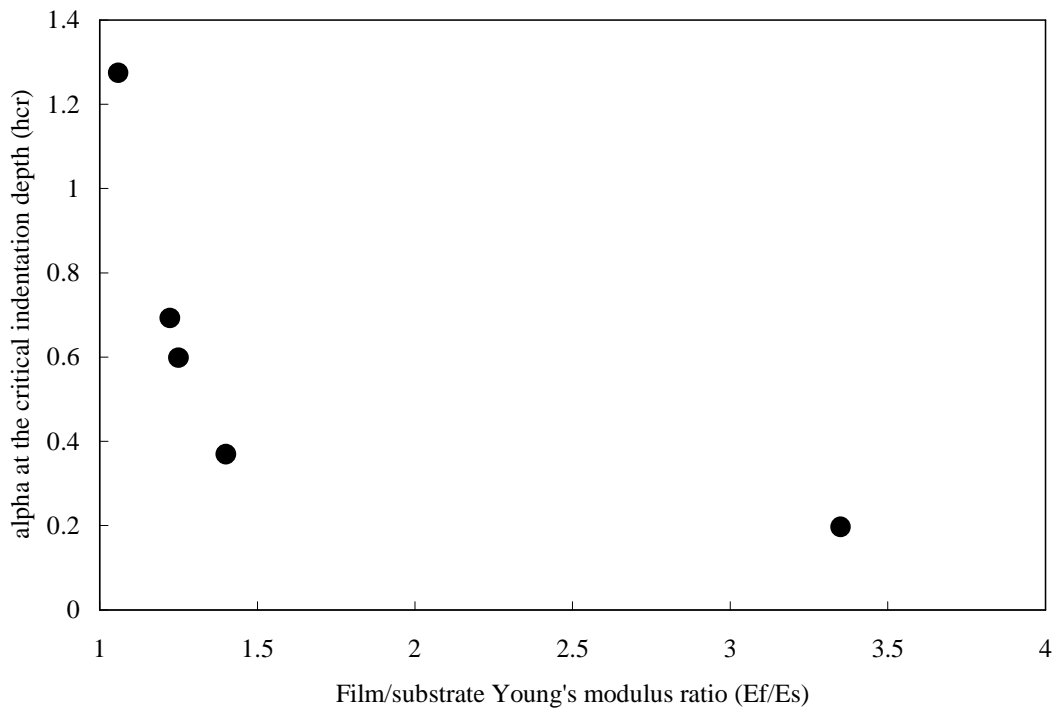


Figure 4.12b α value at h_{cr} vs. E_f/E_s for tested materials with $E_f > E_s$

Now, an important question arises: Is α a constant for each film/substrate combination? In applying the experimental data to Eq. (12) we were able to plot the parameter α in the Doerner & Nix function versus indentation depth. It was interesting to find that α was not only different for each film material, but was not constant with displacement either. A typical α - h curve from a single CSM indentation test on the NFC film is shown in figure 4.13. A similar trend was found in all other materials tested for both soft on hard (SiO_2/Si , figure 4.14) and hard on soft (ta-C:H/Si, figure 4.15) situations. It is interesting to note that the α - h curve peaks are at the critical indentation depth (h_{cr}) when contrasting with the film E - h curve. As the substrate effect is negligible in the flat region, α appeared to have no physical meaning here, or more precisely is close to infinity.

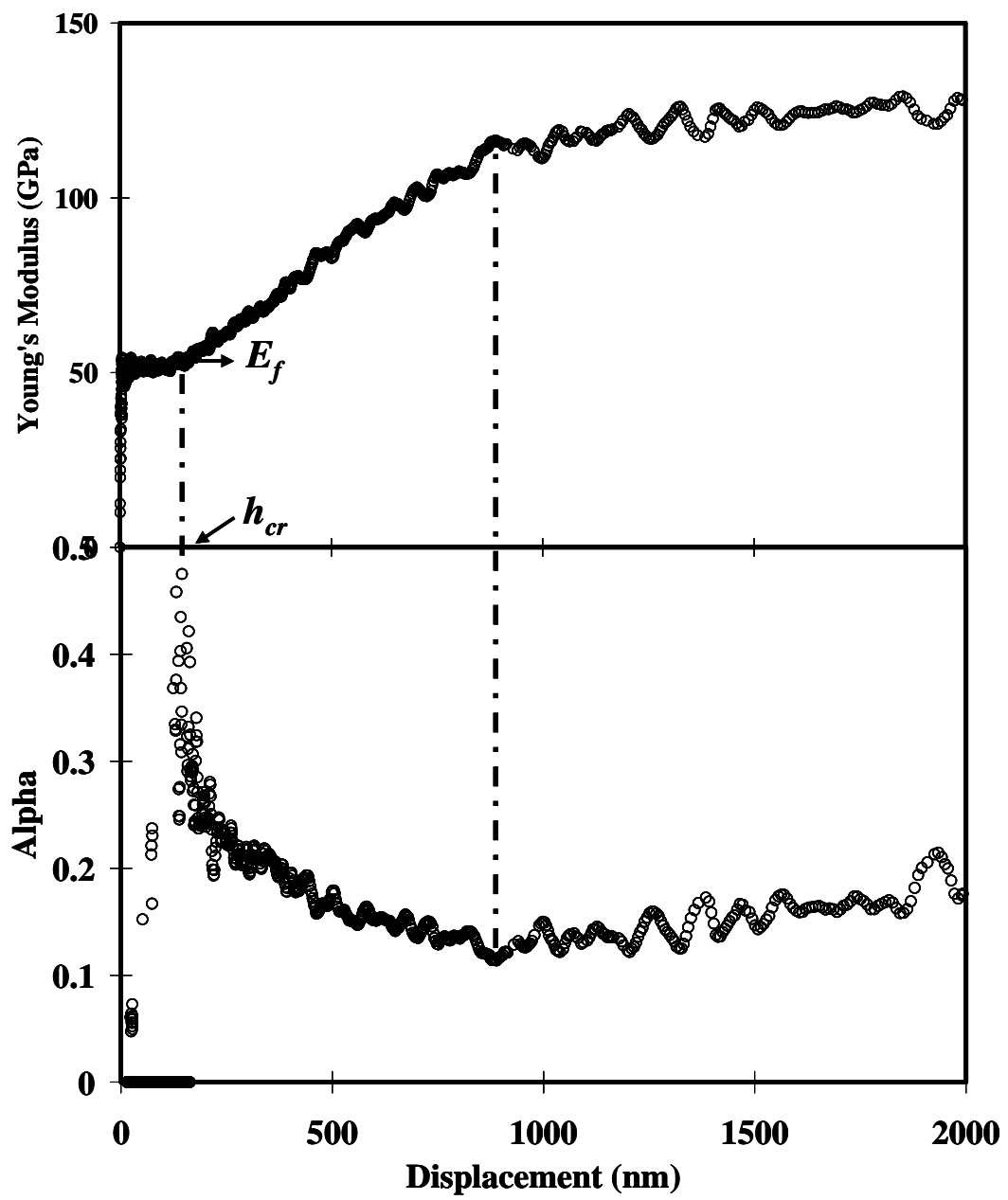


Figure 4.13 Plot of α vs. h for the NFC film contrasted with the E - h curve

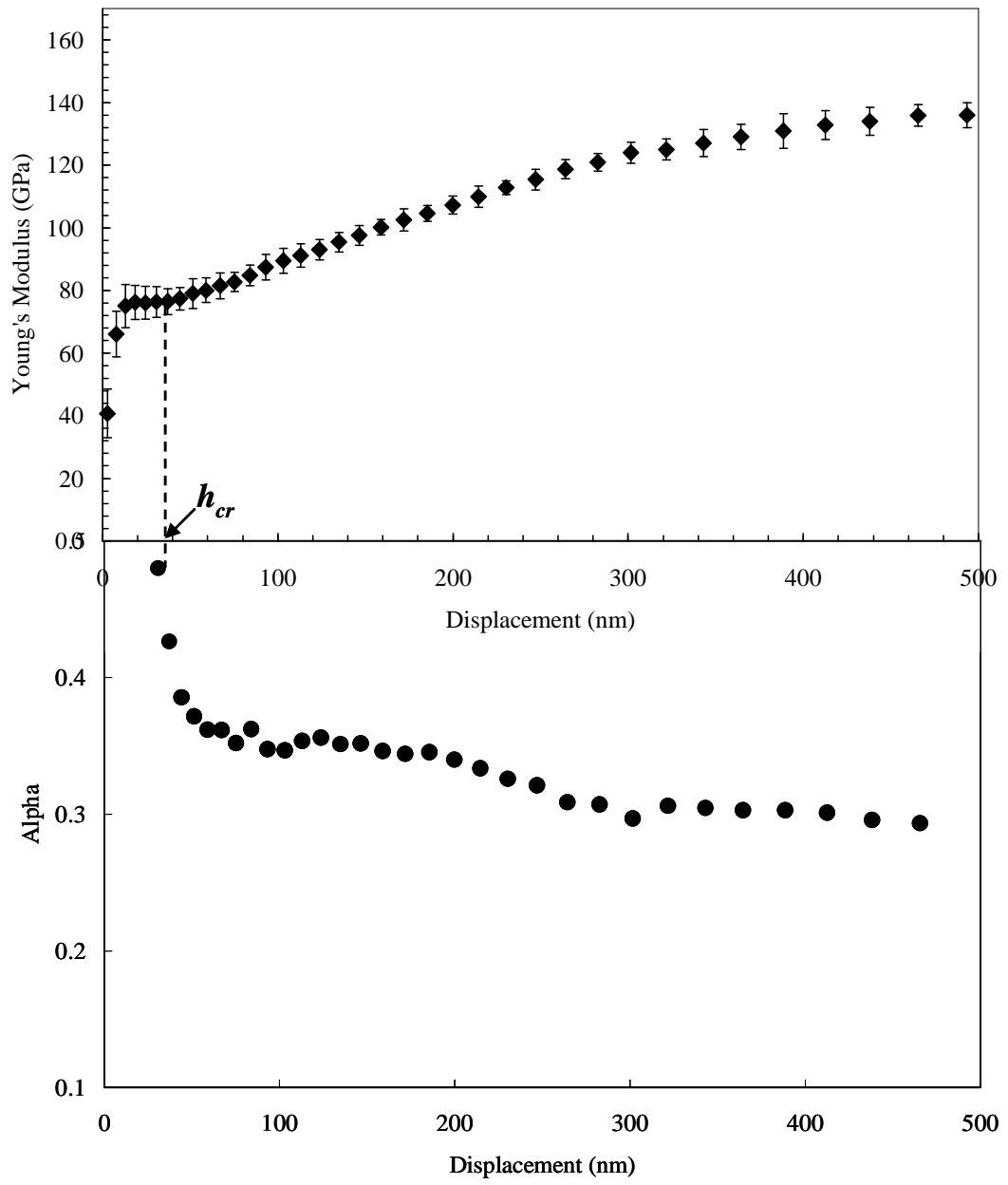


Figure 4.14 Plot of α vs. h for the SiO_2 film contrasted with the E - h curve

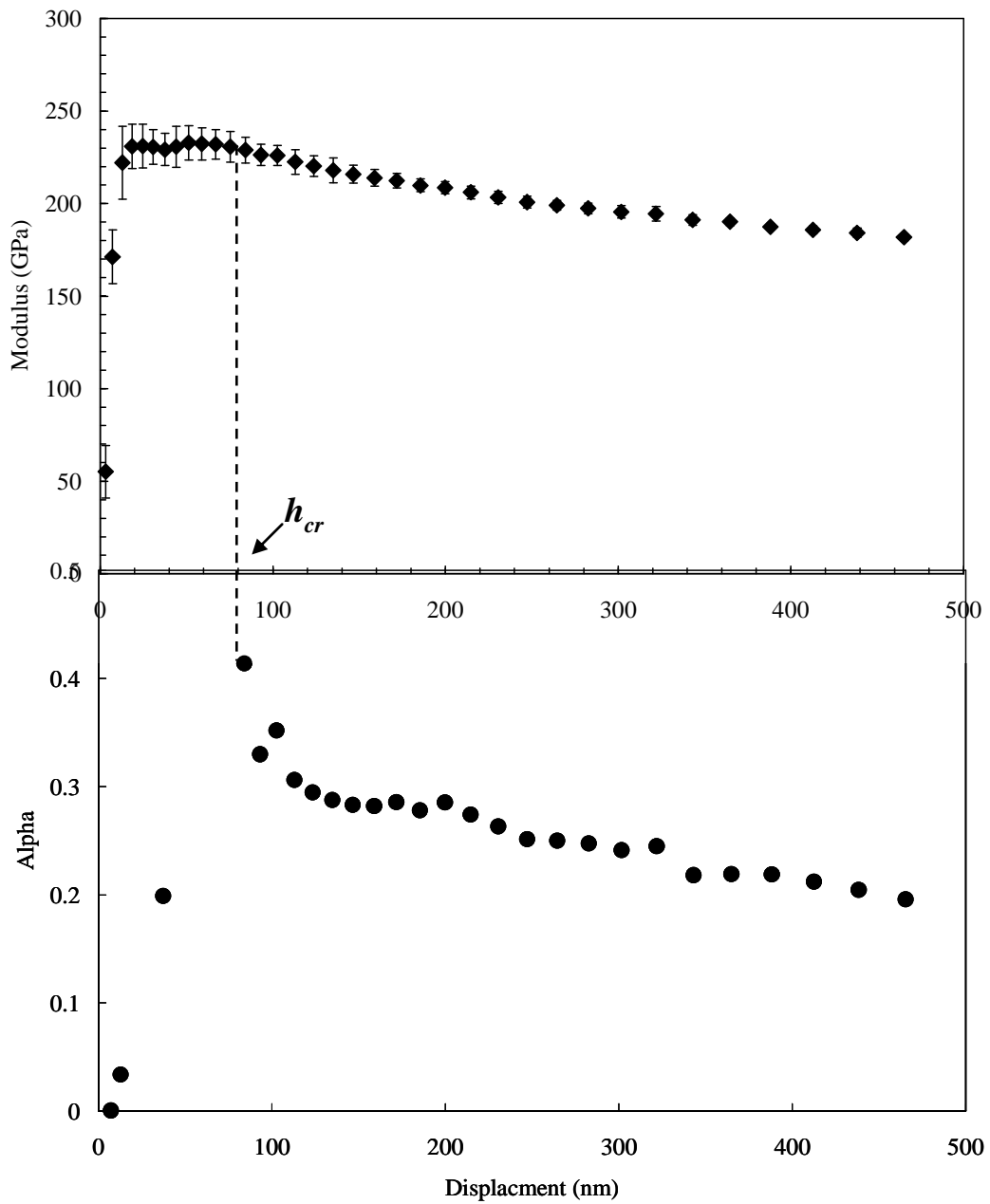


Figure 4.15 Plot of α vs. h for the ta-C:H film contrasted with the $E-h$ curve

4.5 Alpha (α) parameter determination

Based on the results in last section, it is reasonable to suggest alpha (α) as a power function of h shown in figure 4.16. Numerous empirical solutions of α were proposed in the previous preliminary work. Although a power function like Eq. (18)

fits better with the experimental data than the Doerner & Nix function, it lacks a physical explanation to support the assumption. Moreover, a changing alpha parameter will only bring more complexity to the empirical Doerner & Nix function. It is against the original idea of building up a simple and universal solution to extrapolate the thin film indentation mechanism. To find the true physical meaning behind alpha, finite element analysis is needed.

$$\alpha = (h/t)^k \quad (18)$$

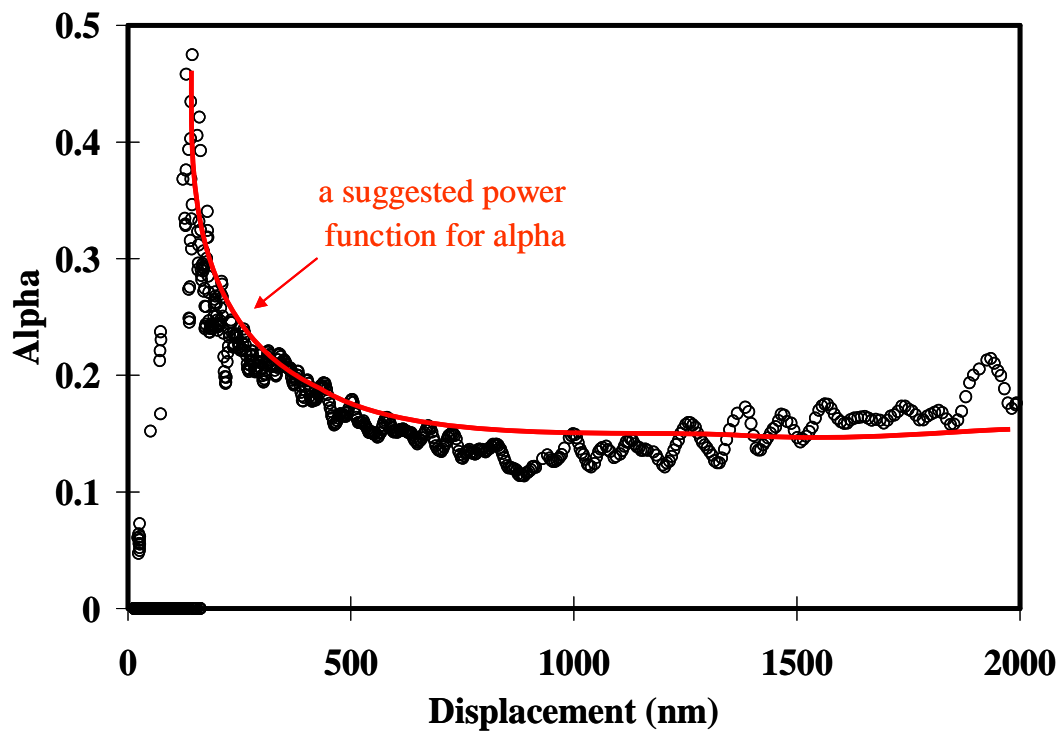


Figure 4.16 A suggested power function of h for alpha.

Before introducing the FEA results, let us rearrange Eq. (12) to get a better picture of the role of alpha plays in the Doerner & Nix function:

$$\frac{1}{E} = \frac{1}{E'_f} [1 - e^{-\alpha(t/h)_c}] + \frac{1}{E'_s} e^{-\alpha(t/h)_c} \quad (19)$$

From Eq. (19), the Doerner & Nix function can be suggested as contributions from the film and substrate compliance weighted by the exponential fraction coefficient. As the sum of the fractions equals to 1 and there is only one parameter (α) controlling the factor, the Doerner & Nix function describes a consistent change of the elastic strain intensity distribution in film and substrate along with the displacement. The assumption is reasonable in a mathematical (theoretical) concern. However, in reality, the elastic strain growth in the specimens will be affected by the film/substrate mechanical properties. Thus some degree of the discontinuity of the elastic strain distribution can be expected.

A schematic of the estimated elastic strain growth in the specimen is shown in figure 4.17. Let us imagine the strain change in the specimen at different indentation depth. At the beginning of the indentation, elastic deformation starts to develop in the specimen and most of the strain energy is confined in the film. The strain intensity in the film is much larger than that in the substrate, which is why there could be a flat region that reflects the true film modulus. As the tip penetrates deeper into the film, the elastic strain intensity begins to grow in both the film and the substrate but in a different manner. Taking NFC/Si as an example, the NFC atoms are easier to move from their original positions than silicon atoms due to the smaller shear modulus. Thus, the strain development in the NFC film should not be uniform in any direction

but follow a preferred manner of growing laterally. Thus for each small indent depth change (Δh), the elastic strain growth in the film ($\Delta \epsilon_f$) is larger than that in the substrate ($\Delta \epsilon_s$).

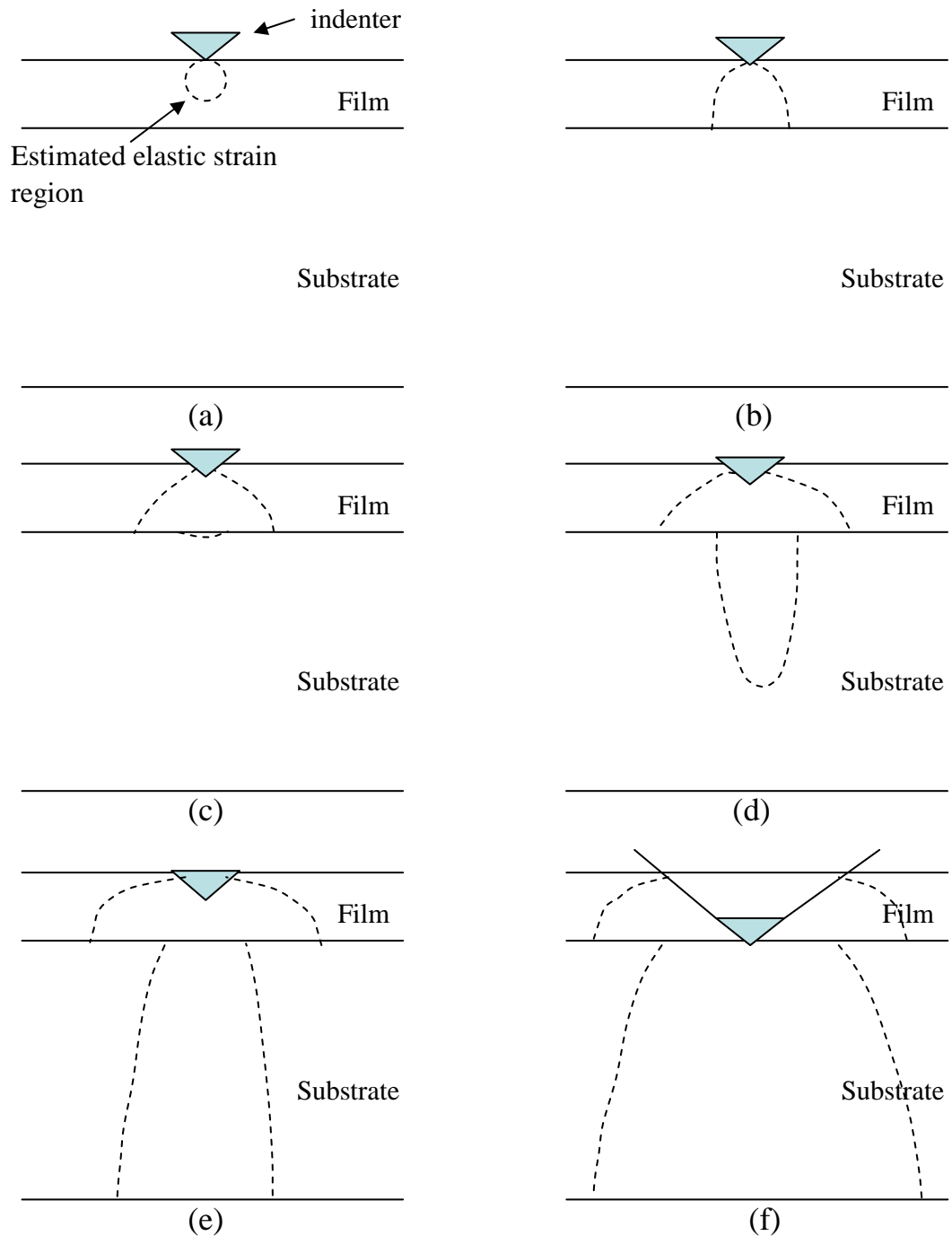


Figure 4.17 Schematic of certain degree of the elastic strain growth in the specimen with increasing indent depth: (a) 20 nm; (b) 50nm; (c) 130nm; (d) 500nm; (e) 1000nm; (f) 2000nm

Finite element analysis (FEA) was employed in this study to observe the elastic strain growth manner in the film and substrate during nanoindentation. Figure 4.18a to 4.18e show the FEA results of indentation at 8, 30, 50, 100, and 250nm into the NFC/Si specimen. The simulation results strongly support the suggested schematic of the elastic strain growth in figure 4.17. At 8 nm indentation, most of the elastic strain is confined in the film. From 8nm towards 100 nm, though the substrate starts to deform elastically, the major part of the elastic strain still prefers to grow latterly in the film. After 100nm indentation for NFC, the elastic strain intensity in the film is getting saturated and the film can no longer sustain much more strain accumulation, and should pass most of the deformation energy into the substrate. From this point, the strain growth in the substrate becomes faster than that in the film. Thus, the measure modulus starts to increase quickly toward the substrate value. Moreover, it is found that the radius of the elastic strain contact area at the interface of film and substrate is another important parameter for characterizing substrate effects. Based on the simulation results, we found that in the early stage of the indentation, the strain contact area grew faster and reached a certain size. When substrate effects start to prevail, the contact area grew much slower, which strongly indicated the elastic strain saturation in the film. The elastic contact area information could help us better understand the strain development in the early stage of indentation and will be carefully investigated in later study.

Moreover, a gap was found between the same scale of the elastic strain (i.e. 0.1% strain) at the interface of film and substrate. This illustrates the inconsistent

elastic strain flow from film to substrate. Similar discontinuity was observed when indenting on hard film/soft substrate combination as shown in figure 4.19 for ta-C:H/Si. The gap degree is influenced by the different mechanic properties of the film and substrate (Young's modulus and Poisson's ratio). It is also interesting to see that even for the same materials combination (i.e, Silicon film on diamond substrate, and diamond film on Si substrate), the manner of the strain discontinuity is different, see figure 4.20a and 4.20b.

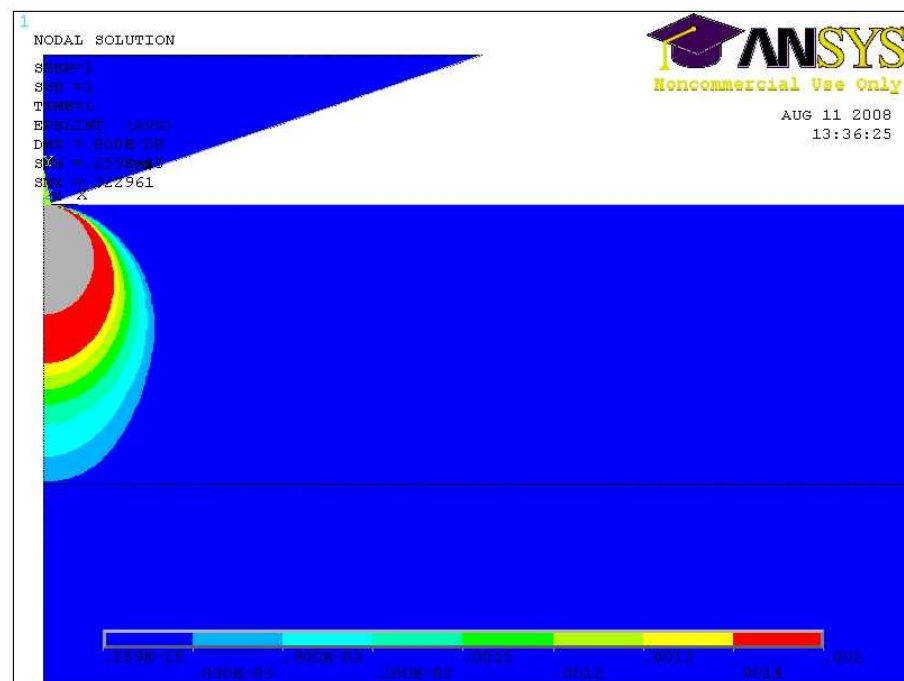


Figure 4.18a FEA image of the elastic strain distribution in NFC/Si specimen at 8nm indentation depth.

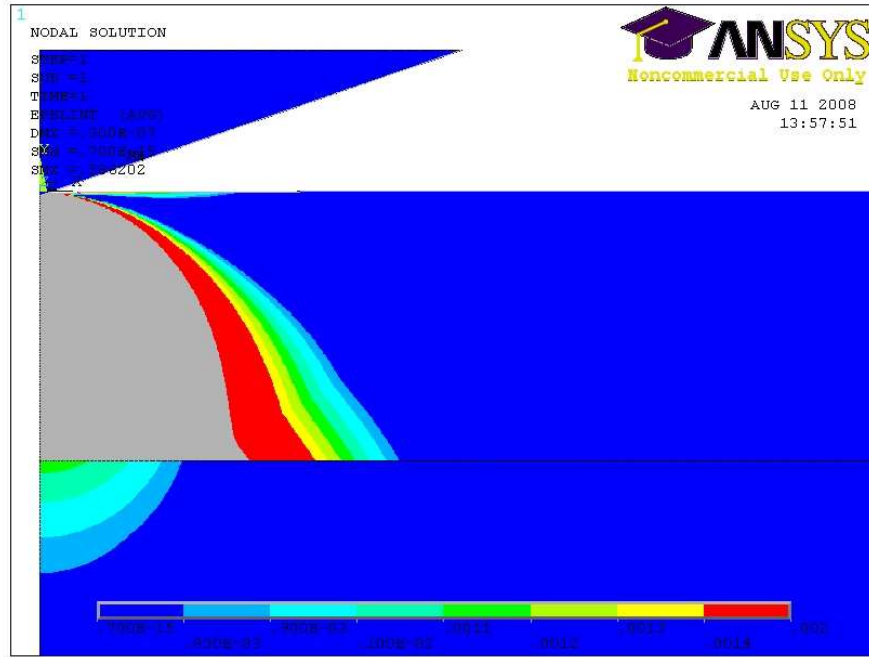


Figure 4.18b FEA image of the elastic strain distribution in NFC/Si specimen at 30nm indentation depth.

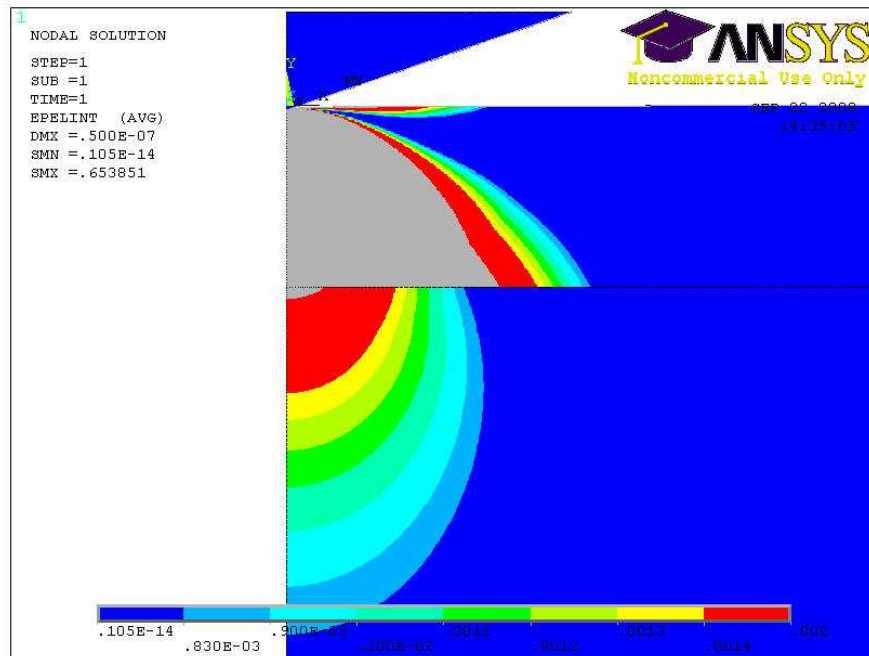


Figure 4.18c FEA image of the elastic strain distribution in NFC/Si specimen at 50nm indentation depth.

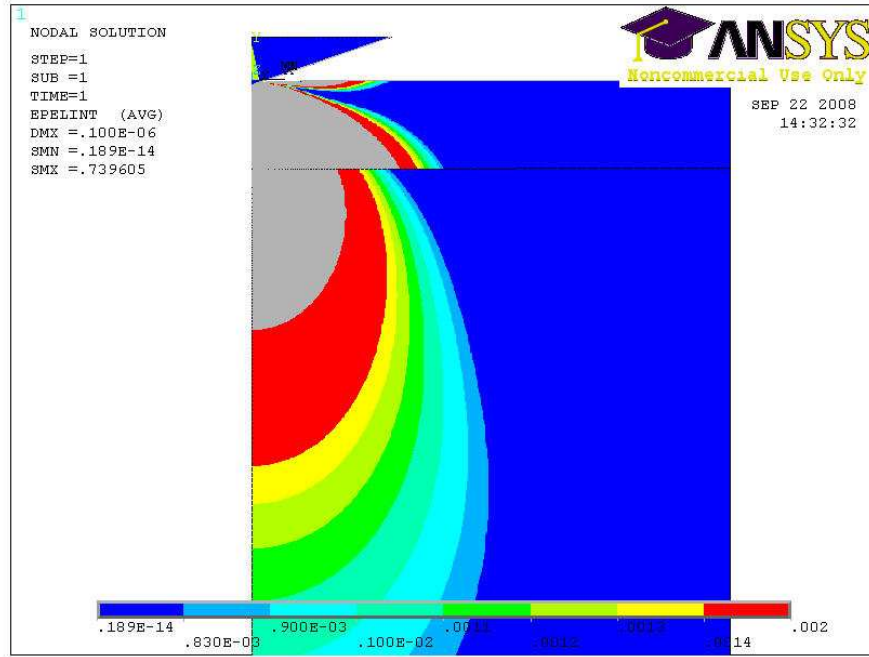


Figure 4.18d FEA image of the elastic strain distribution in NFC/Si specimen at 100nm indentation depth.

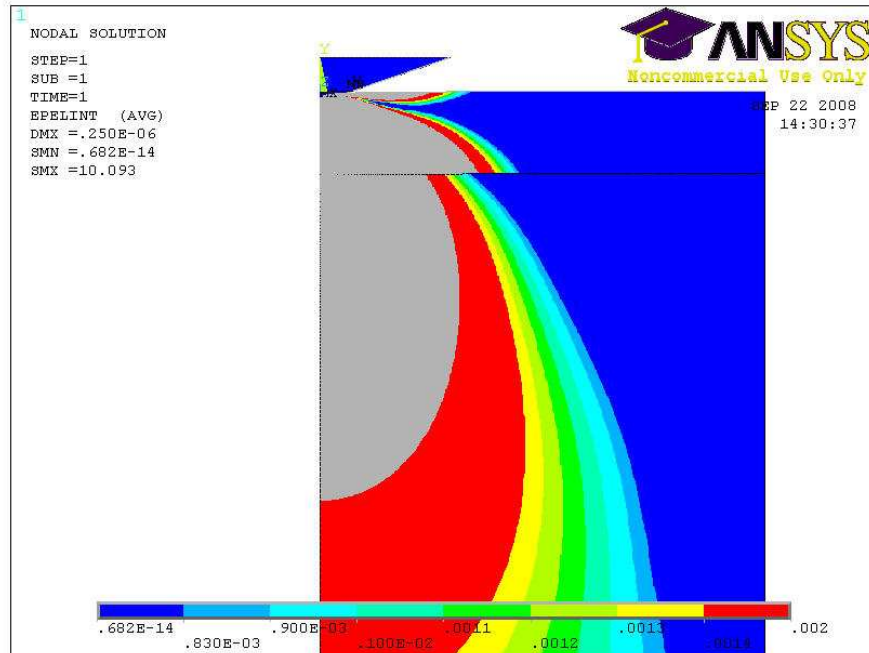


Figure 4.18e FEA image of the elastic strain distribution in NFC/Si specimen at 250nm indentation depth.

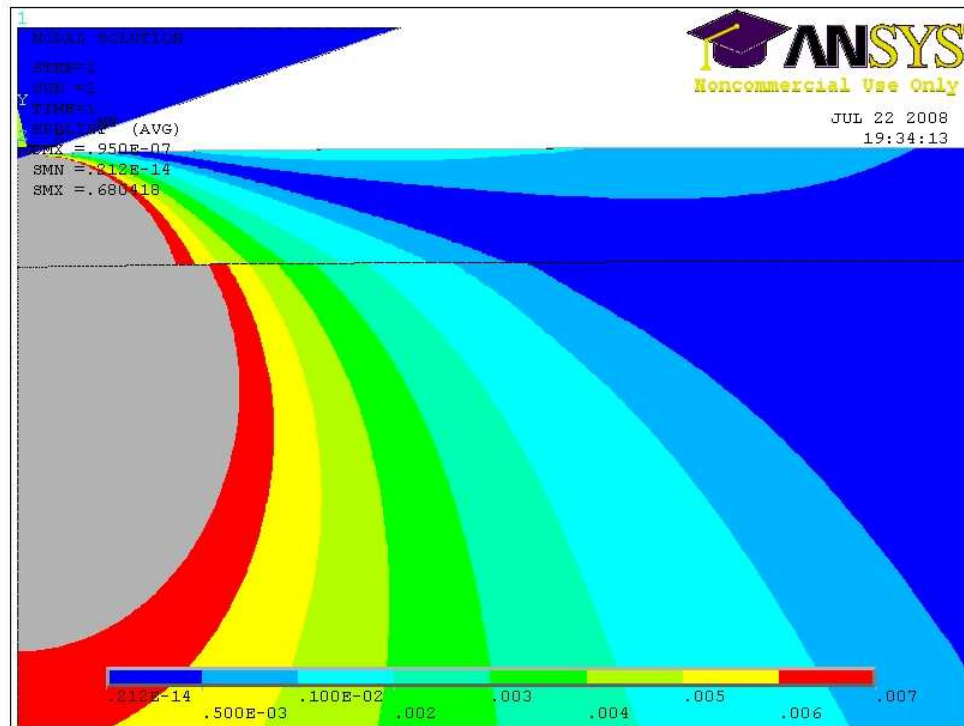


Figure 4.19 FEA image of the elastic strain distribution in ta-C:H/Si at 100nm indentation depth.

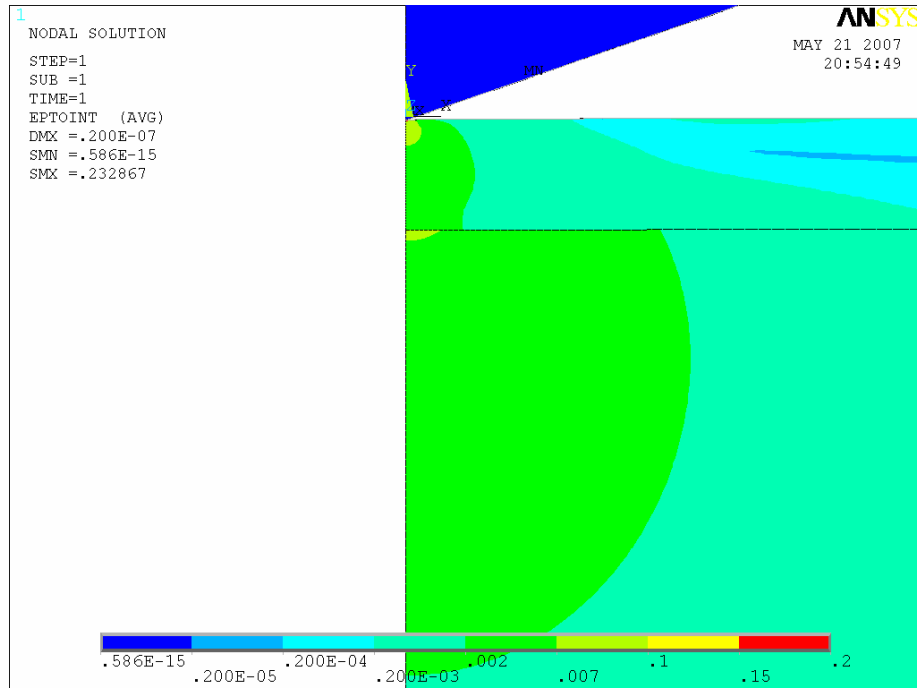


Figure 4.20a FEA result of indenting 20 nm into diamond film on Si substrate

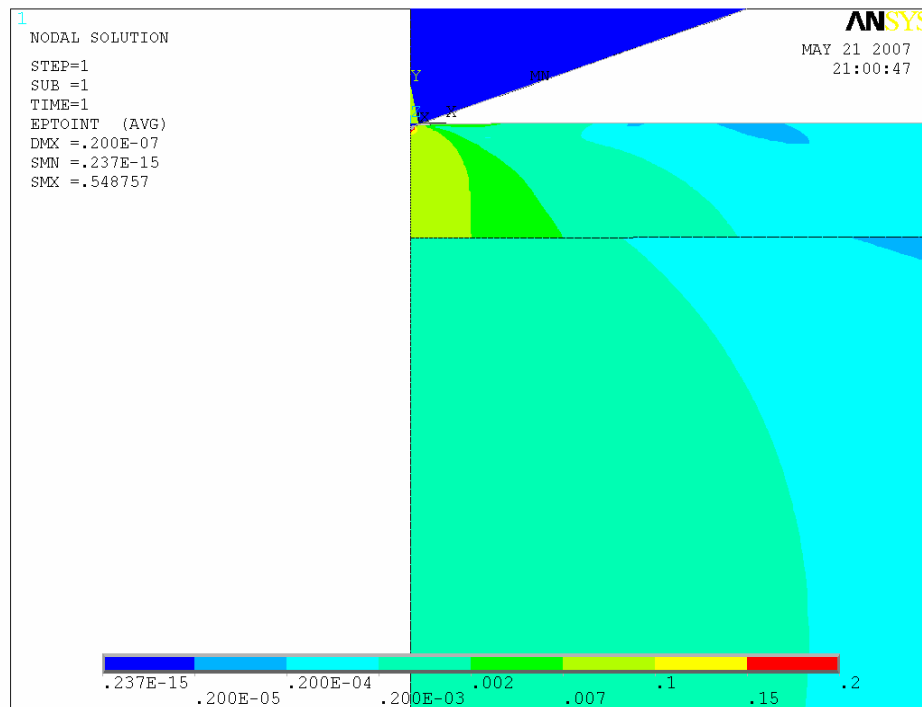


Figure 4.20b FEA result of indenting 20 nm into Si film on diamond substrate

Based on the simulation results of the inconsistent elastic strain growth in the film and substrate, the single alpha parameter in the Doerner & Nix function might not be sufficient enough to describe the whole situation. Thus, we suggested that there might be two parameters that control the weighting factors of the film and substrate separately. Eq. (19) is based on the compliance (form of reciprocal of the Young's modulus) of the specimen. Let us rearrange the equation again so that E is directly presented, and assume there are two parameters α_1 and α_2 in the function:

$$E = \frac{E'_f E'_s}{E'_f e^{-\alpha_1(t/h_c)} + E'_s [1 - e^{-\alpha_2(t/h_c)}]} \quad (20)$$

According to the equation above, $\exp(-\alpha_1 t/h_c)$ is the weighting factor that determines the contribution of the film part to the composite modulus, while $[1 - \exp(-\alpha_2 t/h_c)]$ represents the substrate's fraction. In applying the experimental data to Eq. (20), the results were very satisfying. It was found that, if fixing α_2 as a constant of 0.27~0.29, α_1 would also result in a constant value. Figure 4.21 shows the curve of α_1 vs. displacement (h) for SiO₂ (when $\alpha_2=0.27$) contrasted with the old alpha from the Doerner & Nix function. A list of the α_1 and α_2 values for each thin film system is shown in table 4.3. Using the values from table 4.3, the new function (Eq. 20) was found to be adept at closely matching most experimental data collected, which spanned both soft films on hard substrates and hard films on soft substrates. The experimental $E-h$ data were compared with the repression curves from the Doerner & Nix function, Gao's function, and Eq. (20) in Figure 4.22 through 4.34.

It is very interesting to see that the constant α_2 , which controls the substrate weighting factor, is equal to the Poisson's ratio of $\langle 100 \rangle$ Si (0.28). As the Si wafers are not always perfectly oriented to (100), it is reasonable to have a variation between 0.27~0.29 for the Si substrates used in this research. According to the data in table 4.3, the constant α_1 , on the other hand, is very close to the Poisson's ratio of the film. Is it true that α_1 and α_2 are actually the film and substrate Poisson's ratio? An analytical approach was introduced in the next section to relate these parameters.

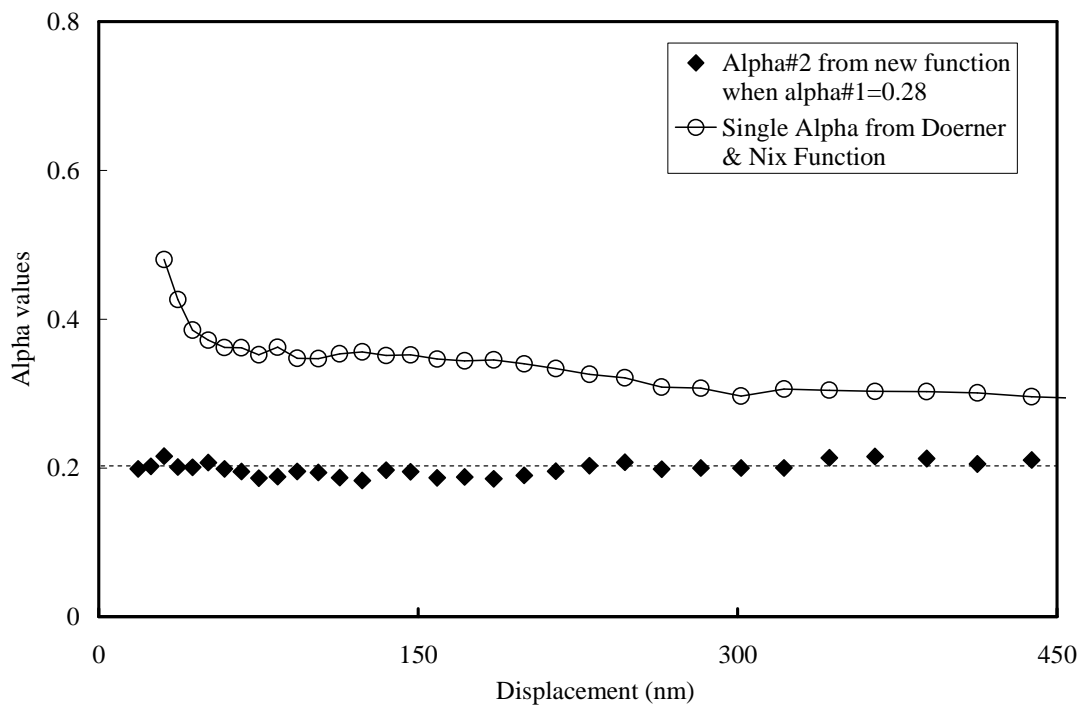


Figure 4.21 Comparison of α_1 - h data for SiO_2 with the Doerner & Nix function

Table 4.3 List of the α_1 and α_2 values for each thin film with the film Poisson's ratio

Thin films	Alpha#2 (α_2)	Alpha#1 (α_1)	Film Poisson's ratio
Polymer	0.28	0.45	0.45 [112]
NFC	0.27	0.33	0.33 [113]
CrO _x	0.28	0.27	0.25 [114]
SiO ₂	0.27	0.2	0.17 (quartz) [115]
FeO _x	0.28	0.35	N/A
TiO _x	0.27	0.28	0.28 [116]
a-Si	0.28	0.25	0.25 [117]
AlO _x	0.29	0.27	0.27 [116]
AlN	0.28	0.27	0.25 (crystal) [118]
FeB	0.27	0.25	0.25 [119]
Metglas	0.28	0.31	0.33 [120]
SiN _x	0.28	0.3	0.28 (crystal) [116]
SiC	0.28	0.3	0.22 ± 0.27 [121]
ta-C:H	0.28	0.28	0.28 [122]
UNCD	0.28	0.1	0.07 [29]

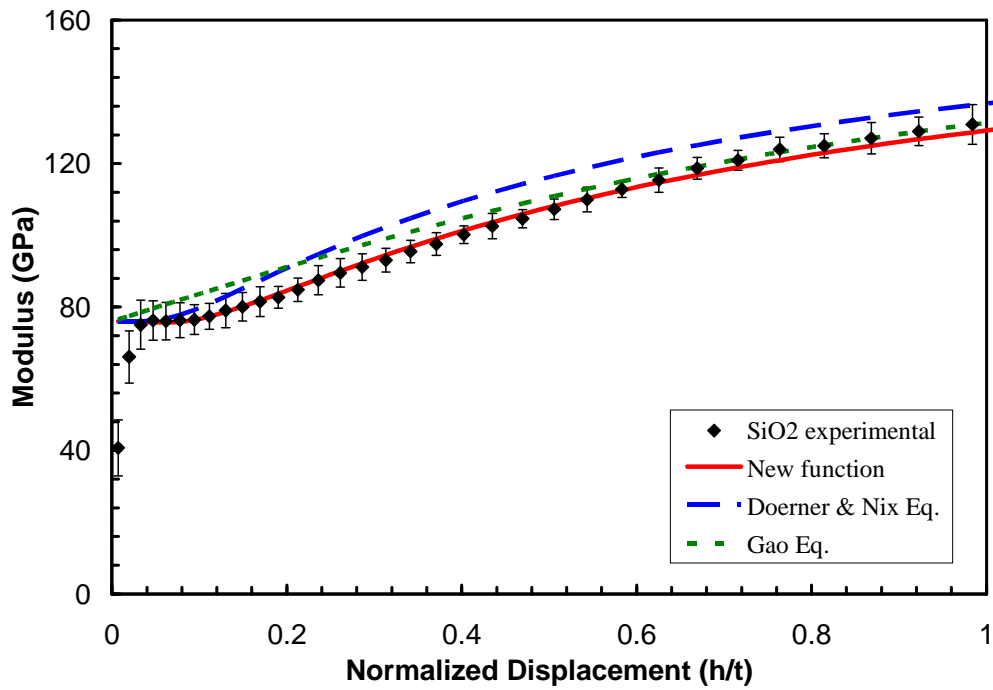


Figure 4.22 $E-h$ curve of SiO_2 film with the new, Doerner & Nix, and Gao models.

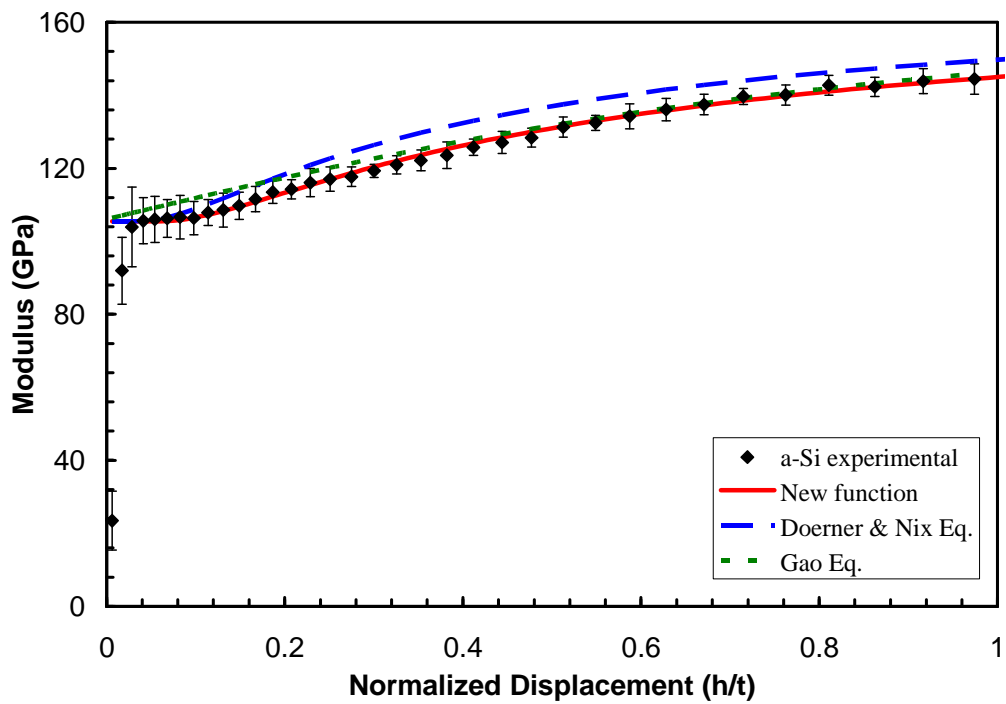


Figure 4.23 $E-h$ curve of a-Si film with the new, Doerner & Nix, and Gao models.

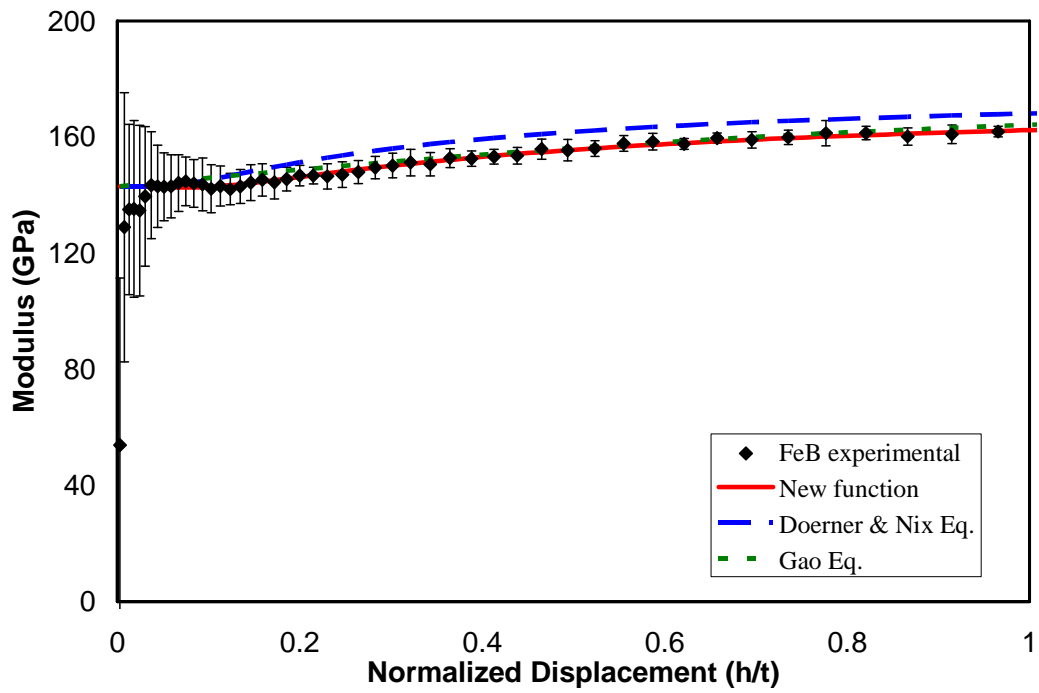


Figure 4.24 $E-h$ curve of FeB film with the new, Doerner & Nix, and Gao models.

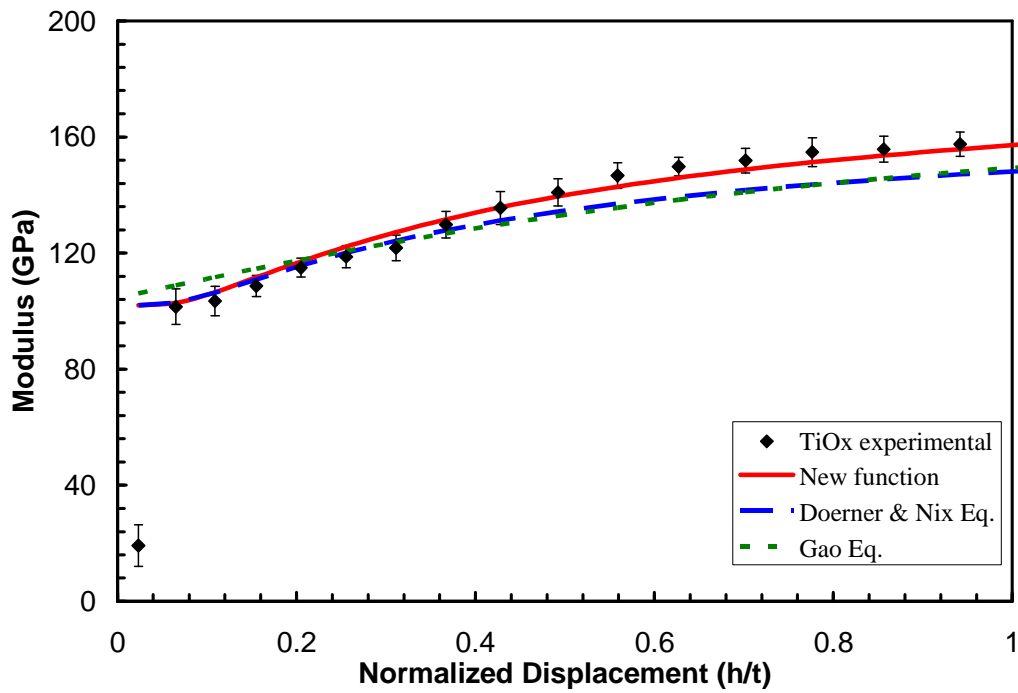


Figure 4.25 $E-h$ curve of TiO_x film with the new, Doerner & Nix, and Gao models.

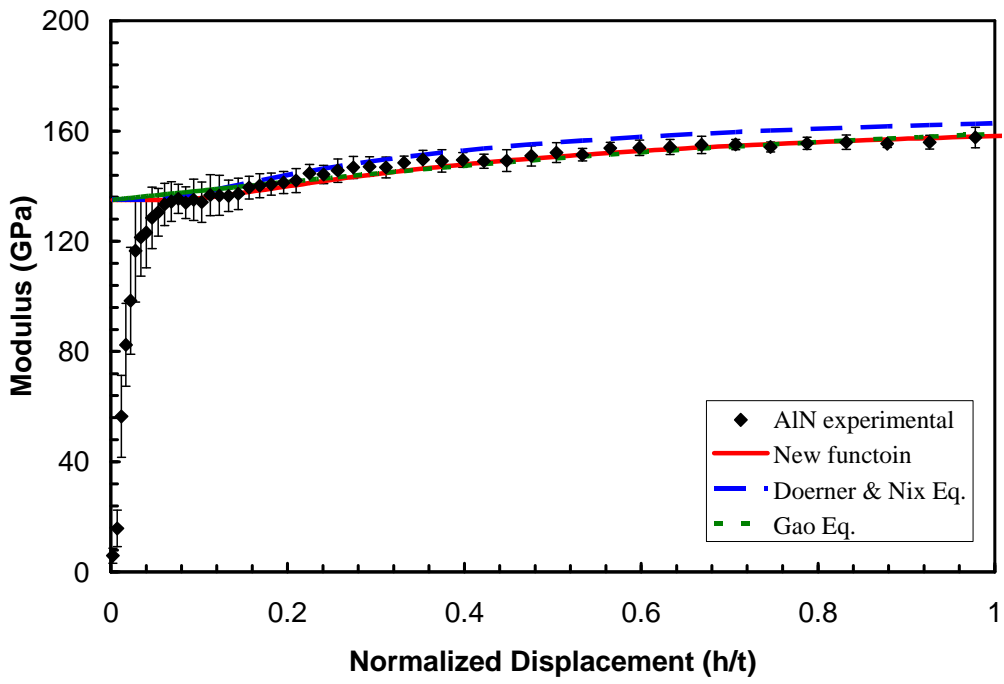


Figure 4.26 $E-h$ curve of AlN film with the new, Doerner & Nix, and Gao models.

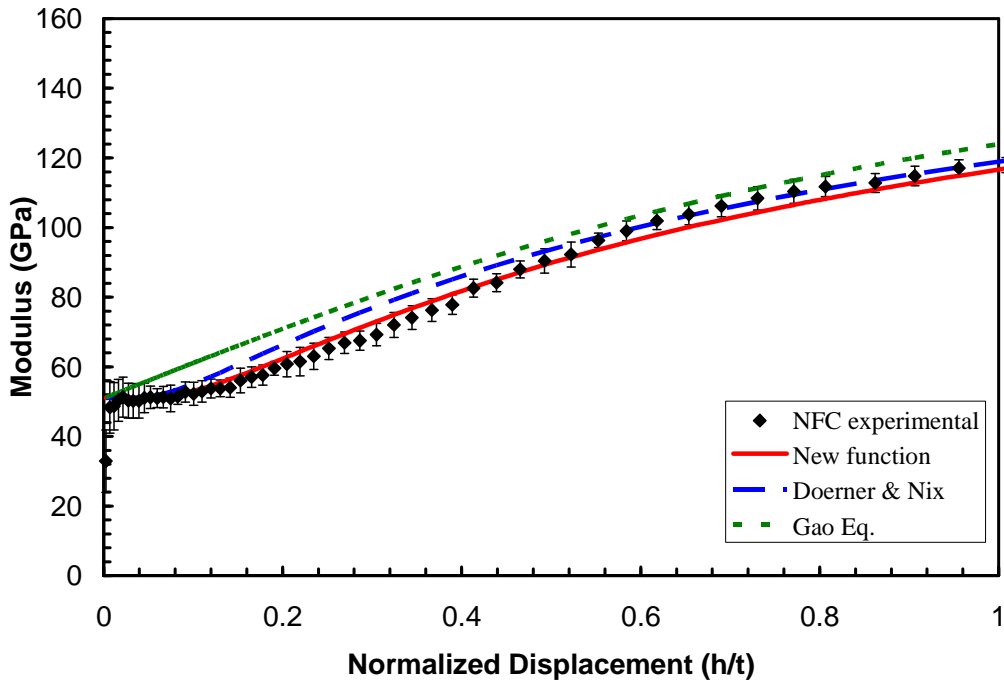


Figure 4.27 $E-h$ curve of NFC film with the new, Doerner & Nix, and Gao models.

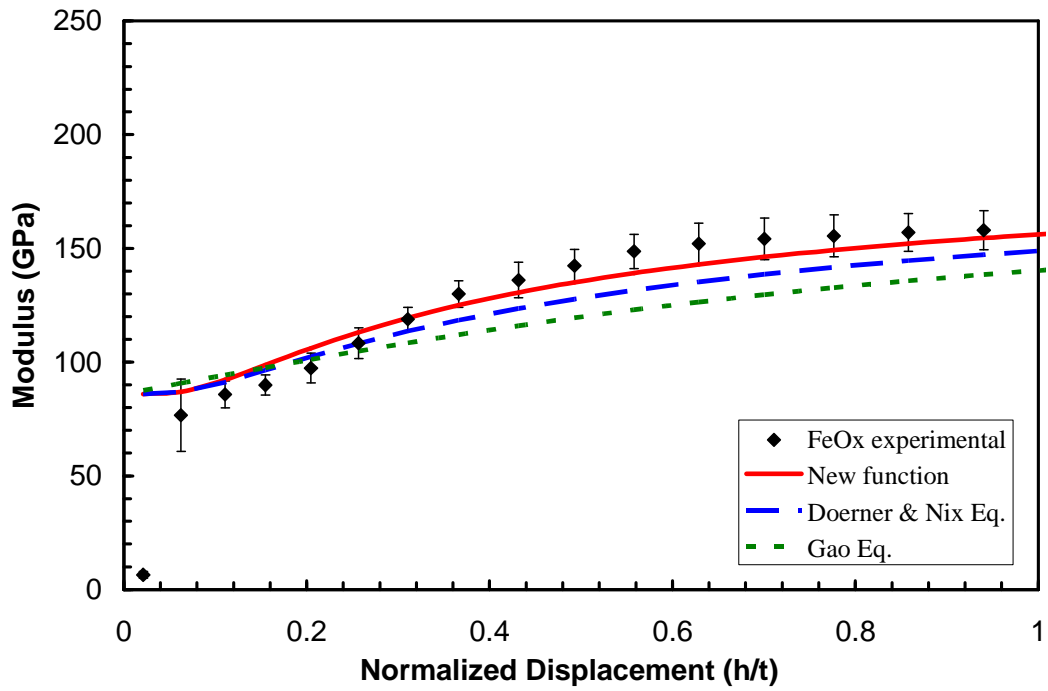


Figure 4.28 $E-h$ curve of FeO_x film with the new, Doerner & Nix, and Gao models.

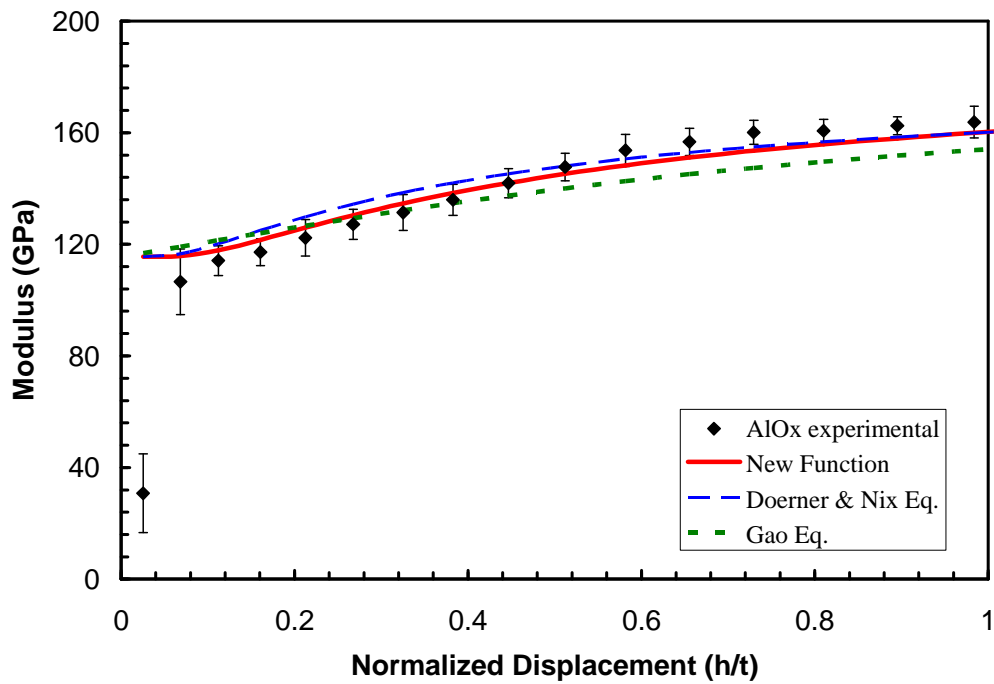


Figure 4.29 $E-h$ curve of AlO_x film with the new, Doerner & Nix, and Gao models.

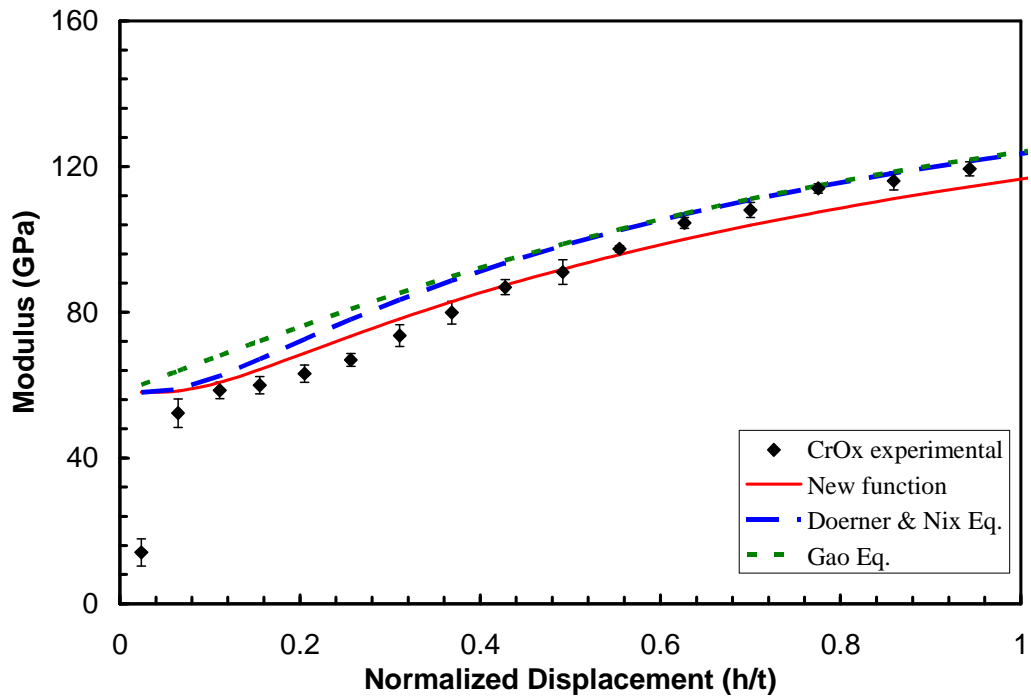


Figure 4.30 $E-h$ curve of CrO_x film with the new, Doerner & Nix, and Gao models.

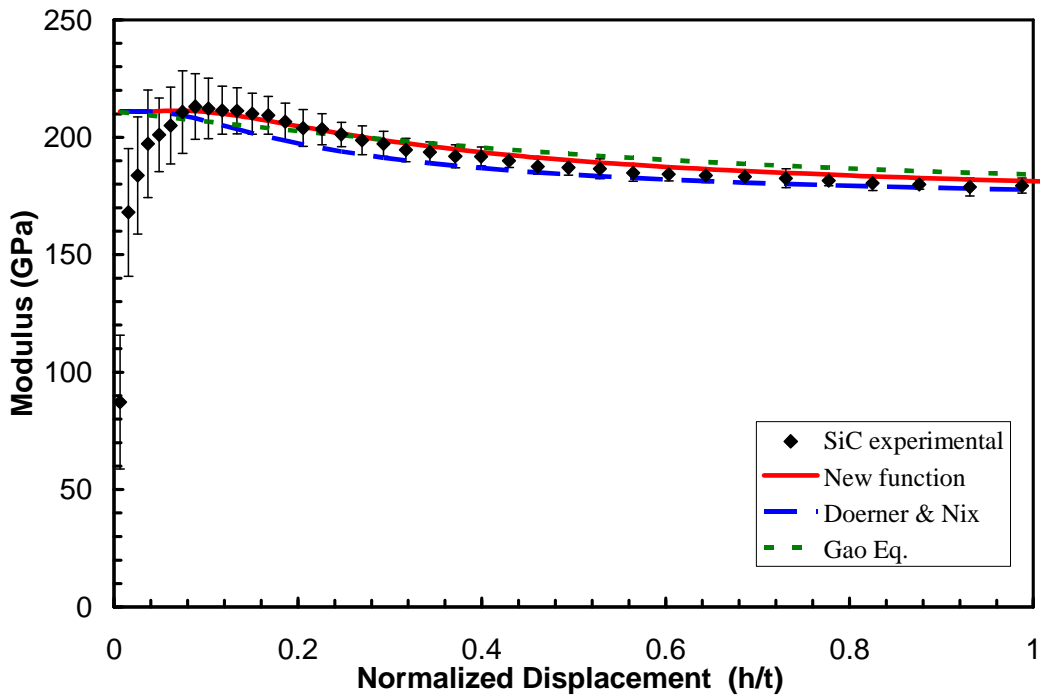


Figure 4.31 $E-h$ curve of SiC film with the new, Doerner & Nix, and Gao models.

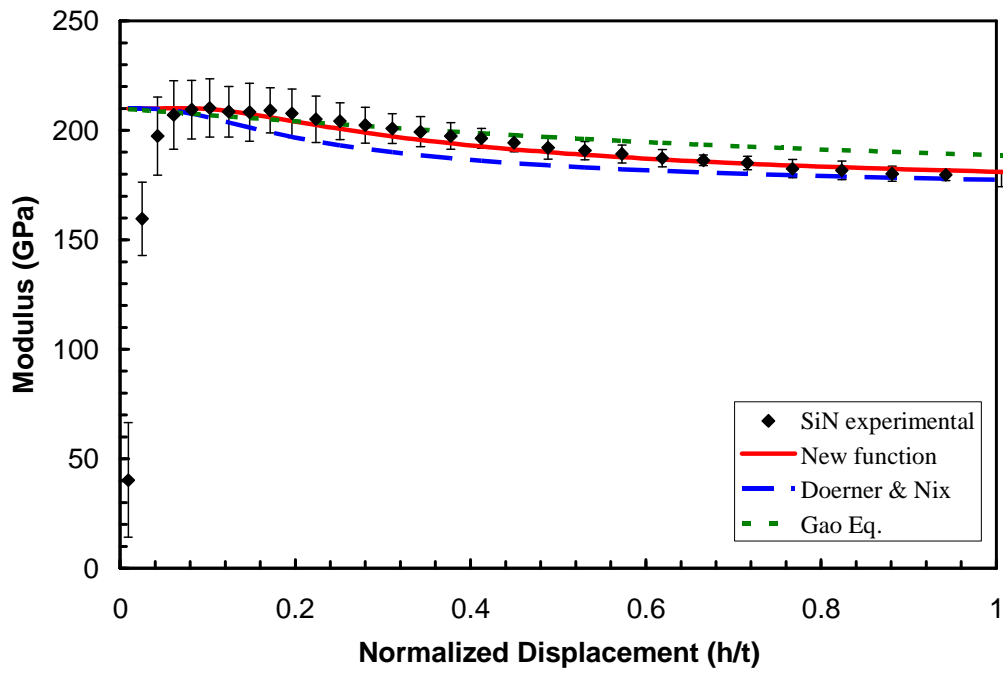


Figure 4.32 $E-h$ curve of Si_3N_4 film with the new, Doerner & Nix, and Gao models.

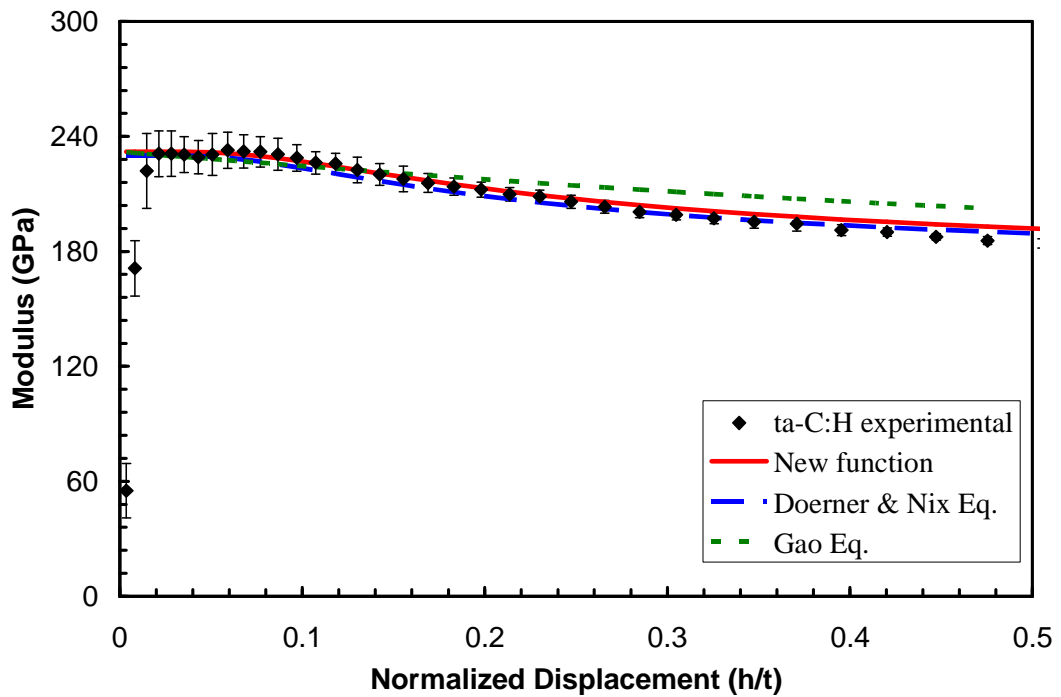


Figure 4.33 $E-h$ curve of ta-C:H film with the new, Doerner & Nix, and Gao models.

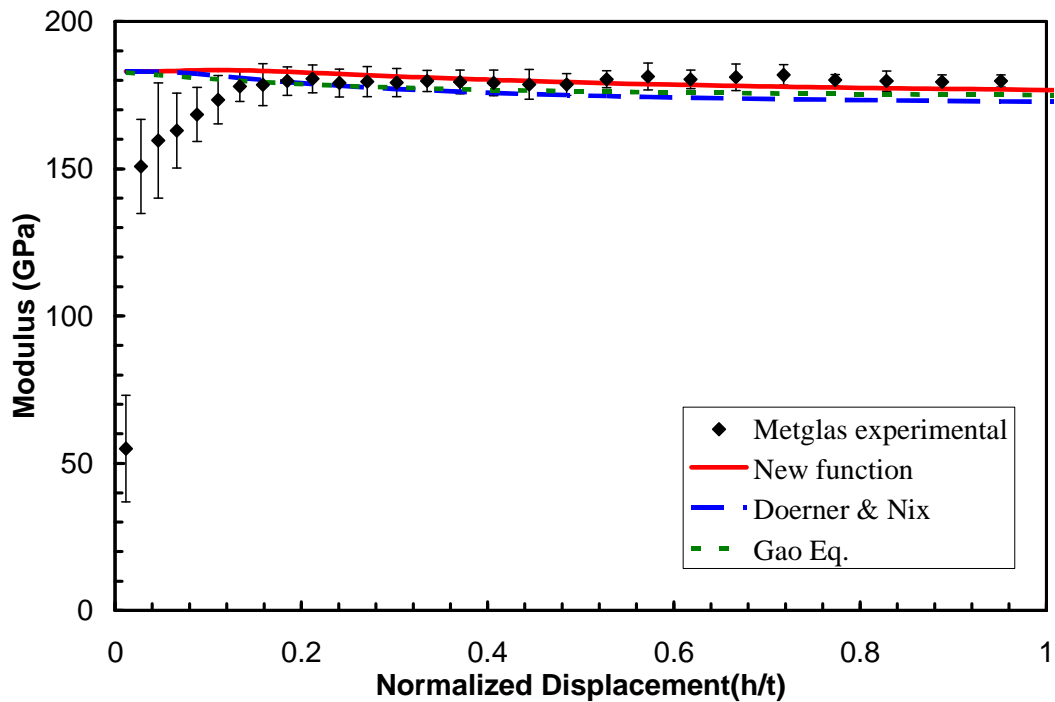


Figure 4.34 $E-h$ curve of Metglas film with the new, Doerner & Nix, and Gao models.

There are two films that didn't match well with the two-alpha function: Polymer and nanocrystalline diamond (UNCD) as shown in figure 4.35a and 4.35b. The deposition method for the polymer was layer-by-layer. Since it is not a continuous deposition method, it is possible that the polymer film is not as uniform as other amorphous materials. As there is an interface between each layer of the polymer, penetration from one layer to the next needs extra load (energy) due to the existence of the residual stress [47]. This may be the reason why the $E-h$ curve in figure 4.36a increases faster than expected. However, the new function is still doing an excellent job for matching the experimental data in the early stage of indentation.

The error in nanocrystalline diamond data is caused by another mechanism. Based on Knapp's simulation results [72], nanoindentation on diamond film results in

serious sink-in situation, whose degree is much larger than that the Oliver & Pharr method suggests. A unique technique for measuring the UNCD modulus was by Espinosa, Prorok and co-workers [62,73-76,78-80]. The so-called membrane deflection technique (MDE) employs tests on freestanding structures of the diamond film. Without having a substrate (effect), the Young's modulus of UNCE was accurately measured as 960 GPa. This value is almost 40% larger than that obtained from the regular nanoindentation test. Due to the serious sink-in degree, the measured modulus was greatly underestimated even from the beginning of indentation. This is the reason why UNCE E-h curve never reaches the true film value in figure 4.36b. Besides, the diamond film has nanocrystalline structures, which might also affect the nanoindentation data due to the existence of small grain structures. Both of these mechanisms limit the use of the new function in UNCD specimens.

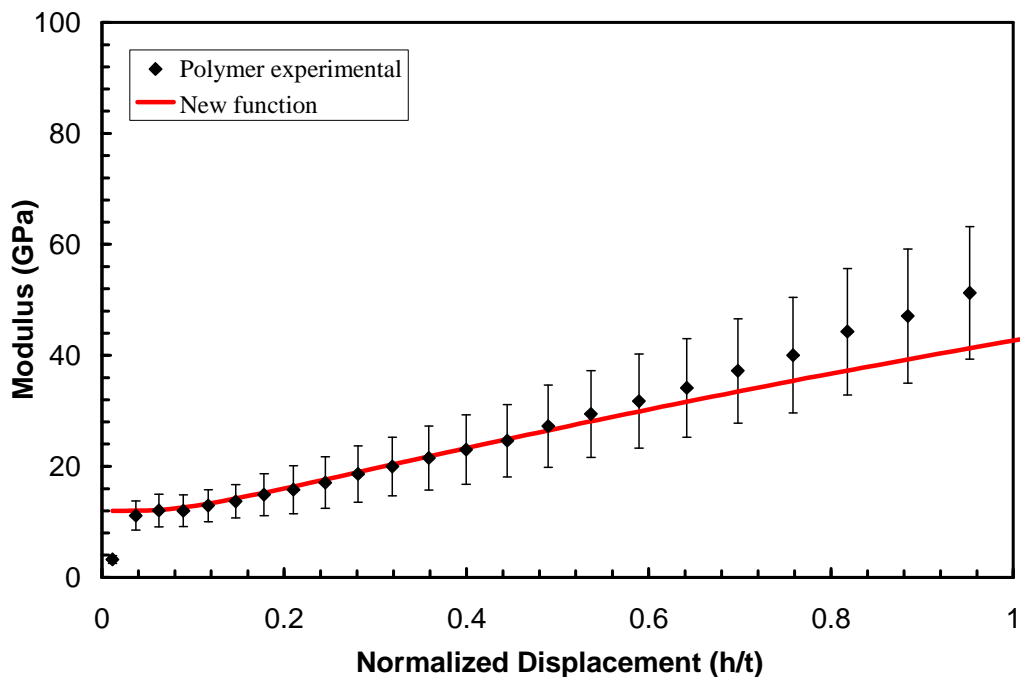


Figure 4.35a *E-h* curve of polymer film with the new two-alpha model.

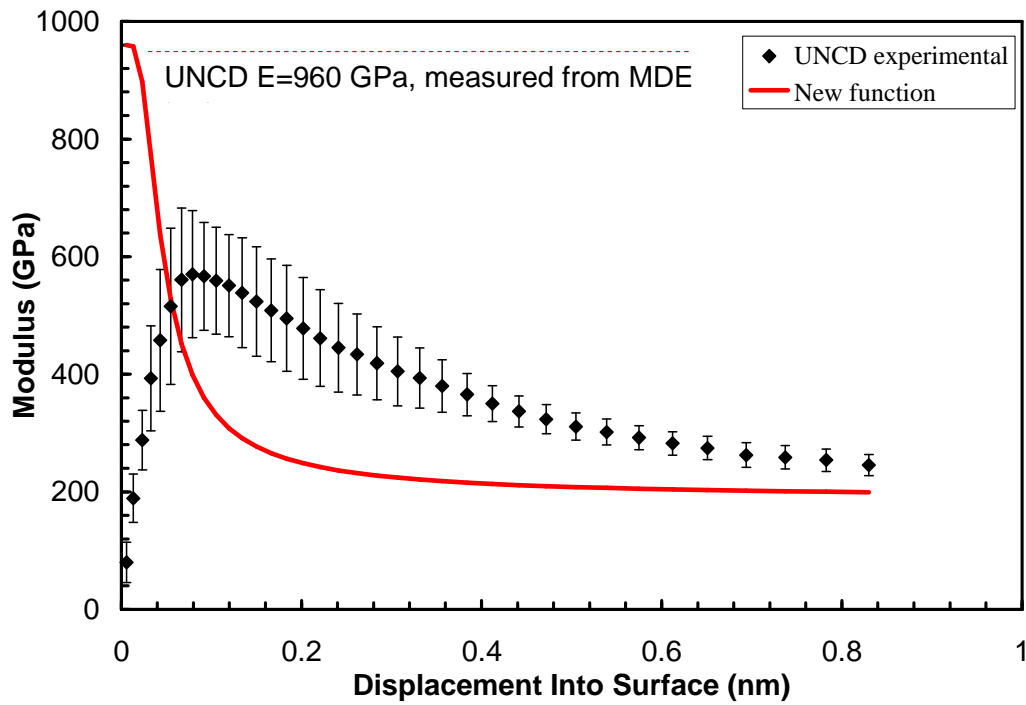


Figure 4.35b $E-h$ curve of UNCD film with the new two-alpha model

4.6 Physical explanation of α_1 and α_2 in modified Doerner & Nix function

The physical meaning behind α_1 and α_2 needs to be found to leverage the empirical function to theoretical level. In this section, a mathematical approach was employed to better understand the physical meaning behind the Doerner & Nix function and the parameter α . As mentioned in Chapter 2, Gao's analytical function for thin film indentation was derived from considering the energy transformation from indenter to the specimen. Thus, Gao's weighting factor gives the ratio of the strain energy stored in the film to the total energy stored in the specimen. Doerner & Nix weighting factor resembles the shape of Gao's factor, which suggests that it is also a ratio of strain energy distribution. As mentioned above, Doerner & Nix function describes a consistent change of the elastic strain intensity distribution in film and

substrate. Assuming the total elastic strain energy in the specimen is confined in an “effective” volume with uniform energy density, Doerner & Nix weighting factor can be seen as a ratio of the segment in the film to the total volume. According to the shape of elastic strain region in finite element analysis, also to simplify the mathematical model, the volume is assumed to have a spherical shape. As shown in figure 4.36, the film segment of the spherical volume always has a vertical length of t , which is the film thickness. The radius of the effective energy volume (R) increases with the displacement (h) as the indenter goes deeper into the specimen.

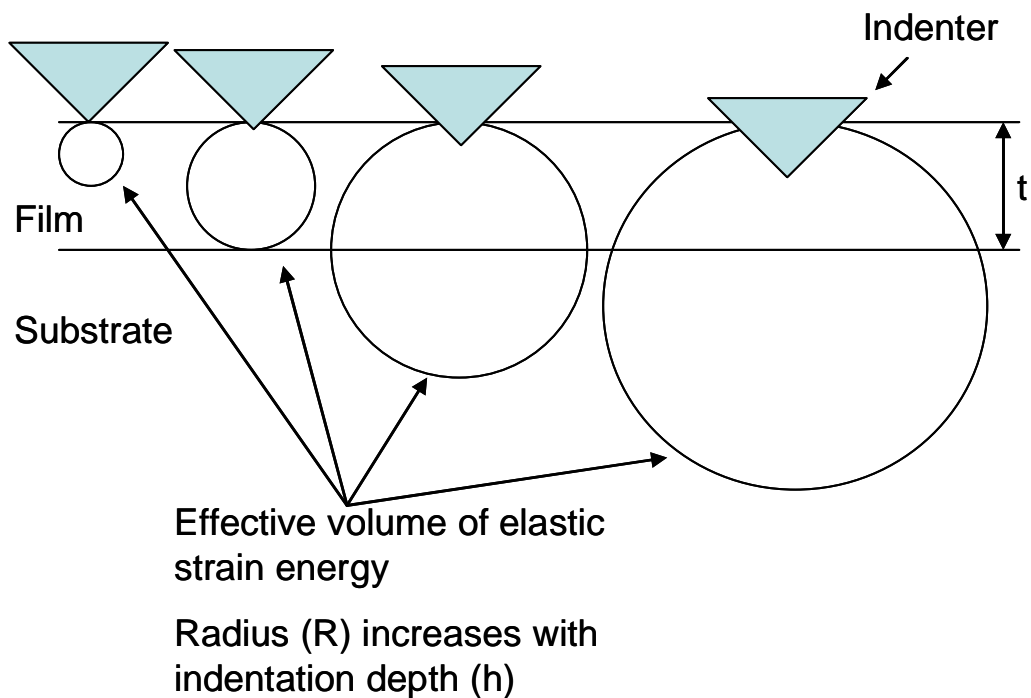


Figure 4.36 Effective elastic strain energy volume developed during nanoindentation

The formula for the volume of a spherical segment is shown in Eq. (21) according to figure 4.37:

$$V_{cap} = \frac{\pi}{3} x^2 (3R - x) \quad (21)$$

As the volume for a sphere is equal to $(4/3)\pi R^3$, the sphere segment ratio can be represented as:

$$\frac{V_{cap}}{V_{total}} = \frac{\frac{\pi}{3} x^2 (3R - x)}{\frac{4}{3} \pi R^3} = \frac{3}{4} \left(\frac{x}{R} \right)^2 - \frac{1}{4} \left(\frac{x}{R} \right)^3 \quad (22)$$

For thin film indentation, x =film thickness (t), and R is a function of indentation depth (h). $\Psi=[1-V_{cap}/V_{total}]$ should resemble the Doerner & Nix factor [$exp^{-at/h}$], if correct R function is suggested.

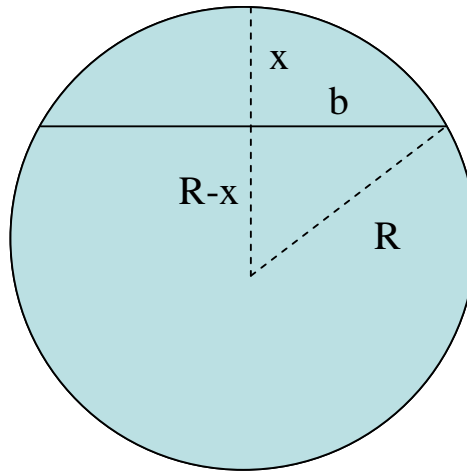


Figure 4.37 Important parameters for the spherical segment

Mathematical approach has been performed to obtain the most suitable radius function. It was found that a simple linear relation between R and h fitted best with the Doerner & Nix factor:

$$R = K * h + \frac{t}{2} \quad (23)$$

where K is a constant and the Y-intercept equals half of the film thickness. Substituting the above equation into Eq. (22), the energy fraction coefficient is plotted in figure 4.38a with the Doerner & Nix factor ($\alpha=0.25$) for indentation on a 500nm thick film. The two factors are in good agreement. Now let's see how the alpha parameter influences R in Eq. (22) and (23). Changing α from 0.25 to 0.05 (figure 4.38b) results in a sharp increase of the Doerner & Nix factor. As mentioned in section 4.3, a smaller α yields a greater substrate effect. To match with this trend, R in Eq. (23) must be increased to account for more volume in the substrate for the rising substrate effect. From figure 4.38a to 4.38b, K in Eq. (23) increased from 1.2 to 5.5. In applying a 10nm indentation depth in a 500nm film, R and K for different α values are listed in table 4.4. It was found that α has a linear relation with $1/K$, see figure 4.39. Also R decreases non-linearly with increasing α (figure 4.40).

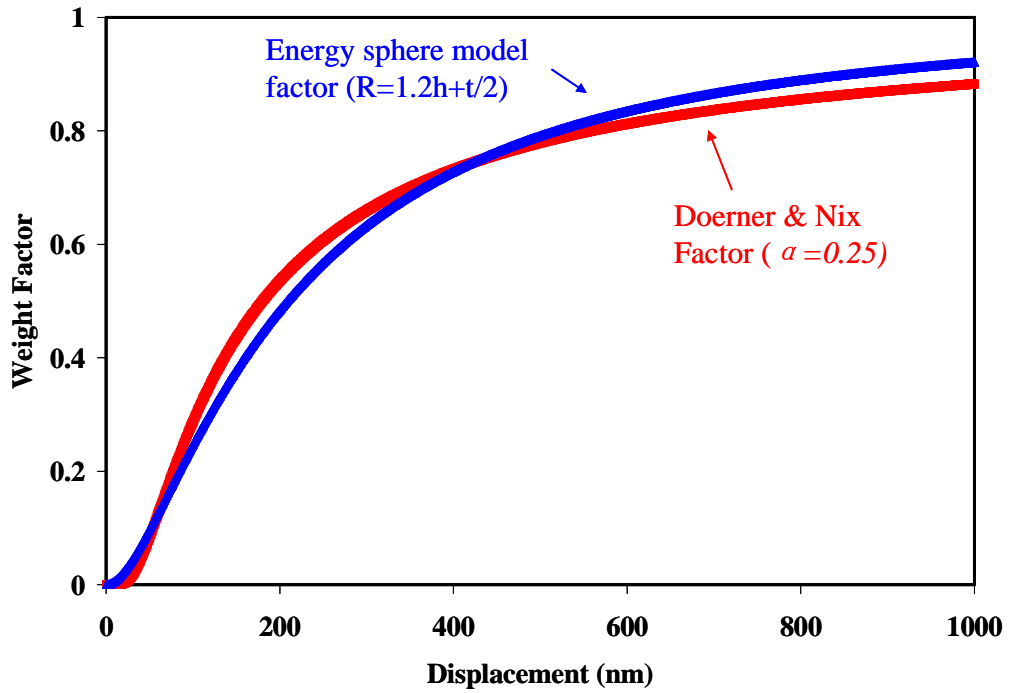


Figure 4.38a Comparison of the Doerner & Nix factor ($\alpha=0.25$) and the analytical model from Eq. (22).

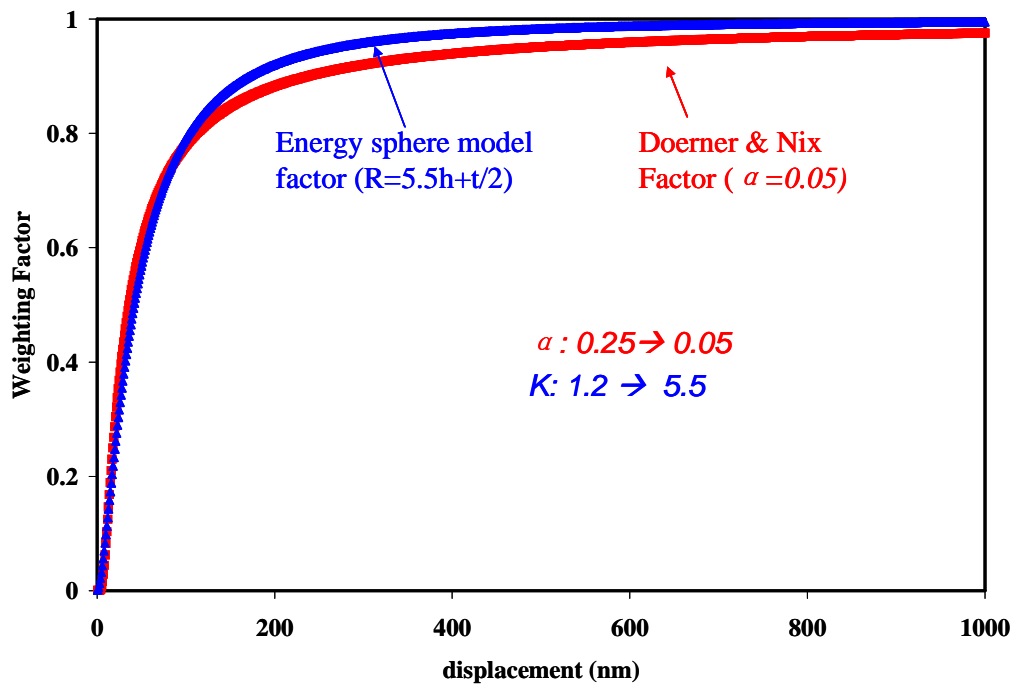


Figure 4.38b Comparison of the Doerner & Nix factor ($\alpha=0.05$) and the analytical model from Eq. (22).

Table 4.4 α parameter in Doerner & Nix function and corresponding K and R values
in the analytical model from Eq. (22) when indenting 10 nm into a 500nm film

Alpha (α)	K	1/K	R
0.05	5.52	0.18	305
0.1	3.01	0.33	280
0.15	2.01	0.5	270
0.2	1.50	0.67	265
0.25	1.21	0.83	262
0.3	1.07	0.95	260.5
0.35	.93	1.11	259
0.4	0.82	1.25	258
0.45	0.71	1.41	257.2
0.499	0.66	1.53	256.5

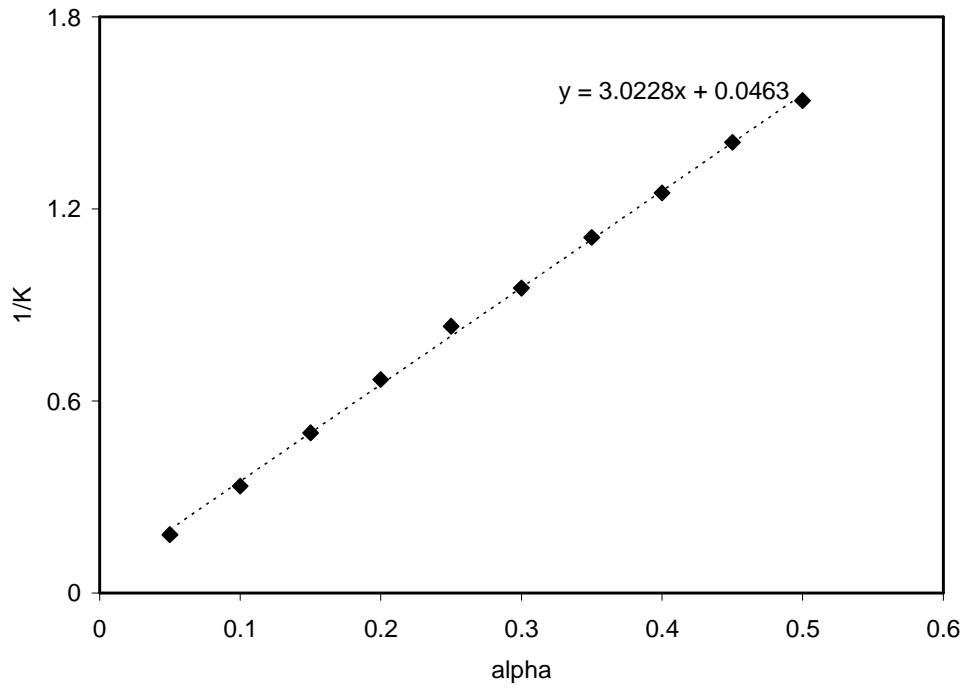


Figure 4.39a Plot of $1/K$ vs. α for a 10 nm indentation on a 500nm film

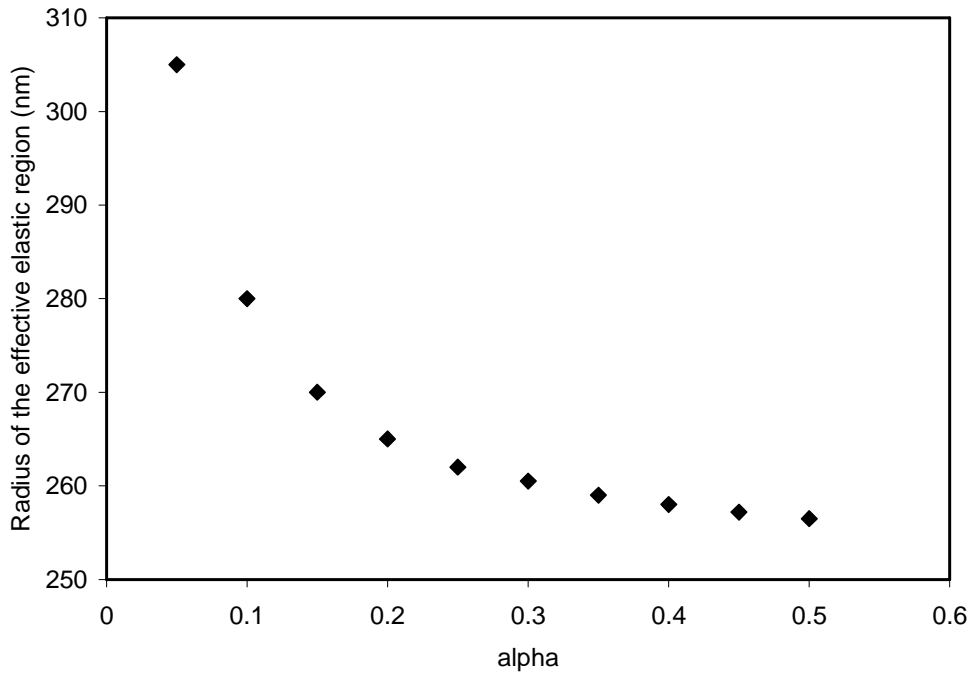


Figure 4.39b Plot of R in Eq. (23) vs. α for a 10 nm indentation on a 500nm film

The section above has shown the Doerner & Nix function can be related to the strain energy volume model. However, the increasing trend of the volume radius with decreasing α does not match the real situation. The major drawback is from the assumption of continuous elastic strain growth through the specimen. Considering that there are two parameters that specify the film and substrate elastic strain growth respectively, the strain volume radius in the film (R_f) should not match with that in the substrate (R_s). Figure 4.41 shows the different changing ways of R between single alpha (α) and two parameters situation to achieve the same volume ratio increase.

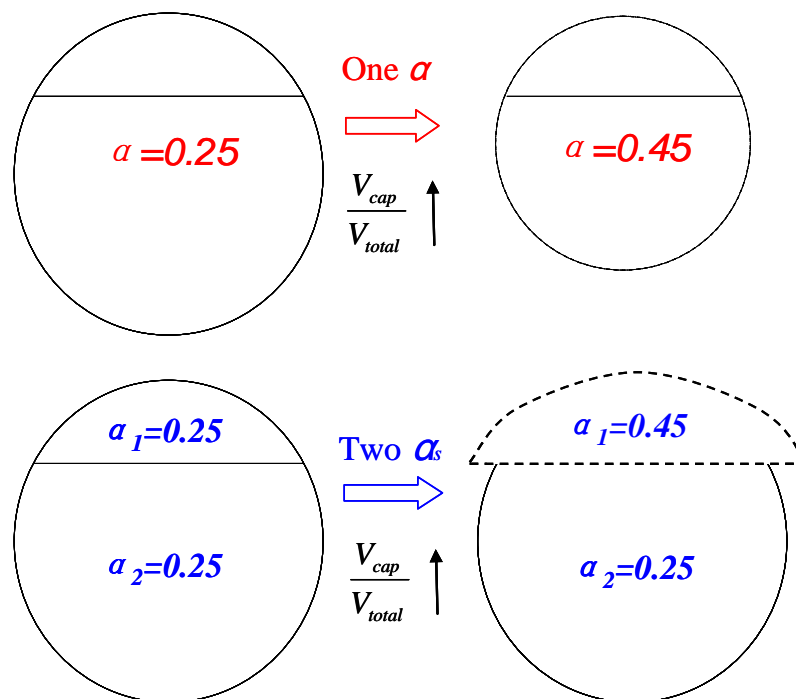


Figure 4.40 Comparison between 1- α and 2- α models

As the specimens all have Si as substrates, let us fix α_2 and see how α_1 affects the radius change in the film. In applying Equation (24), R_f was calculated and plotted with corresponding α_1 in figure 4.41. It is found R_f increases with α_1 with an opposite

trend from figure 4.39b for single alpha factor.

$$\frac{V_{cap}}{V_{total}} = \frac{\frac{\pi}{3}t^2(3R_f - t)}{[\frac{4}{3}\pi R_s^3 - \frac{\pi}{3}t^2(3R_s - t) + \frac{\pi}{3}t^2(3R_f - t)]} \quad (24)$$

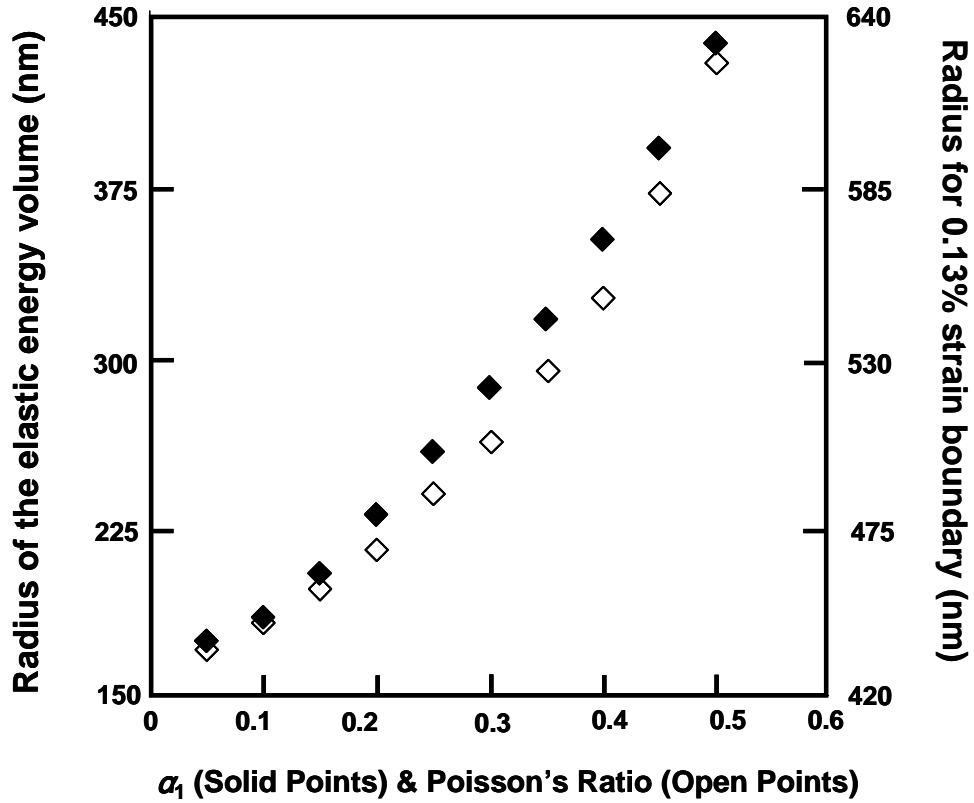


Figure 4.41 Radius of the elastic strain boundary vs. α_1 & Poisson's Ratio

Now, if the film Poisson's ratio is equal to α_1 , it should manifest R_f in a same way as shown in figure 4.41. First, it is necessary to investigate how the Poisson' ratio affects the elastic strain energy in the specimen. As the indenter is driven into the film, local material is pushed away both vertically and laterally (figure 4.42). The laterally displaced film is mainly controlled by the shear mechanisms. The film shear modulus can be represented as:

$$G = \frac{\tau_{xy}}{\gamma_{xy}} = \frac{E}{2(1+\nu)} \quad (25)$$

Assuming indentation is performed on two films with similar Young's modulus but different Poisson's ratio (i.e, $\nu_1=0.1$, and $\nu_2=0.3$). According to Eq. (25), the one with smaller Poisson's ratio should have larger shear modulus and thus be more difficult to deform laterally.

According to that, the elastic strain boundary (volume) should be lesser for a material with smaller Poisson's Ratio. The finite element analysis results proved this assumption. Figure 4.43 shows 10 nm indentations on 500 nm NFC film with the same Young's Modulus and same Si substrates but different Poisson's Ratio. From 4.43(a) to 4.43(c), it is clear to see the film elastic strain boundary at the interface grows with the change of Poisson's Ratio. Using the equation below from figure 4.37 to calculate the effective radius of the total elastic energy volume [R in Eq. (22)]:

$$R = \frac{b^2 + x^2}{2x} \quad (26)$$

The R_f -Poisson's ratio (ν) curve is also plotted in figure 4.41 for comparison and contrast. Although the absolute values of these two curves are not the same (because the elastic strain boundary was randomly picked-up, which may not resemble the true radius of the effective elastic energy volume), it was found that alpha and Poisson's ratio manifested R in a same manner. Based on this mathematical approach and the matching experimental data, we suggest that the

two constants in the modified Doerner & Nix function are film and substrate Poisson's ratios.

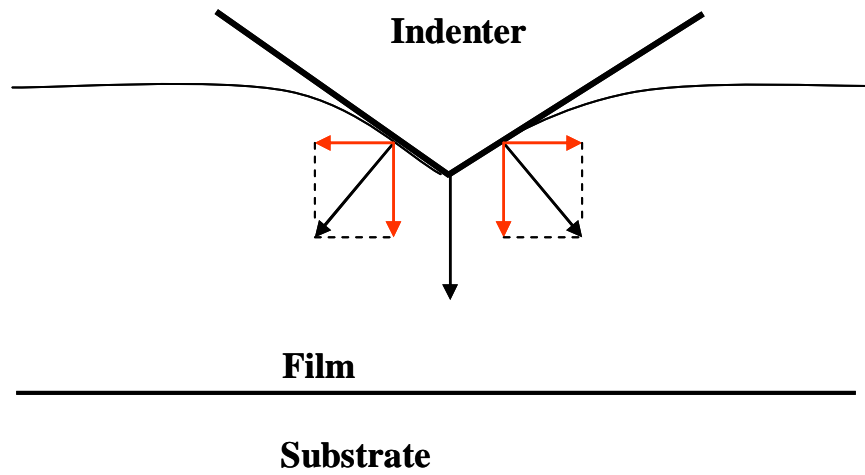


Figure 4.42 Schematic of an indentation impression in the film

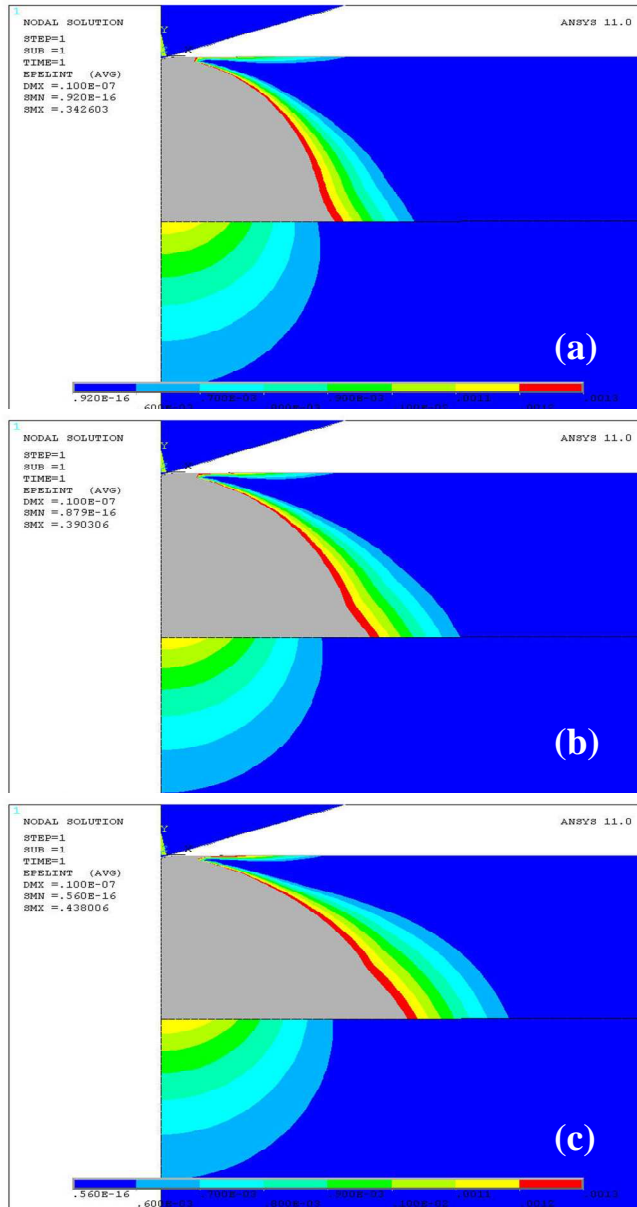


Figure 4.43 FEA elastic strain distributions in the films with the same Young's modulus but different Poisson's Ratios: (a) $\nu=0.1$, (b) $\nu=0.3$, (c) $\nu=0.49$

CHAPTER 5

CONCLUSIONS

In this study, 15 specimens were tested with continuous stiffness nanoindentation to investigate the origin of the substrate effects and its relation to the elastic strain properties in the film and substrate. 14 of them were deposited as amorphous films so that the film microstructures effects on nanoindentation could be minimized. Another tested material was ultra-nanocrystalline diamond film. It was found that as long as the indentation depth was within the film, pile-up degree was negligible and only had minor effects on measure Young's modulus. The films were characterized with XRD, SEM, AFM and other systems before indentation data collection.

Two existing models for the thin film nanoindentation mechanism: Doerner & Nix and Gao models, were studied and compared with our experimental data. It was found that the Doerner & Nix function always yielded more satisfying results for those films that had a flat region in the early stage of the $E-h$ curve, while Gao's model always fit well with the material whose Young's modulus increased (or decreased) from the beginning of the indentation. Since most of our experimental curves had flat regions, the study was mainly focused on modifying Doerner & Nix function.

The flat region length or the critical indent depth (h_{cr}) was determined for each material. A unique non-linear trend was found between the critical indent depth/film thickness ratio and film/substrate modulus ratio. It was also found that the thickness would not affect the h_{cr}/t as long as E_f/E_s was similar. The Doerner and Nix equation for substrate effects were investigated carefully in this study. It was found parameter α in the function was not a constant as originally suggested. It changed with the indentation depth. To improve Doerner & Nix function, two parameters were suggested in the equation instead of one. Based on the experimental determination and analytical modeling, the two parameters were suggested as the Poisson's ratio of the film and substrate. The modified function was found to better describe most of the tested materials.

REFERENCES

- [1] D. Tabor, Proc. R. Soc. **A(192)**, (1948), 247.
- [2] N. A. Stillwell and D. Tabor, Proc. R. Soc. **(78)**, (1961), 169.
- [3] H. Buckle, *The Science of Hardness Testing and its Research Applications*, American Society for Metals, Materials Park, Ohio, (1973)
- [4] S. I. Bulychev, V. P. Alekhin, M. K. Shorshorov, A. P. Ternovskii and G. D. Shnyrev, *Determination of Young's modulus according to the indentation diagram*, Industrial Lab **41**, (1975), 1409.
- [5] F. Frohlich, P. Grau and W. Grellmann, *Performance and Analysis of Recording Microhardness Tests*, Phys. Status Solidi (a **42**, (1977), 79?9.
- [6] D. Newey, M. A. Wilkens and H. M. Pollock, *An uhra-low-load penetration hardness tester [J]*, Phys E: Sci Instrum **15(1)**, (1982), 119-122.
- [7] M. K. Shorshorov, S. I. Bulychev and V. P. Alekhin, *Work of Plastic Deformation during Indenter Indentation*, Sov. Phys. Dokl **26(8)**, (1982), 769?71.
- [8] J. B. Pethica, R. Hutchings and W. C. Oliver, Philos. Mag. **A(48)**, (1983), 593.
- [9] J. L. Loubet, J. M. Georges, O. Marchesini and G. Meille, *Vickers indentation curves of magnesium oxide(MgO)*, Journal of lubrication technology **106(1)**, (1984), 43-48.
- [10] M. F. Doerner and W. D. Nix, *A method for interpreting the data from*

- depth-sensing indentation instruments*, J. Mater. Res **1(4)**, (1986), 601-609.
- [11] W. C. Oliver, MRS Bull. **11**, (1986), 15-19.
- [12] H. M. Pollock, D. Maugis and M. Barquins, *Microindentation Techniques in Material Science and Engineering*, ASTM STP **889**, (1986), 47-71.
- [13] R. B. King, *Elastic Analysis of Some Punch Problems for a Layered Medium* (IBM Thomas J. Watson Research Center, 1987).
- [14] M. J. Mayo, R. W. Siegel, A. Narayanasamy and W. D. Nix, *MECHANICAL PROPERTIES OF NANOPHASE TiO₂ AS DETERMINED BY NANOINDENTATION*, Journal of Materials Research **5(5)**, (1990), 1073-1082.
- [15] H. Gao, C. H. Chiu and J. Lee, Int. J. Solids Structures **29**, (1992)
- [16] W. C. Oliver and G. M. Pharr, *IMPROVED TECHNIQUE FOR DETERMINING HARDNESS AND ELASTIC MODULUS USING LOAD AND DISPLACEMENT SENSING INDENTATION EXPERIMENTS*, Journal of Materials Research **7(6)**, (1992), 1564-1583.
- [17] N. G. Chechenin, J. Brttiger and J. P. Krog, *Nanoindentation of amorphous aluminum oxide films I. The influence of the substrate on the plastic properties*, Thin Solid Films **261(1-2)**, (1995), 219-227.
- [18] G. M. Pharr, D. L. Callahan, S. D. McAdams, T. Y. Tsui, S. Anders, et.al, *Hardness, elastic modulus, and structure of very hard carbon films produced by cathodic-arc deposition with substrate pulse biasing*, Applied Physics Letters **68**, (1996), 779.

- [19] T. Y. Tsui, W. C. Oliver and G. M. Pharr, *Influences of stress on the measurement of mechanical properties using nanoindentation: Part I. Experimental studies in an aluminum alloy*, J. Mater. Res **11(3)**, (1996), 752-759.
- [20] X. Li, D. Diao and B. Bhushan, *Fracture mechanisms of thin amorphous carbon films in nanoindentation*, Acta Materialia **45(11)**, (1997), 4453-4461.
- [21] J. Mencik, D. Munz, E. Quandt, E. R. Weppelmann and M. V. Swain, *Determination of elastic modulus of thin layers using nanoindentation*, J. Mater. Res **1997**, (1997)
- [22] W. D. Nix, *Elastic and plastic properties of thin films on substrates: nanoindentation techniques*, Materials science & engineering. A, Structural materials: properties, microstructure and processing **234**, (1997), 37-44.
- [23] J. Y. Rho, T. Y. Tsui and G. M. Pharr, *Elastic properties of human cortical and trabecular lamellar bone measured by nanoindentation*, Biomaterials **18(20)**, (1997), 1325-1330.
- [24] J. Woirgard and J. C. Dargenton, *An alternative method for penetration depth determination in nanoindentation measurements*, J. Mater. Res **1997**, (1997)
- [25] G. M. Pharr, *Measurement of mechanical properties by ultra-low load indentation*, Mat. Sci. & Eng. **A(253)**, (1998), 151-159.
- [26] S. J. Cho, K. R. Lee, K. Y. Eun, J. H. Hahn and D. H. Ko, *Determination of elastic modulus and poisson's ratio of diamond-like carbon films*, Thin Solid Films **341(207)**, (1999), 210.

- [27] J. H. Ahn and D. Kwon, *Micromechanical estimation of composite hardness using nanoindentation technique for thin-film coated system*, Materials Science & Engineering A **285(1-2)**, (2000), 172-179.
- [28] A. Gouldstone, H. J. Koh, K. Y. Zeng, A. E. Giannakopoulos and S. Suresh, *Discrete and continuous deformation during nanoindentation of thin films*, Acta Materialia **48(9)**, (2000), 2277-2295.
- [29] J. L. Hay and G. M. Pharr, (ASM International, 2000).
- [30] N. X. Randall and A. Harris, *Nanoindentation as a tool for characterising the mechanical properties of tribological transfer films*, Wear **245(1-2)**, (2000), 196-203.
- [31] M. J. Bamber, K. E. Cooke, A. B. Mann and B. Derby, *Accurate determination of Young's modulus and Poisson's ratio of thin films by a combination of acoustic microscopy and nanoindentation*, Thin Solid Films **398**, (2001), 299-305.
- [32] M. Gen, R. Sakidja, W. D. Nix and J. H. Perepezko, *Microstructural mechanical properties and yield point effects in Mo alloys*, Materials Science & Engineering A **319**, (2001), 902-908.
- [33] Y. Huang, M. J. Aziz, J. W. Hutchinson, A. G. Evans, R. Saha, et.al, *Comparison of mechanical properties of Ni₃Al thin films in disordered FCC and ordered L1₂ phases*, Acta Materialia **49(14)**, (2001), 2853-2861.
- [34] R. Saha and W. D. Nix, *Soft films on hard substrates 梠anoindentation of tungsten films on sapphire substrates*, Materials Science & Engineering A **319**,

(2001), 898-901.

- [35] R. Saha, Z. Xue, Y. Huang and W. D. Nix, *Indentation of a soft metal film on a hard substrate: strain gradient hardening effects*, Journal of the Mechanics and Physics of Solids **49(9)**, (2001), 1997-2014.
- [36] J. G. Swadener, B. Taljat and G. M. Pharr, *Measurement of residual stress by load and depth sensing indentation with spherical indenters*, J. Mater. Res **16(7)**, (2001), 2092.
- [37] X. Li and B. Bhushan, *A review of nanoindentation continuous stiffness measurement technique and its applications*, Materials Characterization **48(1)**, (2002), 11-36.
- [38] D. Qian, G. J. Wagner, W. K. Liu, M. F. Yu and R. S. Ruoff, *Mechanics of carbon nanotubes*, Applied Mechanics Reviews **55**, (2002), 495.
- [39] R. Saha and W. D. Nix, *Effects of the substrate on the determination of thin film mechanical properties by nanoindentation*, Acta Materialia **50(1)**, (2002), 23-38.
- [40] T. Y. Zhang and W. H. Xu, *Surface effects on nanoindentation*, J. Mater. Res **17(7)**, (2002), 1716.
- [41] X. Huang and A. A. Pelegri, *Nanoindentation Measurements on Low-k Porous Silica Thin Films Spin Coated on Silicon Substrates*, Journal of Engineering Materials and Technology **125**, (2003), 361.
- [42] C. M. Lepienski and C. E. Foerster, *Nanomechanical Properties by Nanoindentation*, Encyclopedia of Nanoscience and Nanotechnology.

American Scientific Publishers, USA, (2003)

- [43] X. Li, H. Gao, C. J. Murphy and K. K. Caswell, *Nanoindentation of Silver Nanowires*, NANO LETTERS **3(11)**, (2003), 1495-1498.
- [44] E. T. Lilleodden, J. A. Zimmerman, S. M. Foiles and W. D. Nix, *Atomistic simulations of elastic deformation and dislocation nucleation during nanoindentation*, Journal of the Mechanics and Physics of Solids **51(5)**, (2003), 901-920.
- [45] M. A. Phillips, B. M. Clemens and W. D. Nix, *Microstructure and nanoindentation hardness of Al/Al₃Sc multilayers*, Acta Materialia **51(11)**, (2003), 3171-3184.
- [46] Z. Gan, Y. Zhang, G. Yu, C. M. Tan, S. P. Lau, et.al, *Intrinsic mechanical properties of diamond-like carbon thin films deposited by filtered cathodic vacuum arc*, Journal of Applied Physics **95**, (2004), 3509.
- [47] K. O. Kese, Z. C. Li and B. Bergman, *Influence of residual stress on elastic modulus and hardness of soda-lime glass measured by nanoindentation*, Journal of Materials Research **19(10)**, (2004), 3109-3119.
- [48] A. Lee, B. M. Clemens and W. D. Nix, *Stress induced delamination methods for the study of adhesion of Pt thin films to Si*, Acta Materialia **52(7)**, (2004), 2081-2093.
- [49] C. M. Lepienski, G. M. Pharr, Y. J. Park, T. R. Watkins, A. Misra, et.al, *Factors limiting the measurement of residual stresses in thin films by nanoindentation*, Thin Solid Films **447**, (2004), 251-257.

- [50] B. C. Prorok, Y. Zhu, H. D. Espinosa, Z. Guo, Z. Bazant, et.al, *Micro-and nanomechanics*, Encyclopedia of Nanoscience and Nanotechnology **5**, (2004), 555-600.
- [51] S. Qu, Y. Huang, W. D. Nix, H. Jiang, F. Zhang, et.al, *Indenter tip radius effect on the Nix-Gao relation in micro-and nanoindentation hardness experiments*, J. Mater. Res **19(11)**, (2004), 3424.
- [52] F. Cleymand, O. Ferry, R. Kouitat, A. Billard and J. von Stebut, *Influence of indentation depth on the determination of the apparent Young's modulus of bi-layer material: Experiments and numerical simulation*, Surface & Coatings Technology **200(1-4)**, (2005), 890-893.
- [53] S. M. Han, R. Shah, R. Banerjee, G. B. Viswanathan, B. M. Clemens, et.al, *Combinatorial studies of mechanical properties of Ti 401 thin films using nanoindentation*, Acta Materialia **53(7)**, (2005), 2059-2067.
- [54] A. Mani, P. Aubert, F. Mercier, H. Khodja, C. Berthier, et.al, *Effects of residual stress on the mechanical and structural properties of TiC thin films grown by RF sputtering*, Surface & Coatings Technology **194(2-3)**, (2005), 190-195.
- [55] S. M. Han, R. Saha and W. D. Nix, *Determining hardness of thin films in elastically mismatched film-on-substrate systems using nanoindentation*, Acta Materialia **54(6)**, (2006), 1571-1581.
- [56] N. Schwarzer, *Analysing nanoindentation unloading curves using Pharr's concept of the effective indenter shape*, Thin Solid Films **494(1-2)**, (2006), 168-172.

- [57] B. Zhou, B. C. Prorok, A. Erdemir and O. Eryilmaz, *Annealing effects on the mechanical properties of near-frictionless carbon thin films*, *Diamond & Related Materials* **15(11-12)**, (2006), 2051-2054.
- [58] R. Haj-Ali and H. K. Kim, *Nonlinear constitutive models for FRP composites using artificial neural networks*, *Mechanics of Materials* **39(12)**, (2007), 1035-1042.
- [59] S. Liu and J. Wang, *Determination of Young's modulus and Poisson's ratio for coatings*, *Surface & Coatings Technology* **201**, (2007), 6470.
- [60] W. D. Nix, J. R. Greer, G. Feng and E. T. Lilleodden, *Deformation at the nanometer and micrometer length scales: Effects of strain gradients and dislocation starvation*, *Thin Solid Films* **515(6)**, (2007), 3152-3157.
- [61] F. Zhang, R. Saha, Y. Huang, W. D. Nix, K. C. Hwang, et.al, *Indentation of a hard film on a soft substrate: Strain gradient hardening effects*, *International Journal of Plasticity* **23(1)**, (2007), 25-43.
- [62] B. Zhou, B. C. Prorok, A. Erdemir and O. Eryilmaz, *Comparing the Young's Modulus of Near-Frictionless Carbon Films Obtained From Different Methods*, *Diamond Electronics--Fundamentals to Applications(MRS Symposium Proceedings Volume 956)* **956**, (2007), 255-260.
- [63] K. S. Chen, T. C. Chen and K. S. Ou, *Development of semi-empirical formulation for extracting materials properties from nanoindentation measurements: Residual stresses, substrate effect, and creep*, *Thin Solid Films* **516(8)**, (2008), 1931-1940.

- [64] Z. H. Xu and X. Li, *Effects of indenter geometry and material properties on the correction factor of Sneddon's relationship for nanoindentation of elastic and elastic-plastic materials*, *Acta Materialia* **56(6)**, (2008), 1399-1405.
- [65] X. Jiang, J. W. Zou, K. Reichelt and P. Grunberg, *J. Appl. Phys.* **66**, (1989), 4729.
- [66] D. Christopher, R. Smith and A. Richter, *Nanoindentation of carbon materials*, *Nuclear Inst. and Methods in Physics Research, B* **180(1-4)**, (2001), 117-124.
- [67] A. Bolshakov and G. M. Pharr, *Influences of pileup on the measurement of mechanical properties by load and depth sensing indentation techniques*, *J. Mater. Res* **13(4)**, (1998), 1049-1058.
- [68] K. W. McElhaney, J. J. Vlassak and W. D. Nix, *DETERMINATION OF INDENTER TIP GEOMETRY AND INDENTATION CONTACT AREA FOR DEPTH-SENSING INDENTATION EXPERIMENTS*, *Journal of Materials Research* **13(5)**, (1998), 1300-1306.
- [69] W. D. Nix and H. Gao, *Indentation size effects in crystalline materials: A law for strain gradient plasticity*, *Journal of the Mechanics and Physics of Solids* **46(3)**, (1998), 411-425.
- [70] X. Chen and J. J. Vlassak, *Numerical study on the measurement of thin film mechanical properties by means of nanoindentation*, *Journal of Materials Research* **16(10)**, (2001), 2974-2982.
- [71] W. D. Nix, *Mechanical properties of thin films*, *Metallurgical and Materials Transactions A* **20(11)**, (1989), 2217-2245.
- [72] J. A. Knapp, D. M. Follstaedt, S. M. Myers, J. C. Barbour and T. A. Friedmann,

- Finite-element modeling of nanoindentation*, Journal of Applied Physics **85**, (1999), 1460.
- [73] B. Zhou and B. C. Prorok, Thesis, Auburn University, 2005.
- [74] H. D. Espinosa, B. C. Prorok and M. Fischer, *A methodology for determining mechanical properties of freestanding thin films and MEMS materials*, Journal of the Mechanics and Physics of Solids **51(1)**, (2003), 47-67.
- [75] H. D. Espinosa, B. C. Prorok, B. Peng, K. H. Kim, N. Moldovan, et.al, *Mechanical properties of ultrananocrystalline diamond thin films relevant to MEMS/NEMS devices*, Experimental Mechanics **43(3)**, (2003), 256-268.
- [76] H. D. Espinosa, B. C. Prorok and B. Peng, *Plasticity size effects in free-standing submicron polycrystalline FCC films subjected to pure tension*, Journal of the Mechanics and Physics of Solids **52(3)**, (2004), 667-689.
- [77] H. Pelletier, J. Krier, A. Cornet and P. Mille, *Limits of using bilinear stress strain curve for finite element modeling of nanoindentation response on bulk materials*, Thin Solid Films **379(1-2)**, (2000), 147-155.
- [78] H. D. Espinosa, B. C. Prorok and M. Fischer, *A Novel Experimental Technique for Testing Thin Films and MEMS Materials*, Proc. of the SEM Annual Conf, (2001), 446-449.
- [79] B. Zhou, L. Wang, N. Mehta, S. Morshed, A. Erdemir, et.al, *The mechanical properties of freestanding near-frictionless carbon films relevant to MEMS*, JOURNAL OF MICROMECHANICS AND MICROENGINEERING **16(7)**, (2006), 1374.

- [80] B. Zhou, B. C. Prorok, A. Erdemir and O. Eryilmaz, *Microfabrication issues in constructing freestanding membranes of near-frictionless carbon and diamond-like films*, *Diamond & Related Materials* **16(2)**, (2007), 342-349.
- [81] H. Xu and G. M. Pharr, *An improved relation for the effective elastic compliance of a film/substrate system during indentation by a flat cylindrical punch*, *Scripta Materialia* **55(4)**, (2006), 315-318.
- [82] A. Bolshakov, W. C. Oliver and G. M. Pharr, *Influences of stress on the measurement of mechanical properties using nanoindentation: Part II. Finite element simulations*, *Journal of Materials Research* **11(3)**, (1996), 760-768.
- [83] C. M. Tan, *Study of Nanoindentation Using FEM Atomic Model*, *Journal of Tribology* **126**, (2004), 767.
- [84] J. D. Bressan, A. Tramontin and C. Rosa, *Modeling of nanoindentation of bulk and thin film by finite element method*, *Wear* **258(1-4)**, (2005), 115-122.
- [85] Y. Gaillard, C. Tromas and J. Woïrgard, *Quantitative analysis of dislocation pile-ups nucleated during nanoindentation in MgO*, *Acta Materialia* **54(5)**, (2006), 1409-1417.
- [86] K. B. Carlisle, M. Lewis, K. K. Chawla, M. Koopman and G. M. Gladysz, *Finite element modeling of the uniaxial compression behavior of carbon microballoons*, *Acta Materialia* **55(7)**, (2007), 2301-2318.
- [87] C. Walter, T. Antretter, R. Daniel and C. Mitterer, *Finite element simulation of the effect of surface roughness on nanoindentation of thin films with spherical indenters*, *Surface & Coatings Technology* **202(4-7)**, (2007), 1103-1107.

- [88] Y. Zhong and T. Zhu, *Simulating nanoindentation and predicting dislocation nucleation using interatomic potential finite element method*, Computer Methods in Applied Mechanics and Engineering, (2007)
- [89] A. A. Pelegri and X. Huang, *Nanoindentation on soft film/hard substrate and hard film/soft substrate material systems with finite element analysis*, Composites Science and Technology **68(1)**, (2008), 147-155.
- [90] C. W. Shih, M. Yang and J. C. M. Li, *Effect of Tip Radius on Nanoindentation*, Journal of Materials Research(USA) **6(12)**, (1991), 2623-2628.
- [91] B. Taljat and G. M. Pharr, *Development of pile-up during spherical indentation of elastic-plastic solids*, International Journal of Solids and Structures **41(14)**, (2004), 3891-3904.
- [92] G. Das, S. Ghosh and R. N. Ghosh, *Materials characterization and classification on the basis of materials pile-up surrounding the indentation*, Materials Science & Engineering A **408(1-2)**, (2005), 158-164.
- [93] W. M. Huang, J. F. Su, M. H. Hong and B. Yang, *Pile-up and sink-in in micro-indentation of a NiTi shape-memory alloy*, Scripta Materialia **53(9)**, (2005), 1055-1057.
- [94] D. L. Joslin and W. C. Oliver, *A New Method for Analyzing Data From Continuous Depth-Sensing Microindentation Tests*, Journal of Materials Research **5(1)**, (1990), 123-126.
- [95] Y. Huang, F. Zhang, K. C. Hwang, W. D. Nix, G. M. Pharr, et.al, *A model of size effects in nano-indentation*, Journal of the Mechanics and Physics of Solids

- 54(8)**, (2006), 1668-1686.
- [96] E. T. Lilleodden and W. D. Nix, *Microstructural length-scale effects in the nanoindentation behavior of thin gold films*, *Acta Materialia* **54(6)**, (2006), 1583-1593.
- [97] J. C. Angus and C. C. Hayman, *Low-Pressure, Metastable Growth of Diamond and "Diamondlike" Phases*, *Science* **241(4868)**, (1988), 913.
- [98] M. A. Lieberman and A. J. Lichtenberg, *PRINCIPLES OF PLASMA DISCHARGES* (Wiley, New York, 1994).
- [99] B. D. Cullity, *Elements of X-ray Diffraction (ed.)*, M. Cohen (Addison-Wesley, Reading, Massachusetts, 1978), 107.
- [100] M. F. Alzoubi, O. O. Ajayi, O. L. Eryilmaz, O. Ozturk, A. Erdemir, et.al, *Tribological behavior of near-frictionless carbon coatings in high-and low-sulfur diesel fuels*, 2000 SAE International Future Car Congress, Arlington, VA (US), 04/12/2000--04/16/2000, (2000)
- [101] A. Erdemir, O. Ozturk, M. Alzoubi, J. Woodford, L. Ajayi, et.al, *Near-frictionless carbon coatings for use in fuel injectors and pump systems operating with low-sulfur diesel fuels*, SAE International Congress & Exposition, Detroit, MI (US), 03/06/2000--03/09/2000, (2000)
- [102] A. Kovalchenko, O. O. Ajayi, A. Erdemir and G. R. Fenske, *Friction and wear performance of low-friction carbon coatings under oil lubrication*, 2002 Future Car Congress, Arlington, VA (US), 06/03/2002--06/05/2002, (2001)
- [103] J. Andersson, R. A. Erck and A. Erdemir, *Friction of diamond-like carbon films*

- in different atmospheres*, Wear **254(11)**, (2003), 1070-1075.
- [104] J. Hershberger, J. B. Woodford, A. Erdemir and G. R. Fenske, *Friction and wear behavior of near-frictionless carbon coatings in formulated gasolines*, Surface & Coatings Technology **183(1)**, (2004), 111-117.
- [105] J. A. Johnson, J. B. Woodford, X. Chen, J. Andersson, A. Erdemir, et.al, *Insights into near-frictionless carbon films?*, Journal of Applied Physics **95**, (2004), 7765.
- [106] C. Donnet and A. Erdemir, *Diamond-like Carbon Films: A Historical Overview*, Tribology of Diamond-like Carbon Films: Fundamentals And Applications, (2007)
- [107] J. Robertson, *Properties of diamond-like carbon*, Surface & Coatings Technology **50(3)**, (1992), 185-203.
- [108] R. C. Jaeger, *Introduction to microelectronic fabrication* (1987).
- [109] J. A. He, R. Valluzzi, K. Yang, T. Dolukhanyan, C. Sung, et.al, *Electrostatic Multilayer Deposition of a Gold-Dendrimer Nanocomposite*, CHEMISTRY OF MATERIALS **11**, (1999), 3268-3274.
- [110] J. J. Wortman and R. A. Evans, *Young's Modulus, Shear Modulus, and Poisson's Ratio in Silicon and Germanium*, Journal of Applied Physics **36(1)**, (1965), 153-156.
- [111] T. H. Wang, T. H. Fang and Y. C. Lin, *A numerical study of factors affecting the characterization of nanoindentation on silicon*, Materials Science & Engineering A **447(1-2)**, (2007), 244-253.

- [112] E. J. R. K. Chul Soo Lee, *Poisson's ratio of engineering plastics*, Advances in Polymer Technology **6(1)**, (1986), 85-90.
- [113] R. Pastorelli, A. C. Ferrari, M. G. Beghi, C. E. Bottani and J. Robertson, *Elastic constants of ultrathin diamond-like carbon films*, Diamond and Related Materials **9(3-6)**, (2000), 825-830.
- [114] K. G. H. Y. L. Q. Y. W. A. 爛. V. X. Pang, *Interfacial Microstructure of Chromium Oxide Coatings*, Advanced Engineering Materials **9(7)**, (2007), 594-599.
- [115] S. Mizuno, A. Verma, H. Tran, P. Lee and B. Nguyen, *Dielectric constant and stability of fluorine doped PECVD silicon oxide thin films*, Thin Solid Films **283(1-2)**, (1996), 30-36.
- [116] J. F. Shackelford and W. Alexander, *CRC Materials Science and Engineering Handbook* (CRC Press, 2001).
- [117] P. Hess, *Laser diagnostics of mechanical and elastic properties of silicon and carbon films*, Applied Surface Science **106**, (1996), 429-437.
- [118] P. Boch, J. C. Glandus, J. Jarrige, J. P. Lecompte and J. Mexmain, *Sintering, oxidation and mechanical properties of hot pressed aluminum nitride*, Ceramics International **8**, (1982), 34.
- [119] <http://www.szxulong.com/SinteredNdFeB-new-en.htm>,
- [120] C. Liang, L. Mathison and B. C. Prorok, *Mechanical Property Measurement of Interconnect Materials by Magnetostrictive Sensors*,
- [121] M. A. El Khakani, M. Chaker, A. Jean, S. Boily, J. C. Kieffer, et.al,

HARDNESS AND YOUNG'S MODULUS OF AMORPHOUS A-SIC THIN FILMS DETERMINED BY NANOINDENTATION AND BULGE TESTS,
Journal of Materials Research **9(1)**, (1994), 96-103.

- [122] A. C. Ferrari, *Diamond-like carbon for magnetic storage disks*, Surface & Coatings Technology **180**, (2004), 190-206.